EVALUATION OF TROPICAL CYCLONE FORECASTS FROM A GLOBAL MODEL AND COMPARISON WITH REGIONAL MESOSCALE NUMERICAL SIMULATIONS OF HURRICANE JOAQUIN

by

Yafan Yu

A thesis submitted to the faculty of
The University of Utah
in partial fulfillment of the requirements for the degree of

Master of Science

Department of Atmospheric Sciences

The University of Utah

December 2016

The University of Utah Graduate School

STATEMENT OF THESIS APPROVAL

The thesis of **Yafan Yu**

has been approved by the following supervisory committee members:

Zhaoxia Pu	, Chair	**06/27/2016** Date Approved
Edward J. Zipser	, Member	**06/27/2016** Date Approved
Steven K. Krueger	, Member	**06/27/2016** Date Approved

and by **Kevin Perry** , Chair/Dean of

the Department/College/School of **Atmospheric Sciences**

and by David B. Kieda, Dean of The Graduate School.

ABSTRACT

Accurate prediction of hurricane track and intensity is a challenging problem in numerical weather prediction (NWP). Evaluation of the performance of a forecast model is an important step in guiding model improvements. In this study, a statistical evaluation of track and intensity forecasts has been performed for the Navy Global Environmental Model (NAVGEM) during June 2014 to November 2014 for the Atlantic, East Pacific, and West Pacific basins. Results show that: 1) the averaged track errors of NAVGEM range from 100 km at day 1 to 460 km at day 5 and 2) the NAVGEM model has good skill in forecasting intensity trends, although the predicted intensifications lag the observed intensifications in many cases.

Then, a notable recent hurricane, Hurricane Joaquin (2015) is used to evaluate the ability of NAVGEM analysis and forecasts to represent the atmospheric conditions in both the large-scale environment and the vortex core region of the hurricane. In order to do this, a series of high-resolution mesoscale numerical simulations of Hurricane Joaquin is performed with an advanced research version of the Weather Research and Forecasting (WRF or WRF ARW) model, and the outcomes are compared with NAVGEM large-scale forecasts. Specifically, since there was considerable uncertainty in the Hurricane Joaquin NWP track forecast, five groups of sensitivity experiments with different cumulus, boundary layer, and microphysical schemes as well as different initial and boundary conditions and initial times in WRF simulations have been performed to

investigate the large-scale environment and hurricane inner-core structures related to the best-track simulation of Joaquin. It is found that the midlevel steering flows and the thermal structure of the hurricane core region are crucial for track and intensity forecasts. A comparison between the NAVGEM forecasts and the WRF simulation during 1200 UTC 30 September 2015 to 0000 UTC 4 October 2015 shows that NAVGEM makes a fairly good track forecast with reasonable representation of hurricane environmental conditions at its resolution.

CONTENTS

ACKNOWLEDGEMENTS

I would like to thank my advisor, Dr. Zhaoxia Pu, for her guidance, support, and help during this study. I also would like to thank my committee members, Dr. Ed Zipser and Dr. Steve Krueger, for their valuable comments.

I am grateful to all people in the Department of Atmospheric Sciences, especially the fellows in my research group. Special thanks to Chris Yu and Shixuan Zhang for their great help. I would also like to thank my family and friends, who have been very supportive during my study.

I am grateful to the National Center for Atmospheric Research (NCAR) Weather Research and Forecasting (WRF) model development group for their efforts that made the community model available. The computing support from the Center for High Performance Computing (CHPC) at the University of Utah is also greatly acknowledged. More importantly, I would like to thank Dr. Carolyn A. Reynolds at Naval Research Laboratory for providing NAVGEM data and her valuable comments.

CHAPTER 1

INTRODUCTION

Tropical cyclones (TC) out at sea cause large waves, heavy rain, flooding and high winds, disrupting international shipping and, at times, causing shipwrecks. Land-falling TCs can lead to even more severe economic losses and casualties. To save lives, mitigate property loss, and improve economic efficiency, the best possible forecasts of TC tracks and intensity are important. TC forecasts from numerical weather prediction (NWP) models are important presently as guidance to forecasters at both the National Hurricane Center (NHC) in Miami and the Joint Typhoon Warning Center (JTWC) at Pearl Harbor. However, accurate prediction of hurricane track and intensity is a challenging problem in numerical weather prediction. Evaluation of the performance of a forecast model is an important step in guiding model improvements.

1.1 Track forecast

Two challenging problems exist in NWP TC track forecasting: good physical representation and the dearth of observation data. Briefly, mathematical equations can approximately describe the various motions and interactions that occur in the atmosphere. Dynamical models solve the physical equations governing these atmospheric motions. One of the biggest challenges for hurricane modeling is creating a model that can accurately depict the large-scale, environmental flow of the atmosphere that is largely

responsible for steering the hurricane (e.g., Marchok 2014). Another problem is that computer forecast models are based on the available data. Many conventional data come from land-based weather observations, weather balloons and satellites, among other sources, but these surface weather observations and weather balloon data are lacking over the oceans where tropical storms and hurricanes are located for most of their life cycle. This can lead to incomplete datasets to input into computer models.

NWP models can be divided into two types: global models and regional models. Global models are dynamical models with a domain that encompasses the entire planet and the horizontal resolution of 30 km or less for one-week forecasts. Regional TC dynamical models are nonhydrostatic models with domains that encompass the area of a TC and horizontal resolution of a few (less than 10 km) kilometers while obtaining their boundary conditions from a global dynamical model. Due to higher-quality observations and better physical representation in global and regional models, it is well-known in the TC research and operational forecast communities that track forecasts have experienced large improvements during the past several decades. NHC forecast verification of early models for the period 1994–2015 shows a downward trend in model forecast error and the best-performing model changes almost every year. The 48-h track errors for different global and regional models in 2015 ranged between 50 and 150 nautical miles (around 100 to 300 km). In addition, some analysis indicated that the prediction accuracy and stability of the models were better for strong rather than weak TCs with short lead times (Chen et al., 2013).

1.2 Intensity forecast

The standard measure of TC intensity is the maximum sustained surface wind, which refers to the highest one-minute average wind at an elevation of 10 m. Intensity forecast improvements have lagged behind track improvements due to a much wider range of processes that must be accurately modeled to accurately predict intensity. The storm's inner-core structure, microphysical processes, air-sea energy exchanges, ocean response, interaction with land and the larger-scale environment, and radiative effects can all impact intensity changes (e.g., Wang and Wu, 2003). To accurately represent all these processes in numerical models will require an advanced coupled-ocean atmospheric prediction system with proper vertical and horizontal resolution and a data assimilation system that can utilize all available information, including in situ and remotely sensed observations in the inner core.

Quite a few operational global models have been reported to have a good ability to forecast TC intensity. A series of research projects have demonstrated that the TC intensity and structure simulated or predicted by NWP models can be significantly affected by the model settings, including the horizontal and vertical resolution, time-step size, vortex initialization scheme, and physics representations (e.g., Fierro et al., 2009). In practice, forecasters pay attention mainly to trends rather than absolute values of TC intensity from NWP models (Burton et al., 2010).

Despite the remarkable research progress that has been made in recent years on the fine-scale inner-core structure of TCs and the interaction between TCs and oceans (e.g., Chan and Kepert 2010), improvement in the forecast skill of TC intensity is still much less than what is found for TC track (Burton et al., 2010; Duan et al., 2012). As indicated by annul average NHC official intensity errors for the period 1990–2015 in the Eastern

North Pacific basin, there is barely any improvement for the 24-h forecast (remaining around 10 kt), while the improvement is more significant for long term forecast. For the best available intensity guidance at 24–72 h, studies show that improvements are statistically significant at the 95% level at most forecast times (DeMaria et al., 2014). Despite the comparatively small improvement, research still shows that NWP models have had some skill in predicting TC intensity. Intensity forecasts from six operational models (three global models and three regional models) during 2010 and 2011 in the Western Pacific basin showed that two of them were better than a statistical baseline in Vmax at several lead times and three of that showed some skill in intensity change (Yu et al., 2013). In addition, increases in model resolution improves the intensity forecasts, likely arising from a combination of improved representation of the largescale flow, more realistic interactions between TCs and their environment, and more accurate representations of small-scale features (Zarzycki and Jablonowski 2015).

1.3 Scope of the study

This study aims to evaluate the performance of the Navy Global Environmental Model (NAVGEM), a new model that replaced the Navy Operational Global Atmospheric Prediction System (NOGAPS) and completed its first operational test in January 2013 (Pauley et al., 2013).

The evaluation focuses on TC track and intensity forecasts/analysis through statistics based on one hurricane season in different ocean basins and also on a comparison with high-resolution mesoscale numerical simulations using a mesoscale community Weather Research and Forecasting (WRF) model. Specifically, one season of data, from 1 June to 30 November 2014 is used to evaluate the NAVGEM forecast. Details of the verifications

are shown in Chapter 2. Then a specific case, Hurricane Joaquin (2015) is chosen to evaluate how well the NAVGEM model can represent the large-scale environment, which is crucial for track forecasts, as stated previously. In order to achieve this goal, first, in Chapter 3, we employ an advanced research version of the WRF model to conduct a sensitivity experiment to obtain a set of relatively good simulations. Then, the comparison between the global model and the WRF simulations is discussed in Chapter 4. A summary and concluding remarks are provided in Chapter 5.

CHAPTER 2

STATISTICAL EVALUATION OF NAVGEM TROPICAL CYCLONE FORECASTS FOR THE ATLANTIC, EAST PACIFIC AND WEST PACIFIC BASINS DURING JUNE TO NOVEMBER 2014

2.1 Introduction

2.1.1 Background

The Navy Global Environmental Model (NAVGEM), which replaced the Navy Operational Global Atmospheric Prediction System (NOGAPS) that was introduced in 1982, is a new atmospheric forecast model developed by the Naval Research Lab (NRL) - Monterey. It was transitioned to the Fleet Numerical Meteorology and Oceanography Center (FNMOC) and completed its first operational test in January 2013 (Pauley et al., 2013). The NAVGEM model represents a significant NRL milestone in numerical weather prediction system development by introducing a Semi-Lagrangian/Semi-Implicit (SL/SI) dynamical core together with advanced moisture and ozone physical parameterization schemes (Hogan et al., 2014). The new SL/SI dynamic core allows the model to have much higher resolutions without the need for small time steps, which permits NAVGEM to have both higher horizontal and vertical resolutions than NOGAPS (42 vertical levels, 42 km horizontal resolution).

Few studies have been done to verify the track and intensity forecast of the current

version (v1.3) of NAVGEM. In this chapter a statistical evaluation of the 1) track error; 2) intensity error; and 3) intensity trend forecast of NAVGEM are performed for the Atlantic, East Pacific and West Pacific basins during 1 June to 30 November 2014.

2.1.2 Brief description of NAVGEM

The NAVGEM v1.3 forecast is verified in this study. This model version runs at T425L60 (~31km) horizontal resolution with 60 vertical levels. Its output is sampled at 1° × 1° horizontal resolution. This atmospheric model uses a Semi-Lagrangian/Semi-Implicit dynamical core, which utilizes perturbation virtual potential temperature to improve numerical stability and reduce semiimplicit decentering. Several new parameterization schemes are introduced in NAVGEM, including a new 2-species micro-physics cloud water parameterization based on the work of Zhao et al. (1997) and Rapid Radiative Transfer Model for General Circulation Models (RRTMG) parameterizations for solar and long-wave radiation, developed by Atmospheric and Environmental Research Inc. (see details in Hogan et al., 2014). Upgrades in version 1.3 of NAVGEM include new stratospheric physics for water vapor photo-chemistry, subgrid-scale non-orographic gravity wave drag, and stratospheric humidity quality control. In addition, predicted convective cloud fraction based on Xu-Randall and improved initialization of ground wetness and temperature are also introduced (Reynolds 2014).

2.2 Data and methods

The statistical evaluation was performed from 1 June to 30 November 2014. During this time, 42 TCs (including TCs that only developed into tropical depressions) were reported by the NHC and JTWC with 8 TCs in the Atlantic basin, 19 in the East Pacific, and 15 in the West Pacific basin.

All TCs that can be represented in the NAVGEM forecasts (namely, when low pressure systems can be identified in the region near the best-track TC center) are tracked through minimum sea level pressure (MSLP) at all forecast initial times. Forecasts from 00–120 h with 3-h increments, initialized at 00Z of each date during this time period, are available in the NAVGEM forecast data. The maximum surface wind (MSW) is searched for a square area of $3° \times 3°$ centered at the storm center that is tracked by MSLP. The recorded track, MSLP and MSW are compared with best-track data. The best-track data for the Atlantic and East Pacific basins are provided by the National Hurricane Center, a division of the United States National Weather Service. The data for the West Pacific basin are provided by the Joint Typhoon Warning Center, which is under joint Navy and U. S. Air Force command. Best-track data are available at 6-h increments for the location of the storm center, 10-m wind and MSLP.

Forecast track and intensity errors are defined as the absolute value of the difference between the forecast and best track at the forecast verification time. The best track and forecast track are plotted for every tropical storm and every initial time to ensure the tracked storm centers are reasonable. The track plots of Hurricane Arthur are provided as an example in Figure 2.1. Correct identification of the initial track center is important for correctly locating the track center in the following lead times. Due to the $1° \times 1°$ output resolution of the NAVGEM model, an initial track error of around 80 km is acceptable. If the tracked storm center shows great deviation from its corresponding best track, the sea level pressure fields are then checked manually to identify the storm center. This process is especially important to landfalling or offshore TCs due to the topography effect. The MSLP and MSW of the best-track versus the model forecast are also plotted for each TC and each initial time.

For both track and intensity forecasts, the impact of different TC phases on error statistics is investigated. A brief overview of the stages of tropical cyclones follows. TCs start from tropical disturbances/waves, which are organized areas of rain and thunderstorms with no definable surface circulation. The second stage is the tropical depression phase. All TCs that have maximum sustained wind speeds of less than 33 kts (17 m s^{-1}) are classified as tropical depression. A tropical depression strengthens into a tropical storm once its maximum sustained surface winds are greater than 17 m s^{-1}. To be classified as a hurricane, a TC must have maximum sustained winds reaching 64 kts (33 m s^{-1}) and the minimum wind speed for major hurricane is 96 kts (49 m s^{-1}) (Sampson et al., 1995). In this study, the last four stages (tropical depression, tropical storm, hurricane, and major hurricane) are considered.

To clarify, a 120-h (or less) forecast is available at several initial times. For the lead time error statistic, the error is calculated by averaging over all TCs and all initial times at a certain lead time; for the phase-dependency error statistic, the error is calculated by averaging over all initial times for a certain TC at each lead time.

2.3 Results

2.3.1 Statistical summary

In this study, a total of 39 TCs are represented in the NAVGEM forecasts, with 8 in the Atlantic basin, 19 in the East Pacific, and 15 in the West Pacific basin. A summary of the corresponding best-track phases at the time when the TCs are first predicted in the model (when NAVGEM can represent a TC in its analysis/forecast) is shown in Table 2.1. In the Atlantic basin, the NAVGEM forecast can represent 37.5% of all TCs from an early stage (tropical depression) and fails to forecast 12.5% of the total reported TCs; in

the East Pacific basin, it can represent 55% of all TCs from the tropical depression phase and fails to forecast 10% of total TCs; in the West Pacific basin, NAVGEM forecasts can represent 87% of all TCs during the study period starting from the tropical depression stage of best track and no TC is missed. From June to November 2014, model performance in the West Pacific is better than in either the East Pacific or Atlantic basins because it can represent TCs from an early stage in most cases. In both the West and East Pacific basins, TCs can be identified before they reach hurricane phase, except those that were missed in the forecast.

2.3.2 Track errors

As described in section 2.2, the center of a TC is tracked through the MSLP. Figure 2.2 shows the dependency of track errors on the TC phase. Each point in these plots is the track error averaged over forecasts from all initial times for a certain TC at a certain time. The tropical depression phase is excluded from this statistical evaluation as convention, because the storm is too weak to be correctly tracked in a global model. Results indicate that track errors are phase-dependent, especially in the Atlantic and East Pacific basins. Larger errors occur mainly at the tropical storm phase, and the uncertainties in the track errors are also larger when the TCs are weak. Specifically, track errors in the tropical storm phase range from 0 to 1000 km in the Atlantic basin, from 50 to 600 km in the East Pacific and from 0 to 580 km in the West Pacific. In the hurricane phase, track errors range from 10 to 600 km in the Atlantic basin, from 100 to 400 km in the East Pacific and from 100 to 700 km in the West Pacific. For the major hurricane stage, track errors range around 250 km in the Atlantic basin, from 180 to 350 km in the East Pacific and from 100 to 550 km in the West Pacific. The NAVGEM model shows better track forecasts in

the Atlantic basin than in the two other basins for TCs in the major hurricane stage, judging from the extreme track errors. The model performance is similar in the East and West Pacific.

Figure 2.3 shows the lead time track error for the three basins. In each box in the plots, the central mark is the median, the edges of the box are the 25th and 75th percentiles, the whiskers represent the extreme data and the outliers are plotted individually. When outliers are not included, track errors marked by the extreme value in each box range from around 100 km for day 1 to 400 km for day 5 in the Atlantic basin. These errors go from 100 km to 450 km in the East Pacific and from around 100 km to beyond 500 km in the West Pacific during the 120 h forecast. The initial time track errors are similar among all basins. Forecasts initialized early, when TCs are relatively weak, usually show larger errors than those initialized at a more mature TC stage. An increasing trend of track errors with forecast time clearly exists.

2.3.3 Intensity error

The bias and mean absolute errors (MAEs) of MSLP and MSW are investigated in this study. The maximum wind of NAVGEM versus best-track data in Figure 2.4 shows the bias of the intensity forecast. The tropical depression phase is considered here; however, due to the relatively low accuracy of the identified storm center at this phase, the reliability of the intensity forecast is also relatively low. As expected from the relatively coarse resolution of the global model, NAVGEM tends to underestimate the best track intensity at the hurricane and major hurricane phases. For lower wind speeds, model forecasts and best-track data are at the same scale, especially in the tropical depression stage.

The intensity bias shown by MSLP (Figure 2.5) is similar to that shown by MSW (Figure 2.4). It is noted that in the plot for the Atlantic basin, some MSLP value of the tropical storm phase (blue dots) are even lower than those of the hurricane phase for both the best-track and model forecast data. This is because the TC phases were identified by the MSW of the best-track data. It should be noted that in the best-track data provided by the NHC, in some cases when a TC is categorized as tropical storm, it has a corresponding MSLP that as intense as 963 hPa (e.g., Hurricane Cristobal). The reason why the positively-correlated wind-pressure relationship in the Atlantic basin is not the same as in the East Pacific or West Pacific basins is unknown. However, TCs with relatively low MSW and intense MSLP occur at very high latitude (e.g., at around 60^{o}N for Hurricane Cristobal and Hurricane Arthur).

The MAEs of MSW and MSLP (Figure 2.6) are evaluated every 6h during the 120h forecasts. At each time the MAE is an average over all initial times for each storm. For MSW, forecast errors range from 0 to around 25 m/s. The largest intensity error occurs in the West Pacific basin, but the difference is not significant among the three basins. The mean MAE of MSW is around 8 m s^{-1}. For MSLP, forecast errors are largest in the West Pacific, especially beyond the 72 h forecast, ranging between 0 and around 55 hPa. Errors are lowest in the East Pacific, ranging from 0 to 30 hPa. The mean MAEs of MSLP for the Atlantic, East Pacific and West Pacific are 10, 12, 18 hPa, respectively. It can be seen that forecast time has little influence on intensity error.

2.3.4 Intensity trend forecast

2.3.4.1 Correlation between model forecast and best-track intensity

Due to the relatively coarse resolution of global models, they are not commonly expected to predict the actual intensity of TCs. Thus, the ability of NAVGEM to forecast TC intensity trend is of more concern, as stated in the introduction chapter. Therefore, in this section we evaluate NAVGEM forecasts in terms of intensity trend. In order to do this, we utilize the Pearson product-moment correlation.

In statistics, the Pearson product-moment correlation coefficient, p, is a measure of the linear correlation between two variables X and Y, giving a value between +1 and −1, where 1 is total positive correlation, 0 is no correlation, and −1 is total negative correlation. It is widely used in the sciences as a measure of the degree of linear dependence between two variables. Conventionally, when the absolute value of p ranges between 0.5 and 1, it indicates that the strength of relationship between the two variables is strong; when the value of p ranges between 0.3 and 0.5, the correlation is moderate and when it is below 0.3, the correlation is weak. Thus, the Pearson product-moment correlation coefficient of the model forecast and best-track intensity is calculated by equation (1),

$$\rho_{XY}(\tau) = \frac{E[(X_t-\mu_X)(Y_{t+\tau}-\mu_Y)]}{\sigma_X\sigma_Y} \quad (1)$$

where X is the best-track intensity, Y is the model forecast, τ is the lag time, μ is the average of the model forecast and best-track intensity, respectively, and σ is the standard deviation. The lag time τ is set at zero when the ability of the NAVGEM model to forecast intensity trend is investigated.

The distribution of correlation coefficients for MSW and MSLP is shown in Figure 2.7. MSW shows a better correlation between the model forecast and best track than MSLP. When the intensity of a TC is characterized by MSW, 32 out of 39 TCs have p values greater than 0.5. When the intensity is characterized by MSLP, 26 out of 39 TCs have p values greater than 0.5. A quantified summary of the distribution of p values in three intervals, 0–0.5, 0.5–1 and below 0, is shown in Table 2.2. For maximum surface wind, 82% and 97% of TC forecasts show strong or positive correlations between best-track and model intensity. For MSLP, the percentiles are 67% and 94% respectively. Overall, the NAVGEM global model can forecast more than 50 % of the intensity trends at most of the time.

2.3.4.2 Lag time

Further investigation into whether a lag exists in the NAVGEM intensity trend prediction is performed. The τ in equation (1) is selected to be different values in the -36 to 36-h interval with 6-h increments. Lag time is defined as the τ that corresponds to the maximum correlation coefficient for each storm. When the lag is positive, it means that the intensity change (usually characterized by intensification) in the model forecast is ahead of that in the best track and vice versa. Lags exist in the trend forecast and vary case by case. The distribution of lag time (MSW versus MSLP) is shown in Figure 2.8, which indicates that lag ranges from -36 to 24 h. It can be seen that the mark density is highest around -20 to 0 h lag for both MSW and MSLP. A quantified summary of the distribution of lag times in all three basins is listed in Table 2.3. For both MSW and MSLP, intensification usually starts later in the model forecast than in the best track. Specifically, 6 out 19 TCs in the East Pacific basin, 9 out 15 TCs in the West Pacific

basin and 5 out of 7 TCs in the Atlantic basin have negative lag time for both MSLP and MSW. The consistency of the trend forecast between MSW and MSLP is good. Namely, for most cases, when the MSW forecast is behind the best track, the MSLP forecast also tends to lag behind the best track.

2.4 Additional discussion

Considering the large uncertainty in identifying center positions of TCs when they are weak, the above statistical verification for track errors did not include tropical depression phase and outliers. However, there is a large sample of forecasts represents the TD phase or weak TCs. To make a more complete evaluation for the NAVGEM forecasts, additional comparisons are conducted for the statistics with and without the TD phase and outliers.

2.4.1 Impact of the tropical depression phase on track error statistic

Mean absolute track errors at 120h with the TD phase of each storm included, calculated by averaging all data at each lead time, are shown in Figure 2.9. As expected, including the TD phase significantly increases lead time track errors; the medians of long-term forecasts for all three basins go beyond 500 km. Compared with Figure 2.2, the impact of including the TD phase in the statistic is more significant for long-term forecasts (beyond 48 h), especially in the Atlantic basin. For a forecast lead time of 0–48 h, the change is not as significant. Specifically, the range of track errors indicated by the median change from 100–350 km (with the TD phase) to 100–280 km for the Atlantic basin; it changes from 200–380 km (with the TD phase) to 180–300 km for the West Pacific basin; and it remains around 180–280 km for the East Pacific basin. For the forecast at 120 h, the track error decreases from 550 km to 300 km in Atlantic basin, from

500 km to 220 km in the East Pacific basin and from 580 km to 280 km in the West Pacific basin. Excluding the TD phase makes the sample size of the Atlantic basin quite small. In addition, the uncertainty of track errors at each lead time is also decreased. For both including and excluding TD phase statistics, the mean track errors are similar in all three basins.

2.4.2 Impact of outliers on track error statistic

Outliers are determined subjectively. Track errors that are more than three times the mean track error from a certain initial time for a certain storm are treated as outliers. The 120 h lead time track errors without outliers (Figure 2.10) versus with outliers (Figure 2.11) are shown in bar plots. The tropical depression (TD) phase is excluded from this statistic to evaluate solely the impact of outliers on the track error statistic. Since the sample size is quite small, sometimes changing even one day's data has a perceptible influence on the basin-averaged data. The change is most noticeable in the Atlantic basin, where the sample size is the smallest. The anomalous high values around 96-h forecast are removed after outliers are excluded. In the Atlantic basin, the range of track errors changes from 70–300 km (with outliers) to 70–220 km (without outliers). In the East Pacific basin, the track error at 120-h forecast changes from beyond 250 km to less than 250 km. In the West Pacific basin, the maximum track error decreases from 330 km (with outliers) to 270 km (without outliers). When the TD phase is excluded, the existence of outliers has little influence on initial time track error. For all three basins, removing the outliers smooths the error growth as well as reduces the magnitude of track errors.

Finally, a lead time track error statistic is averaged over all three basins (Figure 2.12). The TD phase is excluded. Lead time track error ranges from 70 km to 550 km with

outliers, and is reduced to 70–460 km without outliers.

2.5 Summary

The performance of the newly launched NAVGEM global numerical model is evaluated regarding track and intensity forecast errors. For track errors, results are different when TDs/outliers are considered. Since the TD phase is conventionally excluded from the statistic, the mean track error averaged over all three basins ranges from around 70 km in day 1 to 460 km in day 5 (without outliers) and grows with lead time. Long-term forecasts are better in the Atlantic basin than in the other two basins, but no significant difference exists among the three basins.

For intensity errors, the NAVGEM forecasts underestimate best-track intensity, especially in the hurricane and major hurricane phases, as expected from the relatively coarse resolution of the global model. Lead time has little influence on intensity error. Special attention is paid to the trend forecast: at a 0.5 significance level, most TCs (82% of MSW and 67% of MSLP) show a significant positive correlation in intensity change between the model and best-track data. Therefore, NAVGEM may still have good skill in terms of forecasts of intensity trend. However, the forecasted intensification time is behind the observed time in most cases.

Table 2.1

A summary of the corresponding best-track phases at the time when the TCs are first represented in the NAVGEM model forecast

	Tropical depression (number/percentile)	Tropical storm (number/ percentile)	Hurricane (number/ percentile)	Missed (number/ percentile)
Atlantic	3 (37.5%)	2 (25%)	2 (25%)	1 (12.5)
East Pacific	11 (55%)	6 (35%)	0	2 (10%)
West Pacific	13 (87%)	2 (13%)	0	0

Table 2.2

Summary of the distribution of correlation coefficients of the model forecast and best-track intensity

	>0.5	0<r<0.5	<0
MSW	32/39	6/39	1/39
MSLP	26/39	11/39	2/39

Table 2.3

Lag time distribution of MSLP versus MSW in all three basins

for all TC cases.

East Pacific		**MSLP**			**West Pacific**		**MSLP**		
		lag	lead	0			lag	lead	0
MW	lag	6	3	1	**MW**	lag	9	0	0
	lead	1	2	1		lead	4	0	0
	0	1	2	0		0	2	0	0

Atlantic		**MSLP**	
		lag	lead
MW	lag	5	1
	lead	0	1

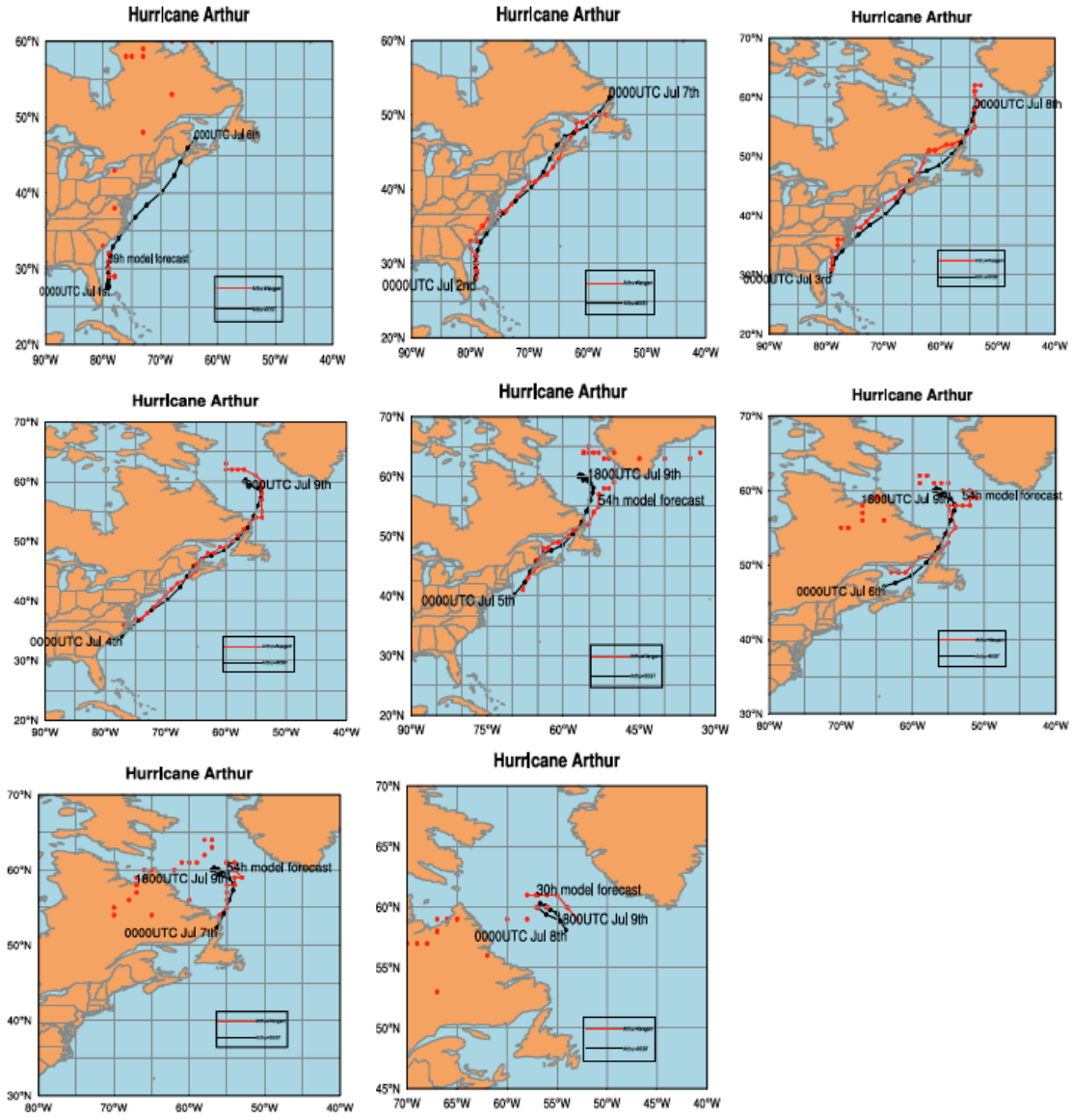

Figure 2.1 Best track (black line) versus model forecast (red line) for Hurricane Arthur. Initial and end times are labeled in each panel.

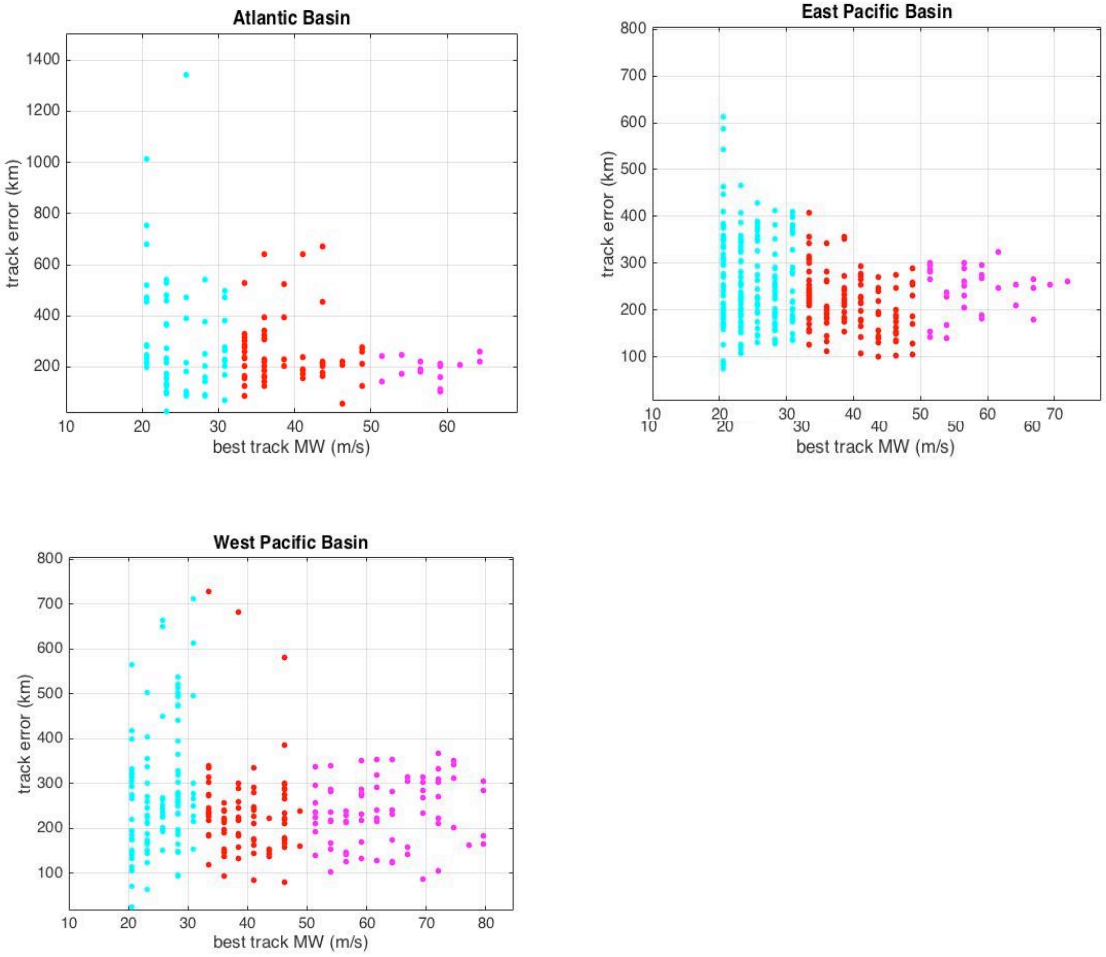

Figure 2.2. Averaged track errors of all forecasts at different initial times at tropical storm (cyan), hurricane (red) and major hurricane phases (magenta). Different TC phases is identified by maximum surface wind.

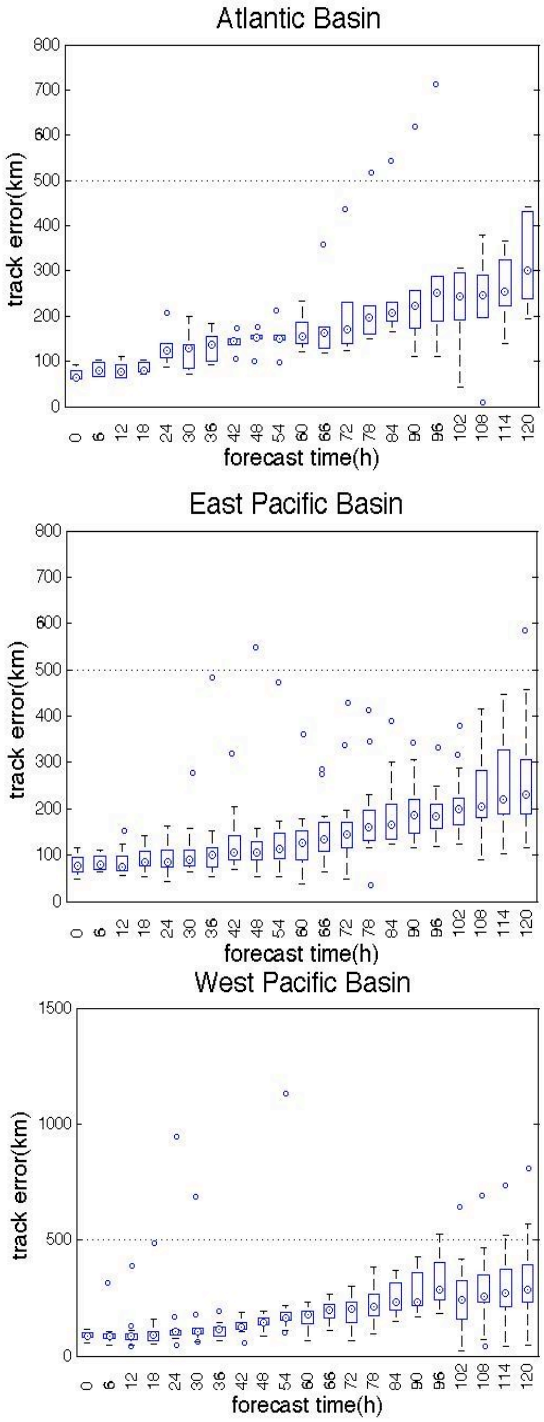

Figure 2.3. Ranges of track errors with tropical depression phase excluded for the Atlantic, East Pacific, and West Pacific basins. In each box, the central mark is the median, the edges of the box are the 25th and 75th percentiles, the whiskers extend to the extreme data and the outliers are plotted individually.

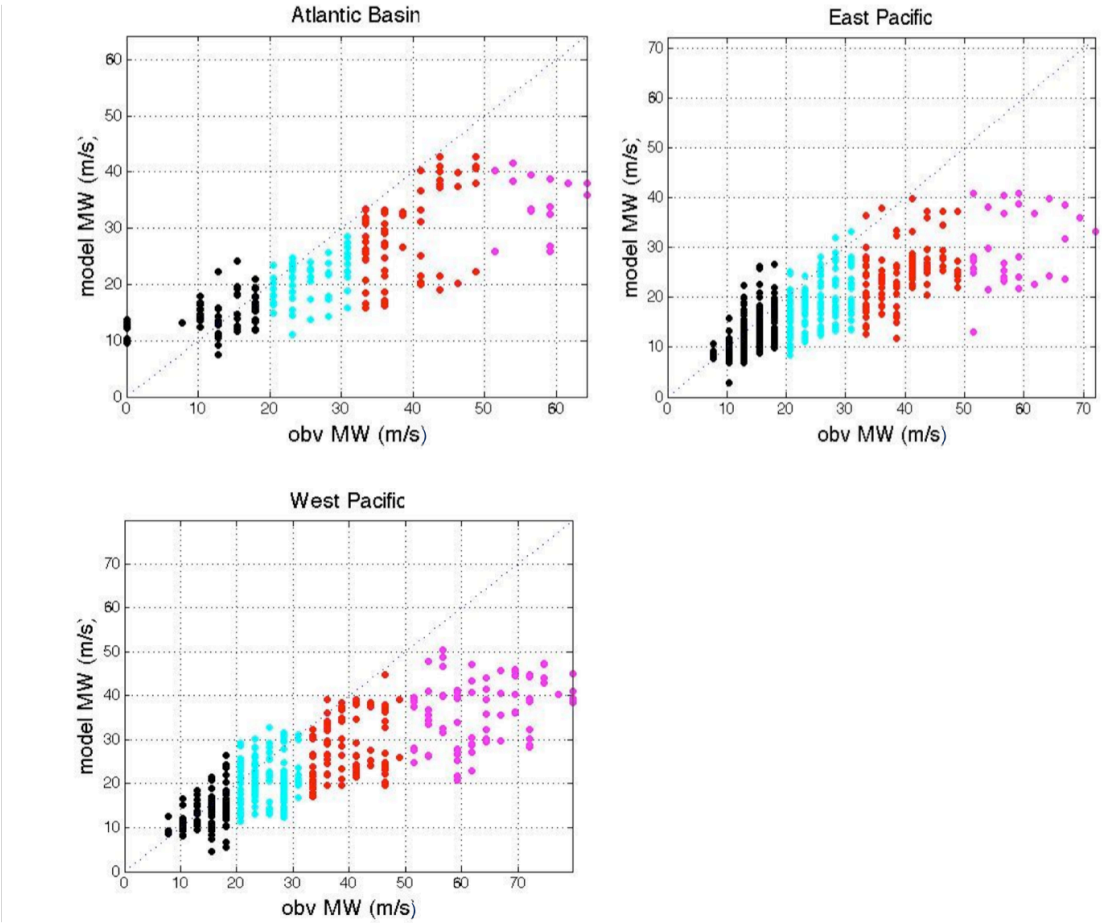

Figure 2.4. Maximum surface wind of NAVGEM versus best track data at tropical depression (black), tropical storm (cyan), hurricane (red) and major hurricane (magenta) phases for all three basins.

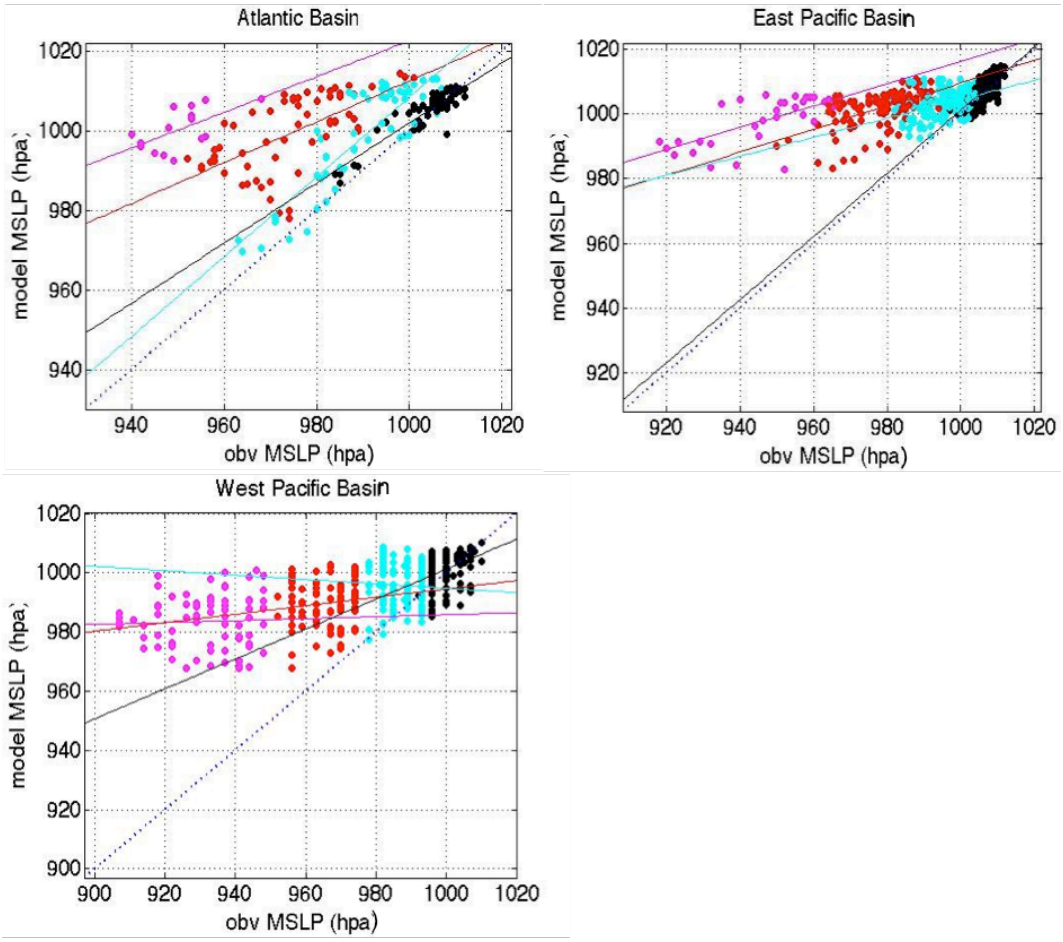

Figure 2.5. Minimum sea level pressure of NAVGEM versus best track data at tropical depression (black), tropical storm (cyan), hurricane (red), and major hurricane (magenta) phases for all three basins.

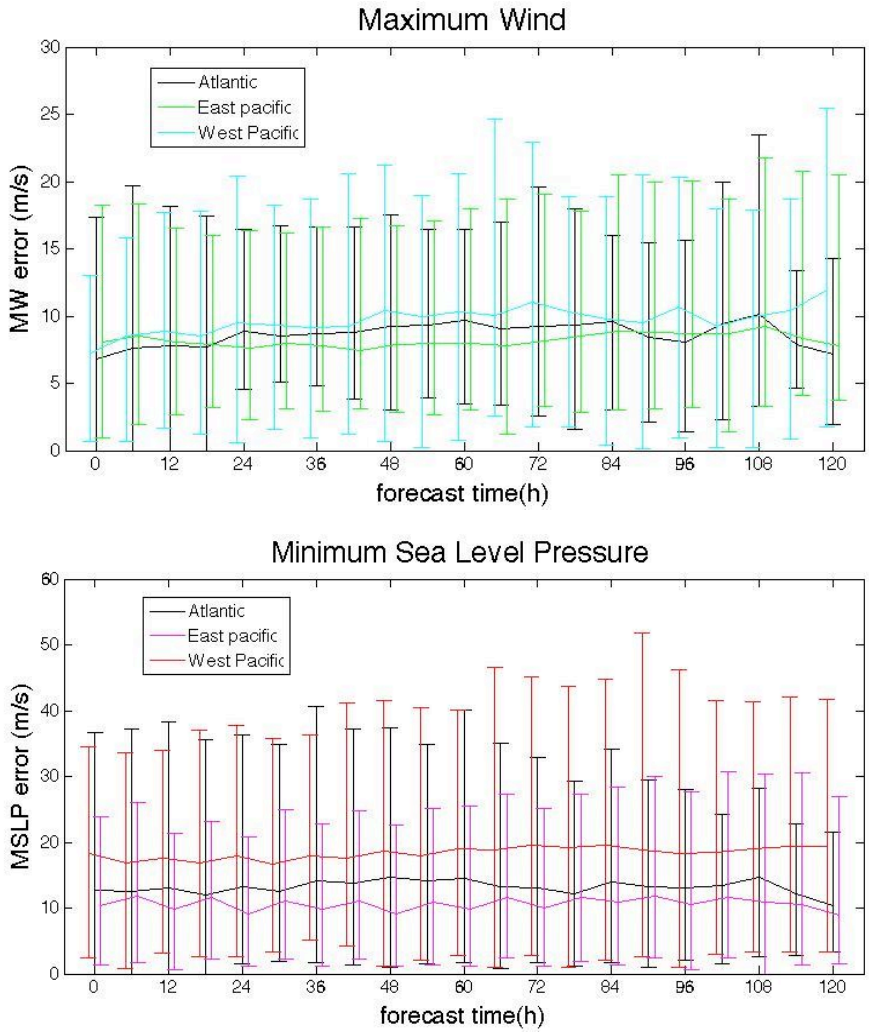

Figure 2.6. Mean absolute error of maximum surface wind (top panel) and minimum sea level pressure (bottom panel) for the Atlantic, East Pacific, and West Pacific basins. The bar plots show the mean and extreme values at every 6 h in 120-h forecast.

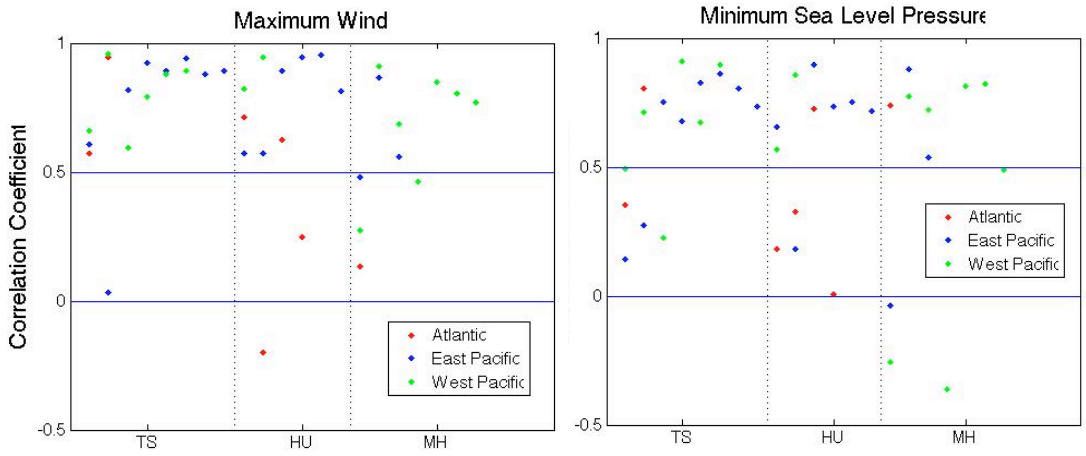

Figure 2.7. The distribution of correlation coefficients of model forecast and best track intensity. The p values for the Atlantic (red), East Pacific (blue), and West Pacific (green) basins are divided into tropical storm, hurricane and major hurricane phases.

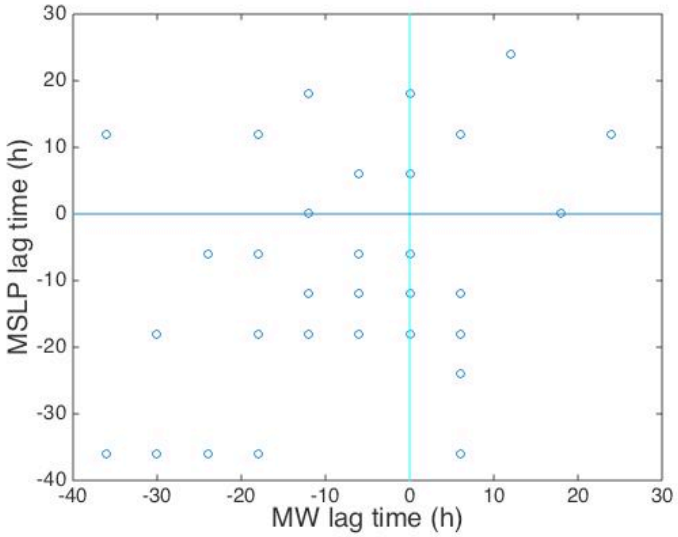

Figure 2.8 The distribution of lag time for minimum sea level pressure and maximum wind respectively for all TC cases in the Atlantic, East Pacific, and West Pacific basins.

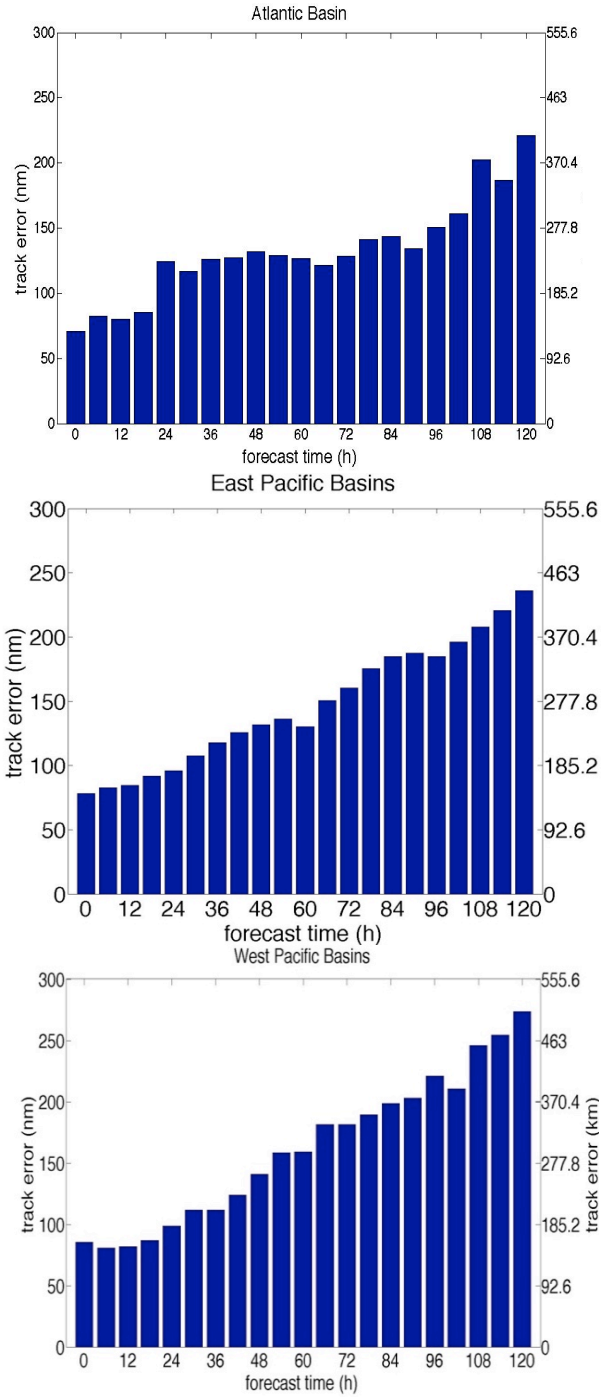

Figure 2.9. Ranges of track errors with the tropical depression phase included for the Atlantic, East Pacific, and West Pacific basins. In each box, the central mark is the median, the edges of the box are the 25th and 75th percentiles, the whiskers extend to the extreme data and the outliers are plotted individually.

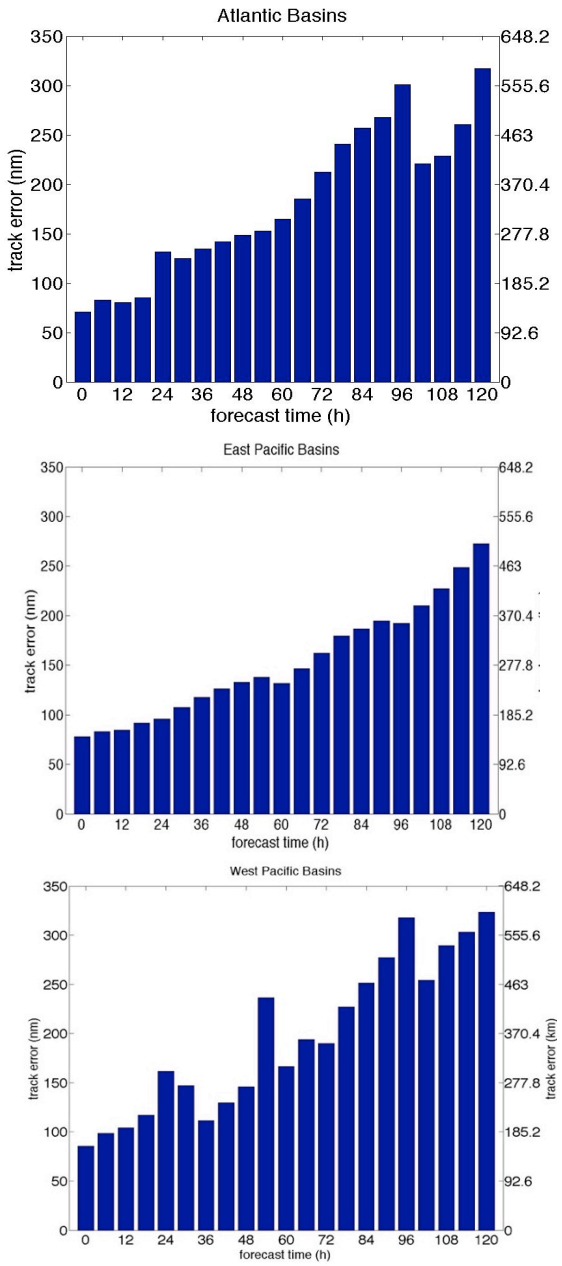

Figure 2.10 Averaged forecast track errors without outliers for TCs in relatively mature stage (MSW > 34 kt). The y-axis is labeled in nautical miles and kilometers, respectively.

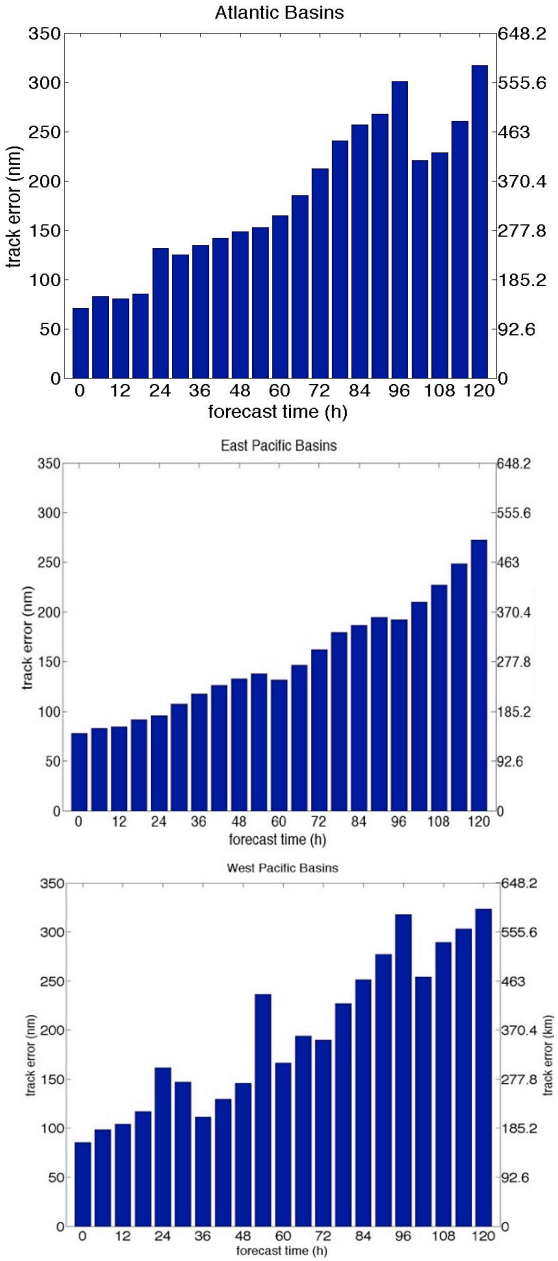

Figure 2.11 Same as Figure 10, except for that outliers are included in this statistic.

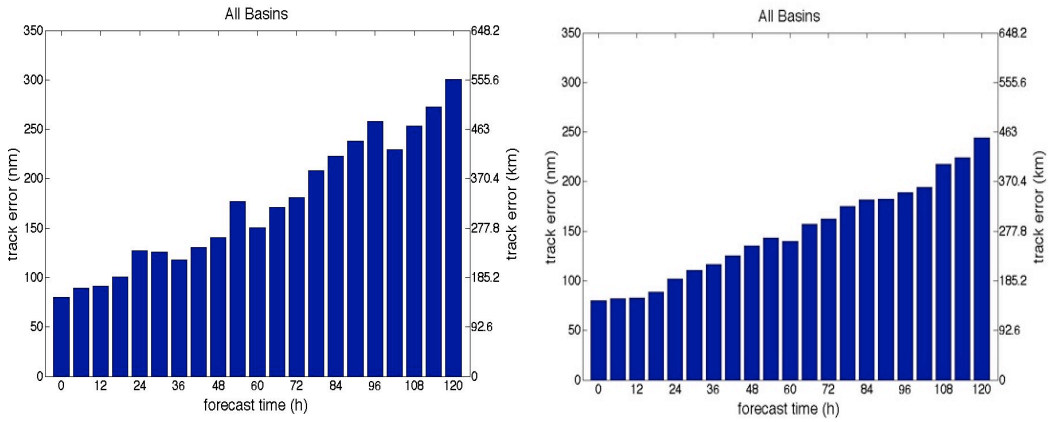

Figure 2.12 Time variation of track error averaged over all three basins for data with outliers (left panel) and without outliers (right panel). Tropical depression phase is excluded in both figures.

CHAPTER 3

NUMERICAL SIMULATIONS OF HURRICANE JOAQUIN (2015) WITH THE MESOSCALE WEATHER RESEARCH AND FORECASTING MODEL

As stated in the introduction, the accurate representation of the large-scale environmental fields and inner-core structures of TCs are crucial for high-quality track and intensity forecasts. Therefore, a case study is conducted to further investigate how well the NAVGEM model can represent the environment and hurricane inner-core fields. Considering the results from the previous section, we expect that the NAVGEM should have good ability to represent the TC environmental field because of its ability to predict TC track. Due to its coarser resolution, it should have less ability to represent the TC inner-core structure. In order to conduct further investigation, we should compare the NAVGEM analysis and forecast with a set of reference high-resolution numerical simulation and analysis. In this chapter, we attempt to achieve a set of reasonable mesoscale numerical simulation that can be used for this purpose. Hurricane Joaquin (2015), which experienced large uncertainty in its track forecast during real-time operational forecasts, is selected. Several sensitivity experiments are performed using the WRF-ARW model to obtain a set of relatively reasonable mesoscale numerical simulations of Hurricane Joaquin.

3.1 Overview of Hurricane Joaquin

Hurricane Joaquin (2015) was a category 4 hurricane (on the Saffir-Simpson Hurricane Wind Scale), which was designated as a tropical depression at 0000 UTC 28 September 2015 and dissipated after 0000 UTC 15 October 2015. At 0000 UTC 29 September 2015, it reached the tropical storm stage and a blocking ridge of high pressure was located over the western Atlantic, forcing Joaquin to move slowly southwestward. A 60-h period of rapid intensification began at 0600 UTC 29 September 2015, and Joaquin became a hurricane at 0600 UTC 30 September 2015 and then a major hurricane at 0000 UTC 1 October 2015. Meanwhile, a mid- to upper-level trough over the eastern United States deepened on 1 and 2 October 2015, causing Joaquin to slow down and make a clockwise hairpin turn over the southeastern and central Bahamas. Joaquin continued to strengthen, reaching a relative peak in intensity as a 120-kt category 4 hurricane between 0000 UTC 2 October 2015 and 0600 UTC 2 October 2015. Joaquin did not have a clear eye typical of category 4 hurricanes.

The prediction of Hurricane Joaquin's hairpin clockwise from 2100 UTC 1 October 2015 to 0600 UTC 2 October 2015 presents a forecasting challenge during real-time prediction, as tracks of several numerical models differ from each other. Therefore, the track forecast of Joaquin becomes an interesting research question.

In this chapter, we conduct high-resolution, mesoscale numerical simulations to investigate the ability of the mesoscale community WRF model to predict Hurricane Joaquin (2015). Through the sensitivity of numerical simulations to various physical processes and initial conditions, we hope to obtain a set of simulations with a relatively good representation of Hurricane Joaquin's track and its environment, which will not only provide a high-resolution dataset that will be useful for further evaluation of

NAVGEM global forecasting, but will also offer insights about the key parameters that we should compare between regional and global models in hurricane cases.

3.2 Description of numerical simulations

3.2.1 Model setup

An advanced research version of the Weather Research and Forecasting (WRF ARW) Model (version 3.7) is used to conduct numerical simulations of Hurricane Joaquin. A detailed description of ARW v3.7 can be found in Skamarock et al. (2007).

A two-way interactive, three-level nested grid technique is employed to conduct the multiscale simulations with the ARW model. Figure 3.1 shows the location of model domains for two different initial times and Table 3.1 lists the specifications for the model domains. All three domains are fixed with 27-km, 9-km, and 3-km grid-spacing respectively. The model vertical structure comprises 37 levels with the top of the model set at a pressure of 50 hPa.

3.2.2 Initial/boundary conditions and initial times

Two sets of global analyses are selected in this study for initial and boundary conditions: the National Centers for Environmental Prediction's (NCEP) Global Forecast System analysis data (GFS-ANL) at $0.5° \times 0.5°$ horizontal resolution and the reanalysis data produced by the European Centre for Medium-Range Weather Forecasts (ECMWF) at T255 (0.703125 degrees) horizontal resolution. All sensitivity experiments to different parameterization schemes are conducted at two different initial times for 5-day integrations: one from 1200 UTC 30 September 2015 to 1200 UTC 5 October 2015 and another from 0000 UTC 29 September 2015 to 0000 UTC 4 October 2015.

3.2.3 Sensitivity experiments

The WRF model has multiple options for each type of physical parameterizations. These available options facilitate the study of the sensitivity of numerical simulations of Hurricane Joaquin to various physical processes and initial conditions. Thus, they not only help achieve a good simulation among many experiments but also help us understand the processes associated with hurricane evolution.

Three groups of sensitivity experiments are performed for different physical schemes. Specifically, experiments are conducted with three different cumulus schemes, three microphysics schemes and two boundary layer schemes in the ARW model. The boundary layer and microphysics are applied to all three domains, while the cumulus schemes are applied only to the 9-km and 27-km grid spacing domains. A summary of all sensitivity experiments is listed in Table 3.2.

3.2.4 A brief description of physical schemes in sensitivity experiments

3.2.4.1 Cumulus schemes

The cumulus convection schemes are responsible for predicting convective precipitation, changing vertical stability, generating and redistributing heat, removing and redistributing moisture, and making clouds. Convection has long been recognized as being centrally important in the development of tropical cyclones. The performance of a numerical model in TC forecasts depends on how well convection is parameterized in the model (e.g., Anthes 1977; Mandal et al., 2004). Even though cumulus schemes are important for the simulation of TCs, there is a limitation in the use of cumulus schemes at high resolutions (e.g., less than 10 km grid spacing).

Previous studies indicate that TC track and intensity appear to be highly sensitive to

the choice of cumulus parameterization (e.g., Biswas et al., 2014; Pattanayak et al., 2012; Nicholas 2003). However, the sensitivity results varied from case to case. In this study, three widely-used cumulus schemes are selected for the sensitivity experiments: the Kain-Fritsch, Betts-Miller-Janjic (BMJ), and the Old-Simplified Arakawa-Schubert (OSAS) scheme. The Kain-Fristch (KF) is a deep and shallow subgrid scheme using a mass-flux approach with downdrafts (Kain 2004; Kain and Fritsch 1993). Mixing is allowed at all vertical levels through entrainment and detrainment. This scheme removes convective available potential energy (CAPE) through vertical reorganization of mass at each grid point. The scheme consists of a convective trigger function (based on grid-resolved vertical velocity), a mass flux formulation, and closure assumptions. The Betts-Miller-Janjic (BMJ) scheme is an adjustment-type scheme for deep and shallow convection relaxing towards a reference profile of temperature and specific humidity determined from thermodynamic considerations. The Old Simplified Arakawa Schubert (OSAS) uses a stability closure, assumes a large cloud size, parameterizes moist downdrafts, and does not assume unrealistically large lateral mixing to simulate penetrative convection (Pan and Wu 1995).

3.2.4.2 Planetary boundary layer (PBL) schemes

The intensification of a TC depends heavily on its ability to extract heat and moisture from the upper layer of the sea through turbulent fluxes. This process takes place in the PBL. The Yonsei University (YSU) scheme (Hong and Dudhia 2003) and the Eta implementation of Mellor and Yamada (1982) by Janji´c (1994) (MYJ) are the two most popular schemes used in many studies. These two schemes differ in the way they calculate the surface flux and the vertical mixing in the PBL. YSU is a first-order closure,

nonlocal K scheme, while MYJ is a 1.5-order, local K scheme.

Some differences between the two schemes mentioned in previous case studies include the production of larger intensity and stronger secondary circulation in MYJ than in YSU (Nolan et al., 2009), and larger values of surface latent heat flux (LHFLX) in MYJ than in YSU at the same wind speeds (Hill and Lackmann 2009).

3.2.4.3 Microphysics (MP) schemes

Microphysics schemes control the formation and dissipation of cloud droplets and ice crystals, and influence precipitation prediction (e.g., Morrison et al., 2010). Previous studies show that in general, microphysics schemes do not have a major impact on track forecasts but do have an effect on the simulated TC intensity (Tao et al., 2011). Concentration of frozen hydrometeors and latent heat released during conversion of hydrometeors may be responsible for storm intensity (e.g., Kanase et al., 2015). Melting and evaporation help strengthen downdrafts and reduce the intensity and intensification rate (Wang and Wu 2003).

Three microphysics schemes that treat the hydrometeors differently are selected to investigate the sensitivity of TC intensity. Microphysical schemes are divided into two types, single moment and multiple moments, according to their treatments of hydrometeor particle size distribution. A single-moment scheme predicts only the mixing ratio while double-moment schemes predict both the mixing ratio and the number concentration for each hydrometeor species (Lim and Hong 2012). The WRF Single-Moment 6-Class Microphysics Scheme (WSM6) based on Hong and Lim (2006), is a single-moment scheme including cloud water, rain-water, pristine ice, snow, and graupel. The New Thompson scheme includes the same hydrometeors as the WSM6 scheme, but

it is a double-moment scheme for pristine ice (Thompson et al., 2004). A third scheme is the single-moment Eta Ferrier scheme, which is simple and efficient and uses diagnostic mixed-phase processes. As indicated in the WRF user guide, the Ferrier scheme includes only mixing ratios of cloud water, rain water and snow.

3.3 Results and discussion

3.3.1 Overall evaluation

Track and intensity forecasts are sensitive to initial times for all cumulus, microphysics, and boundary layer schemes. In general, simulations initialized at 1200 UTC 30 September 2015 produce better forecasts for both track and intensity. Details of the sensitivity results are described in section 3.3.2. The use of GFS analysis as boundary and initial conditions leads to better control simulation results than the use of the ECMWF analysis (Figure 3.2a). Hence, the sensitivity experiments for different physics schemes are conducted by using GFS final analysis data as initial and boundary conditions. The sensitivity of track and intensity to various physical schemes at different initial times is investigated and summarized in Table 3.3 and described in the following paragraphs.

3.3.1.1 Track

For all experiments that were initialized at 1200 UTC 30 September 2015, track simulations are significantly sensitive to cumulus schemes that, track simulations differed after the recurve. The sensitivities are not significant for microphysics or boundary layer schemes (Figure 3.2). Track errors range from 50 to 200 km during the integration periods for simulations with both boundary layer schemes – YSU and MYJ (Figure 3.3b).

For different microphysics schemes, the simulation with WSM6 leads to a better forecast than those with the Ferrier and the New Thompson schemes beyond 96-h forecasts. Specifically, track errors range from 50 to 200 km for the simulation with the WSM6 scheme and from 50 to 350 km for simulations with Ferrier and New Thompson schemes (Figure 3.3c).

For different cumulus schemes, the Kain-Fritsch scheme is the only cumulus scheme that results in correct simulation of the hairpin turn (Figure 3.2b). Before the 36-h integration, all simulations with three cumulus schemes show a similar track forecast with track errors of around 50 km (Figure 3.3a). Major track difference occurred after the hairpin turn. At the 120-h integration, the track error of the simulation with KF scheme remains within 200 km while it extends far beyond 1000 km for simulations with both the BMJ and OSAS scheme. Reason for this this discrepancy will be discussed.

3.3.1.2 Intensity

For the intensity simulations, none of the results from the WRF experiments match the best-track data. For the experiments with three cumulus schemes initialized at 1200 UTC 30 September 2015, the simulation with OSAS scheme simulates a much weaker storm than simulations with the other two schemes, though none of these schemes are good (Figure 3.4). The difference in minimum sea level pressure starts from around the 18 h forecast; for maximum wind, it starts from around the 36 h forecast, after the simulated storm in the simulation with OSAS cumulus scheme makes the hairpin turn. For boundary layer (Figure 3.5) and microphysics (Figure 3.6) schemes, the WRF simulations failed to capture the rapid intensification of Joaquin from 1200 UTC 30 September 2015 to 0600 UTC 2 October 2015 at both initialization times. However, the

sensitivity results differ at different lead times – intensity forecast is not sensitive to boundary layer or microphysics schemes for the experiments initialized at 1200 UTC 30 September 2015 while it is sensitive for experiments initialized 0000 UTC 29 September 2015. The influence of physics schemes to TC intensity will be discussed in next section.

3.3.2 Sensitivity to initial times

All simulations with various cumulus, boundary layer, and microphysics schemes are sensitive to initial time (namely, forecast lead time). In general, initializing at an earlier time significantly worsens the track simulations although exceptions exist. For the simulation with the cumulus scheme BMJ, when initialized at 0000 UTC 29 September 2015, it successfully simulates the recurve (Figure 3.7a). For the intensity simulation with different cumulus schemes, it can be seen that when initialized at an early time, TC intensities are weaker in simulations with all three schemes (Figure 3.4a).

For simulations with different boundary layer schemes, although forecasts with both YSU and MYJ schemes initialized at 0000 UTC 29 September 2015 produce successfully the recurve (Figure 3.7b), track errors are much larger than those initialized at 1200 UTC 30 September 2015. Despite the relatively large track errors, the simulation of TC intensity is compared. While TC intensity is not sensitive to different boundary layer schemes at 1200 UTC 30 September 2015, it starts to be significantly weaker in the simulation with the MYJ scheme than that with the YSU scheme after the 42-h integration for experiments initialized at 0000 UTC 29 September 2015 (Figure 3.5a). This difference can be partially explained by the large track difference; the track errors go beyond 600 km after the 84-h forecasts in simulations with the YSU and MYJ schemes (Figure 3.8).

For simulations with different microphysics schemes, track simulations are sensitive to initial times for the WSM6, Ferrier, and New Thompson schemes. Simulations with all these three schemes capture the hairpin turn. However, the recurve is counter clockwise instead of clockwise (Figure 3.7c) at 0000 UTC 29 September 2015. Moreover, track errors are much larger than when initialized at 1200 UTC 30 September 2015, as expected. For intensity, while all three schemes reproduce similar TC intensity at 1200 UTC 30 September 2015, the storm in the simulation with WSM6 is stronger than in those with two schemes after around the 42-h integration at this earlier initial time (Figure 3.6a). Again, this is probably due to the much larger track differences.

Hurricane Joaquin reaches the tropical storm stage at 0000 UTC 29 September 2015 and it is at hurricane stage at 1200 UTC 30 September 2015. Model results are much better when initialized at a relatively mature stage of TC.

3.3.3 Sensitivity to cumulus schemes

The different simulations of both core region structures and the large-scale environment could be the reason for the different TC forecasts. In the next two sections, diagnoses are conducted to investigate the possible factors controlling Joaquin's track and intensity.

3.3.3.1 Large-scale environment

The absolute vorticity tendency gives a very clear picture about when the north-westward movement occurs and how each storm moves in each level, especially in lower levels where the vortex is more clearly structured. For the simulation with Kain-Fritsch, the recurve occurs at the 39–42-h forecast (Figure 3.9); for the BMJ scheme, the recurve occurs at the 30–36-h simulation (Figure 3.10); for the OSAS scheme, the recurve occurs

at the 33–36-h simulation (Figure 3.11). The Hovmoller plots of south-north (S-N) and west-east (W-E) wind speed cross section centered at the storm center is plotted (Figure 3.12). The locations of the storm centers, marked by the eye where wind speeds are near zero, are similar before the 33-h integration for all three experiments. After this time, the movements diverge; the storms in simulation with BMJ and OSAS stop moving southward and their westward speeds are faster than that of the simulation with KF scheme. At the 60-h forecasts, the storm center in the simulation with BMJ is about 1 degree north and 1 degree west of that with the Kain-Fritsch; the storm center in the simulation with OSAS is about 1degree north and 1.25 degrees west of the storm center with the Kain-Fritch scheme.

The different simulations of both core region structures and the large-scale environment could be the reason for the different TC tracks. Since TC track is explained mainly by environmental steering, steering vectors, which are the average wind within a radius of 600 km from the storm center and the 850–200 hPa layer, are plotted for all three cumulus schemes to investigate the reason for the difference in track simulations (Figure 3.13a) at the 0–60-h time period. Large track differences between the KF and the other two schemes start at around the 27-h integration and end at 42 h. The directions of the steering vectors show good consistency with the directions of the KF, BMJ, and OSAS storms. In addition, steering vectors are not sensitive to the boundary layer or microphysics schemes (Figure 3.13b,c), which further demonstrated that environmental steering could be the main reason for different track simulations under different cumulus schemes. Hence, the comparison between the three schemes is performed during the hairpin turn (33–42-h simulations), focusing on the large-scale environment.

Steering vectors for low, middle and upper levels are also investigated at the 0-60 h simulations for different cumulus schemes (Figure 3.14). Results show that, at the 33–42-h forecasts, difference mainly occurs at the middle and upper levels. The time variation of midlevel steering is quite similar with the total steering (i.e., differences start at 27-h and end at around the 42-h integration).

Complex large-scale weather patterns, including strong areas of high pressure aloft over the northern Atlantic Ocean, a strong high pressure near the surface of the earth nosing southward along the East Coast, a mid- to upper-level trough over the eastern United States and remnants of Tropical Storm Ida in the Atlantic, are major reasons for the large uncertainty of the steering flow.

For the geopotential height fields, the three schemes are similar in the lower and outflow levels. The largest difference occurs at the middle level (500 hPa) as shown in Figure 3.15. The high-pressure region to the southwest of Joaquin is much stronger in the KF scheme than in the BMJ or OSAS scheme during the 33–39-h integration. It noses northeastward and connects with the high pressure near the surface of the earth nosing southward along the East Coast. Hence, the geopotential height to the north-west of Hurricane Joaquin in the simulation with the KF scheme is higher than the simulations with other two schemes – much higher than in the simulation with BMJ scheme and slightly higher than in that with the OSAS scheme. At the 42-h integration, the southwest high region significantly weakens in all three schemes. As a result, the northwest blocking high in the KF simulation also weakens at this time.

A mid- to upper-level trough over the eastern United States exists in the simulation of all three schemes, which is assumed to be the reason for the northward clockwise hairpin turn of Joaquin. Due to the existence of the blocking high, the KF storm is

separated from the trough at the 33–39-h integration. In the mean time, as indicated by the 5838-m geopotential height contour, Hurricane Joaquin in the simulations with the BMJ scheme and the OSAS scheme is connected to the trough and starts to move northeastward. At the 42-h integration, along with the disappearance of the blocking high, the storm in the simulation with KF scheme finally moves to the trough (also indicated by the 5838-m geopotential height contour) and is steered by it.

The large-scale wind fields further confirm that the track difference can be explained by the steering theory. At the "blocking high" region at the 33-h and 36-h integration, wind speed is near zero in the simulation with the KF scheme. It ranges between 6 and 9 m/s in the simulation with the BMJ scheme and between 4 and 9 m/s in the simulation with OSAS scheme (Figure 3.16). At the 42-h integration, the northward wind speed in the simulation with the KF scheme increases to around 5 m/s as the southwest high weakens. It is also noted that wind speed at the front of the trough is also different between the simulations with three schemes at the middle levels. The wind speed in the simulation with the BMJ scheme is significantly stronger than in the simulations with other two schemes (400 hPa is shown as an example in Figure 3.17). However, since the northeastward wind speed is equal or even weaker in the simulation with the OSAS scheme than in that with the KF scheme, the wind in front of the trough should have little influence on steering Hurricane Joaquin. Besides, conventionally the wind fields within 500–700 km of the storm center are considered to be steering. Hence, the blocking high at 500 hPa seems to play a more important role than the mid- to upper-level trough in leading to different steering flows.

The third significant difference in the large-scale environment is that the remains of Tropical Storm Ida, located east of Hurricane Joaquin, are much weaker in the simulation

with the KF scheme than in the simulation with the BMJ or the OSAS schemes. However, since Joaquin is the stronger storm in the binary cyclone system, the influence of Ida on Joaquin's track simulation should be small.

3.3.3.2 Possible reason for different steering

In this section, the reason why the simulated large-scale environments are different in the simulations with the three schemes is discussed, focusing mainly on the formation of the south-west high-pressure region in the KF scheme. As stated previously, the existence of the blocking high in the simulation with the KF scheme is the result of this strong high-pressure region. This region noses north-westward and connects with the surface to mid level high along the East Coast to block the storm in the simulation with KF scheme from steering by the trough.

Different distribution of heat is the main reason for the different distribution of pressure fields. As can be seen from the temperature fields at different levels during the 33-42 h forecasts, temperature is much higher in the simulation with KF scheme than in the simulations with BMJ or the OSAS schemes at lower to middle levels to the south of Hurricane Joaquin. Using 700 hPa as an example, nearly the whole area to the southwest of Joaquin shows temperatures higher than 283 K in the KF scheme (Figure 3.18). Only a few regions show temperatures higher than 283 K in the simulation with OSAS scheme, and that with the BMJ scheme is even colder. Since atmospheric layer thickness is proportional to temperature, a warmer lower to mid level region produces a stronger high-pressure region at around 500 hPa in the simulation with the KF scheme.

All three cumulus experiments start from the same initial condition. The east-west cross section at 20 degrees north is selected to investigate the evolution of environmental

temperature. As can be seen from the 0–60-h integration of the east-west cross section of temperature at 20 degrees north at 850 hPa, a large difference between the simulation with the KF scheme and simulations with the other two schemes starts at the 6-h integration (Figure 3.19). After this time, temperatures to the southwest of Joaquin are continuously higher in the KF scheme than in the BMJ or OSAS schemes.

3.3.3.3 Thermal structure and TC intensity

The reason for different simulations of TC intensity should be found in the inner-core structure of the TCs. As shown in Figure 3.12, the evolution of wind speed distribution is similar between simulations with the KF and the BMJ schemes, while the simulation with OSAS scheme is much weaker. From the MSLP and MSW plots, the 18 h and 33–36 h are two break points in the intensity difference. The former marks the time when the storm in the simulation with OSAS starts to become weaker than the other two simulations in MSLP, while the latter marks the time when the storm in the simulation with OSAS suddenly weakens in MSW.

To investigate the reason why the storm in the simulation with OSAS is much weaker than the storms in simulations with KF or BMJ, core region characteristics are investigated. The time series of warm-core structure (the temperature anomaly averaged over 0.5 degrees from the storm center) and azimuthal wind speed (20 to 60 km mean radius) are plotted for all three experiments. The evolution of the temperature anomaly and wind structure correlates well (Figure 3.20). For the simulation with KF scheme, when the upper-level temperature anomaly starts to intensify at the 18-h simulation, the MWS also starts to increase. It is the same for the simulation with the BMJ scheme (at 21 h integration) and the OSAS scheme (at 24-h integration). Another common feature in the

three experiments is that when the temperature anomaly is significantly higher at the lower or middle levels, a corresponding region of low wind speed exists, for instance, at around the 12-h integration in the simulation with the KF scheme and at the 15-h integration in simulations with BMJ and OSAS schemes. In addition, all three storms experience intensification after the warm-core height increases. Hence, it can be assumed that the intensity of the TC is highly correlated with the core region temperature structure in this case. It can be further assumed that the TC intensity is positively correlated with the upper-level temperature anomaly.

The core region thermal structure is significantly different in the simulation with the OSAS scheme than in those with the other two schemes. First, the upper-level temperature anomaly intensifies at a slower speed in the simulation with the OSAS scheme. Second, before the storm in the simulation with OSAS makes the hairpin turn at the 33-h integration, the core region temperature anomaly suddenly decreases at the lower to middle levels. At last, after the recurve of the OSAS storm at the 36-h simulation, the warm-core height of the OSAS storm significantly lowers and suddenly stops intensifying. Meanwhile, the temperature anomaly and azimuthal wind speed in the other schemes continue to increase.

The first difference can explain the relatively low MSLP in the OSAS scheme in the 18-33-h integration through the assumption that TC intensity is positively related to the upper-level temperature anomaly. The second and third differences are related to the sudden decrease in MSW at the 36-h simulation, which will be discussed next.

3.3.3.4 The sudden decrease in MSW

Since the core region structures are quite similar in the simulations with KF and BMJ schemes, only the KF scheme is discussed. The reason for the sudden weakening of MSW at the 33–36-h integration is discussed by comparing the core region structures of the KF and OSAS schemes.

First, what leads to the different thermal structures is discussed. To investigate the sudden decrease of temperature at lower levels at 33 h, precipitation at domain 3 during this time period is investigated. However, no big difference exists between the two schemes at the 30–33-h forecasts (Figure 3.21). The surge of lower-level cooling may not be caused by the evaporation of rain. For diabatic heating, which can be estimated as the apparent heat source Q (Yanai et al., 1973):

$$Q = \frac{T}{\theta}\left(\frac{\partial \theta}{\partial t} + u\frac{\partial \theta}{\partial x} + v\frac{\partial \theta}{\partial y} + \omega\frac{\partial \theta}{\partial p}\right) \quad (2)$$

where θ is potential temperature, T is temperature. At 1800 UTC 1 October 2015, a difference does exist between the two schemes in the core regions but it is not significant. At 2100 UTC 1 October 2015, the simulation with OSAS scheme clearly shows a stronger diabatic cooling than the simulation with KF scheme from 850 to 500 hPa (Figure 3.22). The diabatic cooling could be one reason for the sudden surge in the cold-core region at the lower to middle levels.

After the recurve of storm in the simulation with the OSAS at 0000 UTC 2 October 2015, diabatic heating in the core- region differs mainly in the upper levels (500–250 hPa); the cooling in the OSAS scheme is much stronger at 250 hPa (Figure 3.23). For vertical motion, significant difference occurs at 0000 UTC 2 October 2015 (36 h simulation), where strong downdraft occurs in the middle levels in the OSAS scheme

(Figure 3.24). Meanwhile, a strong downdraft is found in the middle levels in the OSAS storm. Hence the significant change in warm-core structure could be caused because strong diabatic cooling at the middle to upper-levels during the 33–36 h integration makes the upper-level air negatively buoyant and leads to strong downdrafts at the middle levels. The warming at lower to middle levels for the OSAS storm at the 36-h integration could be caused by the strong mid level downdraft through adiabatic heating.

A symmetric TC is in approximate thermal wind balance. The core region of a TC is highly inertially stable, which means the vortex is not likely to interact with the environment and will stay symmetric. Hence, the radial gradient of temperature can be related to the vertical shear of tangential wind (thermal wind):

$$\frac{\partial u_g}{\partial z} = -\frac{R}{fH}\frac{\partial T}{\partial r} \tag{3}$$

where u_g is geostrophic wind, and R is the gas constant. When the wind speed decreases with height, wind shear is expected to be negative. When the temperature increases from the storm center, dT/dr > 0; when the temperature increases toward the storm center, dT/dr < 0. Theoretically, $\frac{\partial T}{\partial r}$ would reduce in the lower levels and increase in the upper levels when the warm-core height decreases. At the 36-h simulation, since the maximum positive temperature anomaly is located at around 600 hPa, $\frac{\partial T}{\partial r}$ is expected to be negative at this level and $\frac{\partial u_g}{\partial z}$ is expected to be positive. Tangential wind shear is plotted at the 30-, 33-, and 36-h simulations for both the KF and OSAS schemes (Figure 3.25). Its distribution can be well explained by the thermal wind balance theory that a positive $\frac{\partial u_g}{\partial z}$ region suddenly occurred at around 600 hPa (4–6 km). However, how the change in tangential wind shear leads to the significant decrease in wind speed cannot be clearly

explained. But the change in thermal structure has great impact on the change in wind fields.

3.3.4 Effects of cumulus schemes on TC track and intensity

Although the cumulus schemes were absent in the inner 3-km domain, both the intensity and track forecasts are sensitive to the choice of cumulus scheme in the outer grids. In the Joaquin case, different simulation of temperature plays an important role in both track and intensity simulations.

Cumulus schemes represent subgrid-scale updraft and downdraft and generally produce column moisture tendency. In the core regions, the distribution of azimuthally averaged vertical velocity and moisture from the storm center to 500 km are similar before 0600 UTC 1 October 2015 (0000 UTC 1 October 2015 is shown as an example in Figure 3.26). After this time, though varied at each time, a general trend is that the updraft in the eye-wall region is stronger in simulations with the KF and BMJ schemes than in simulation with the OSAS scheme. Meanwhile, the moist air near the surface is transported to higher levels. Specifically, at 1200 UTC 1 October 2015, the 90% relative humidity contour extends to above 400 hPa in simulations with the KF and BMJ schemes, while it stays below 800 hPa in the simulation with OSAS scheme. The stronger convection and moisture transport lead to a stronger warm core in the eye. At the 36-h integration, a strong downdraft leads to a significant decrease in moisture in the eye region and destroys the warm-core structure in the simulation with OSAS scheme.

In the large-scale environment, the convection is much weaker than in the core region. The release of latent heating by the cumulus clouds from condensation and precipitation is critical for sustaining large-scale disturbances and mesoscale flows (Kuo 1974; Adler

and Rodgers 1977). However, cloud fractions are near zero for all three experiments at the lower to middle levels to the southwest of Joaquin. How different cumulus schemes lead to different simulations of temperature at lower levels remains unknown.

3.3.5 Impact of boundary layer schemes to TC intensity

Surface latent heat flux (SLHF), which is directly related to boundary layer schemes and impacts TC intensity is investigated. Three specific times, 1800 UTC 30 September 2015, 0000 UCT 1 October 2015, 0000 UTC 3 October 2015 are selected (Figure 3.27). The two schemes mainly differ at the radius of 0-200 km, where the convection is intense. Both the YSU and MYJ schemes show an increment in the SLHF from the initial time 0000 UTC 29 September 2015 to 1200 UTC 30 September 2015. However, the change in the MYJ simulation is much more significant than that in the YSU simulation at selected times, despite that the change in MSLP is relatively similar for both schemes. For the YSU scheme, the SLHF increased for 500 wm^{-2} for a 45 hPa increments in MSLP (comparing between 1800 UTC 30 September 2015 and 0000 UTC 3 October 2015 for the experiment initialized at 0000 UTC 29 September 2015); for the MYJ scheme, the SLHF increased for 1200 w m^{-2} for a 30 hPa increments in MSLP (comparing between 0000 UCT 1 October and 0000 UTC 3 October 2015 for the experiment initialized at 0000 UTC 29 September 2015). Different lead time can be a factor that lead to this difference. The SLHF is positively related to TC intensity. When the TC is viewed as a heat engine, a larger amount of heat received from the sea surface indicates that more energy can turn into work (kinetic energy) in the TC.

3.3.5 Impact of microphysics schemes to TC intensity

The influence of microphysics schemes on the distribution of different water phases is investigated at two specific times, 1800 UTC 30 September 2015 and 0600 UTC 2 October 2015. Rain and snow mixing ratio, two parameters that are distributed below and above the freezing level, respectively, and can potentially impact latent heat release at low and upper levels, are selected.

At 1800 UTC 30 September 2015, simulated TC intensities are similar for simulations with the WSM6, Ferrier, and New Thompson schemes; the MSLP is around 990 hPa for experiments initialized at 0000 UTC 29 September 2015 and 970 hPa for that initialized at 1200 UTC 30 September 2015. At this time, the rain water mixing ratio show an increment of around $1\times 10^{-5} kg/kg$ for all three schemes from the earlier initial time to the later initial time (Figure 3.28). The value of the snow mixing ratio is largest in the New Thompson scheme and smallest in the WSM6 scheme for both initial times (Figure 3.29). However, large increments occur from 0000 UTC 29 September 2015 to 1200 UTC 30 September 2015, as for the rain water mixing ratio.

At 0600 UTC 2 October 2015, the storm in the simulation with WSM6, with an MSLP of 955 hPa, is much stronger than in simulations with the two other schemes for simulations initialized at 0000 UTC 29 September 2015. For experiments initialized at 1200 UTC 30 September 2015, the experiments with all three schemes show similar simulated TC intensities (around 960 hPa) at this time. The rain water mixing ratio in the simulation with the WSM6 scheme is larger than in simulations with the other two schemes by about $1\times 10^{-5} kg/kg$. For the snow mixing ratio, the changes between the two initial times are relatively small.

The above results show that TC intensity is positively correlated with the rainwater mixing ratio: comparing between experiments, those with a larger rainwater mixing ratio simulate a higher TC intensity; for each experiment, TC intensity is larger when the rainwater mixing ratio is higher. The relationship between the snow mixing ratio and TC intensity is not as clear as for the rainwater mixing ratio. In spite of TC intensity, the snow mixing ratio is always highest in the simulation with the New Thompson scheme and lowest in the experiment with the WSM6 scheme.

3.4 Summary

The numerical simulations of Hurricane Joaquin using GFS analysis data are better than those using ECMWF analysis data. For all sensitivity experiments, forecast lead time shows impact on both track and intensity forecasts. Among all the simulation results, the Kain-Fritsch scheme, together with the WSM6 and YSU schemes, initialized at a more mature stage of TC (1200 UTC 30 September 2015) leads to the best-track simulation.

The selection of different cumulus schemes could significantly impact both track and intensity forecasts. The midlevel environmental steering can be the reason that leads to different tracks in the simulations with different cumulus schemes. In particular, a high-pressure system blocked the northward motion of the storm in the simulation with the Kain-Fritsch cumulus scheme during the hairpin turn. In addition, since three experiments produce differences in the distribution and amounts of the latent heating, discrepancies occur in the intensity forecasts.

Table 3.1 Summary of model domain setup

Domain	Dimensions (x,y,z)	Grid size (km)	Time step (s)
D01	227× 188 × 37	27	90
D02	355× 355 × 37	9	90
D03	619× 685 × 37 (0000 UTC 29 Sep 2015)	3	90
	613× 589 × 37 (1200 UTC 30 Sep 2015)		

Table 3.2 Summary of sensitivity experiments

	Sensitivity Experiments	CU	MP	BL	Initial/boundary conditions
1	Cumulus (CU)	Kain-Fritsch/ BMJ/Old Simplified Arakawa-Schubert	WSM6	YSU	GFS-ANL
2	Microphysics (MP)	Kain-Fritsch	WSM6/Ferrier/ New Thompson	YSU	GFS-ANL
3	Boundary Layer (BL)	Kain-Fritsch	WSM6	YSU- sfclay_physics =1 MYJ- sfclay_physics =2	GFS-ANL
4	Initial and boundary conditions	Kain-Fritsch	WSM6	YSU	GFS-ANL/ ECMWF

Table 3.3 Sensitivity results for experiments at different initial times

Significance of sensitivity (yes/no)		Cumulus schemes	Microphysics schemes	Boundary layer schemes
Initial time: 0000 UTC 29 Sep 2015	track	yes	no	no
	intensity	yes	yes	yes
Initial time: 1200 UTC 30 Sep 2015	track	yes	no	no
	intensity	yes	no	no

WRF-ARW domain configuration

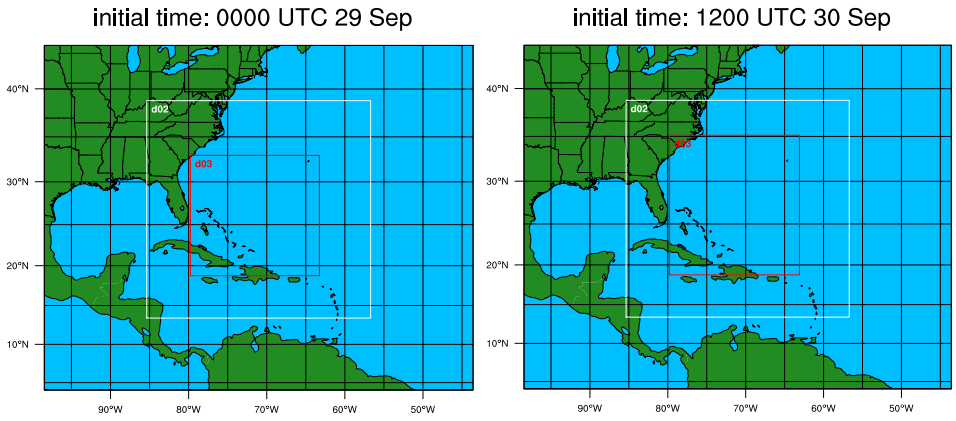

Figure 3.1 WRF-ARW domain configuration. Domain 2 is highlighted by white box, while domain 3 is highlighted by red box.

Hurricane Joaquin (initial time: 1200 UTC 30 Sep)

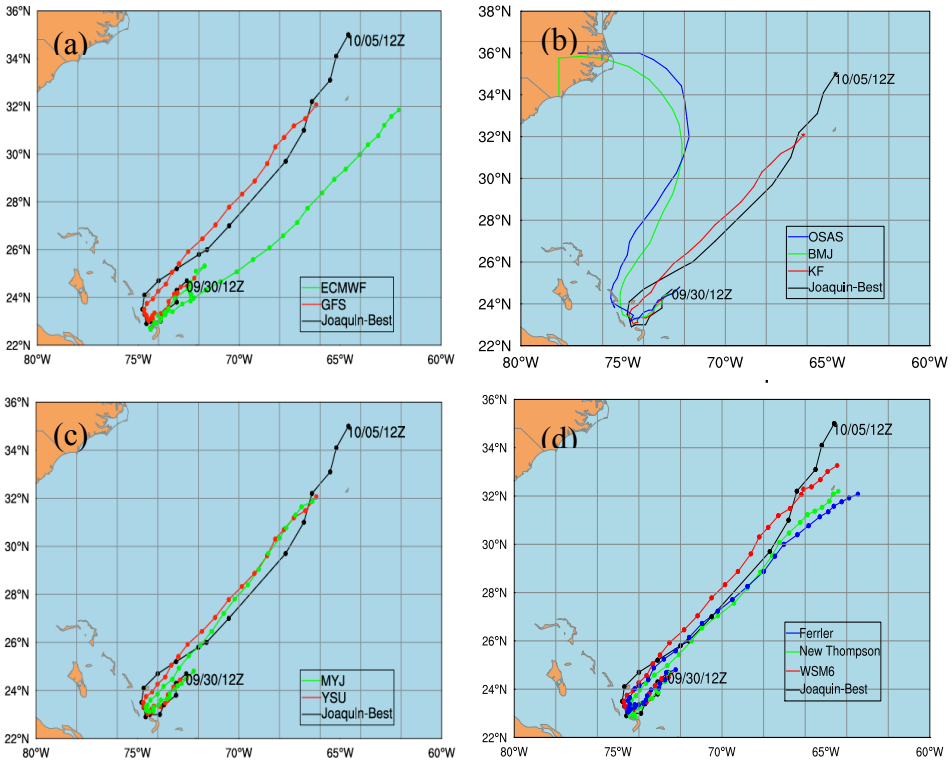

Figure 3.2 Track simulations initialed at 1200 UTC 30 Sep 2015 for different a) initial and boundary conditions; b) cumulus schemes; c) planetary boundary layer schemes; d) microphysics schemes.

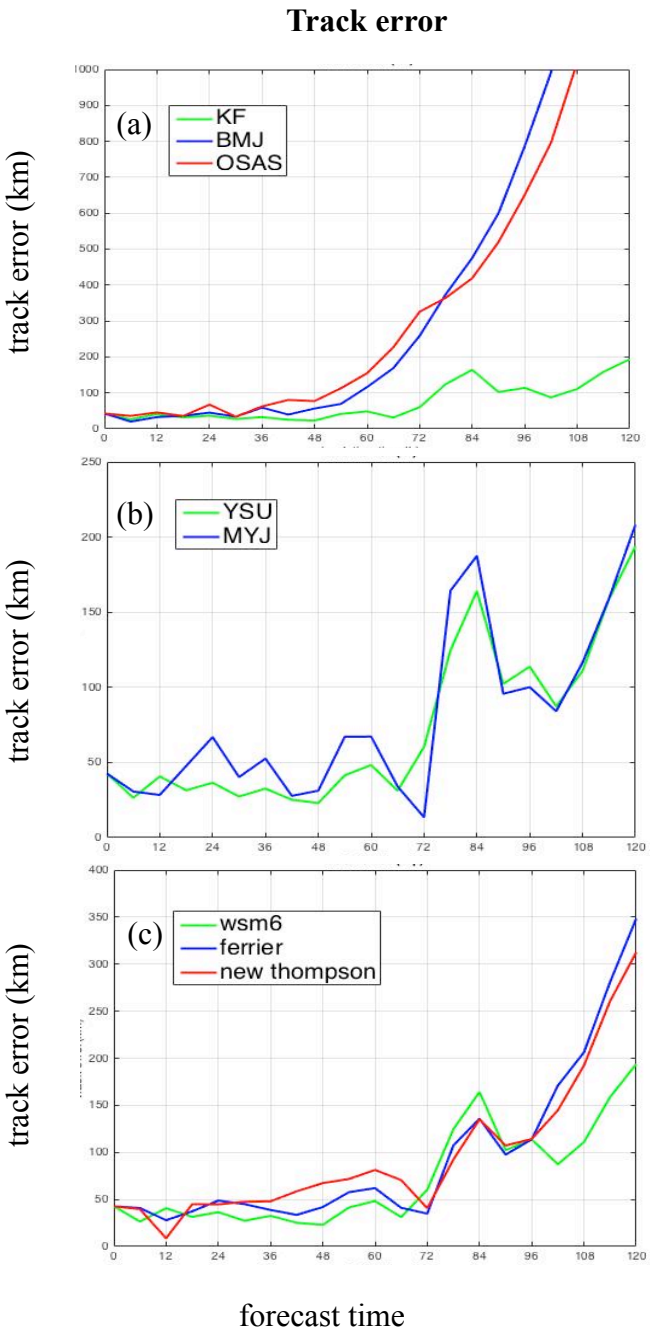

Figure 3.3 Track errors from different experiments initialized at 1200 UTC 30 Sep 2015 for sensitivity experiments with a) cumulus; b) boundary layer, and c) microphysics schemes during 120-h integration.

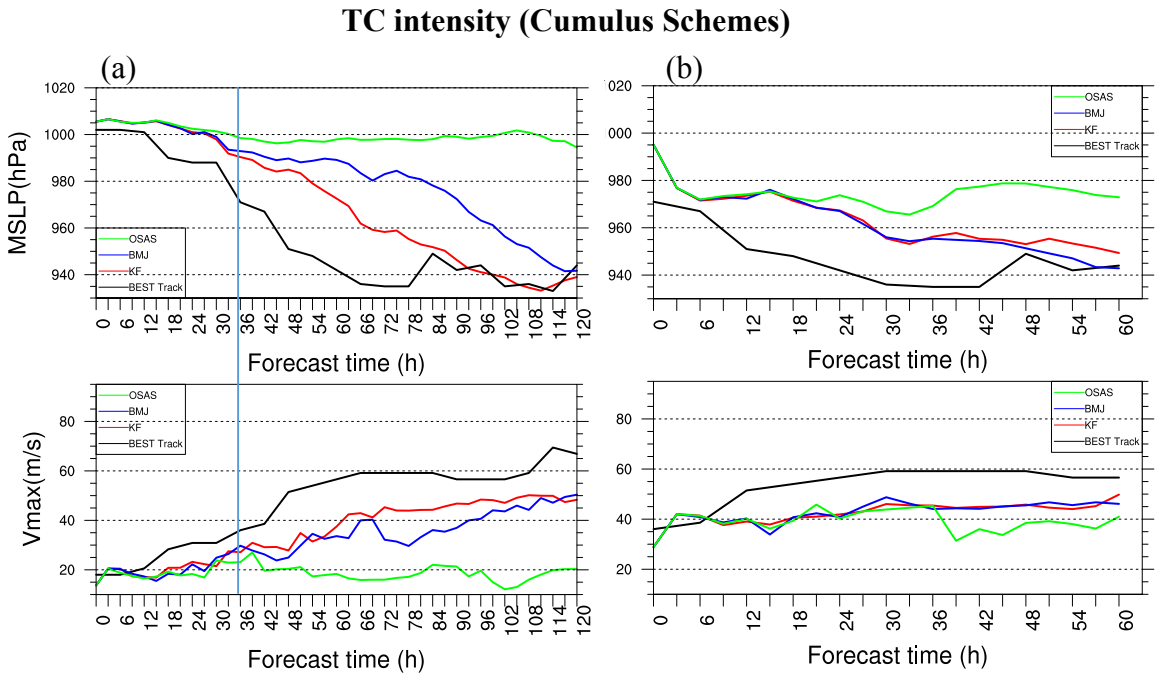

Figure 3.4 Intensity simulations represented by MSLP and MSW for the three cumulus schemes initialized at 0000 UTC 29 Sep 2015 (left) and 1200 UTC 30 Sep 2015 (right).

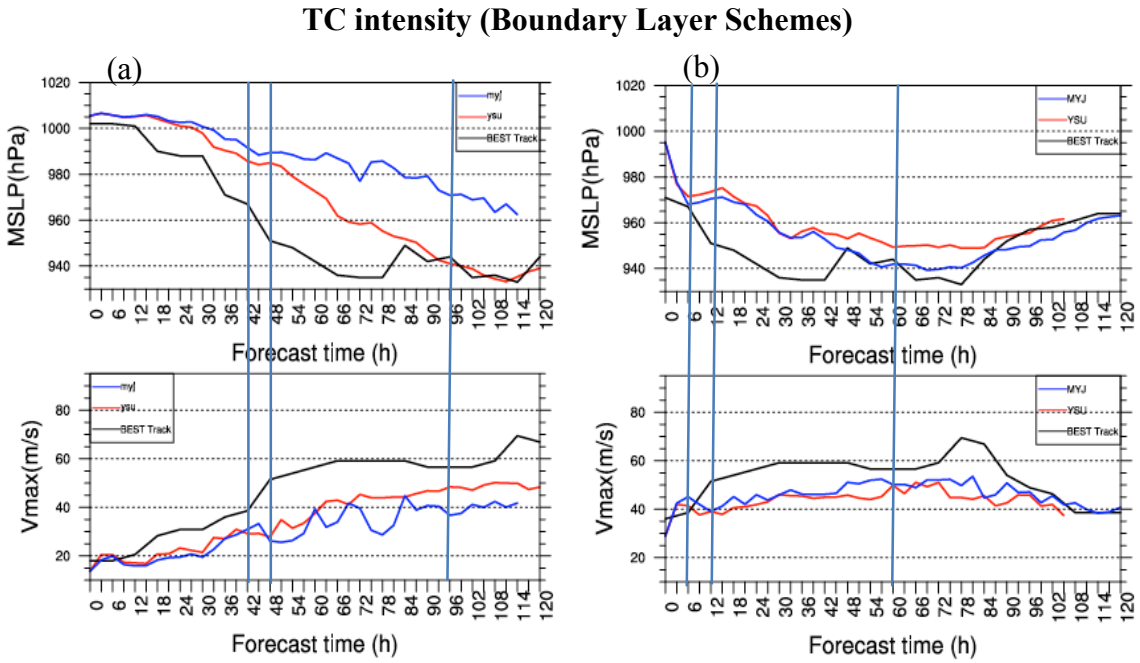

Figure 3.5 Intensity simulations represented by MSLP and MSW for the MYJ and the YSU schemes initialized at 0000 UTC 29 Sep 2015 (left) and 1200 UTC 30 Sep 2015 (right). 1800 UTC 30 Sep 2015, 0000 UTC 1 Oct 2015, and 0000 UTC 3 Oct 2015 is marked by the blue lines.

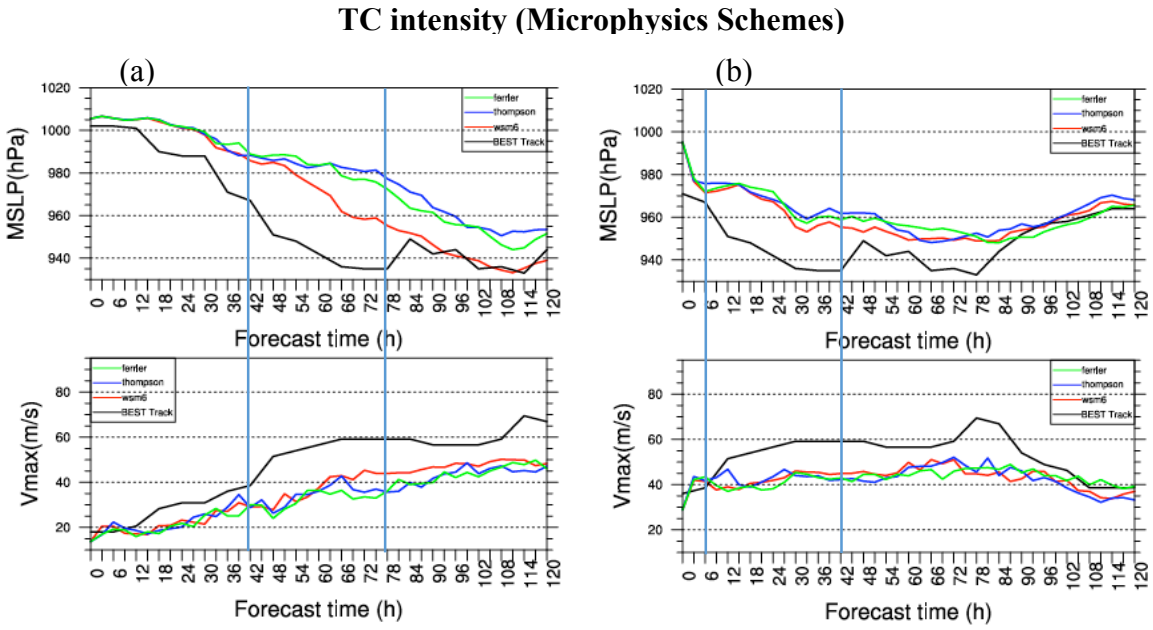

Figure 3.6 Intensity simulations represented by MSLP and MSW for the three microphysics scehems initialized at 0000 UTC 29 Sep (left) and 0012 UTC 30 Sep (right). 1800 UTC 30 Sep and 0600 UTC 2 Oct is marked by the blue lines.

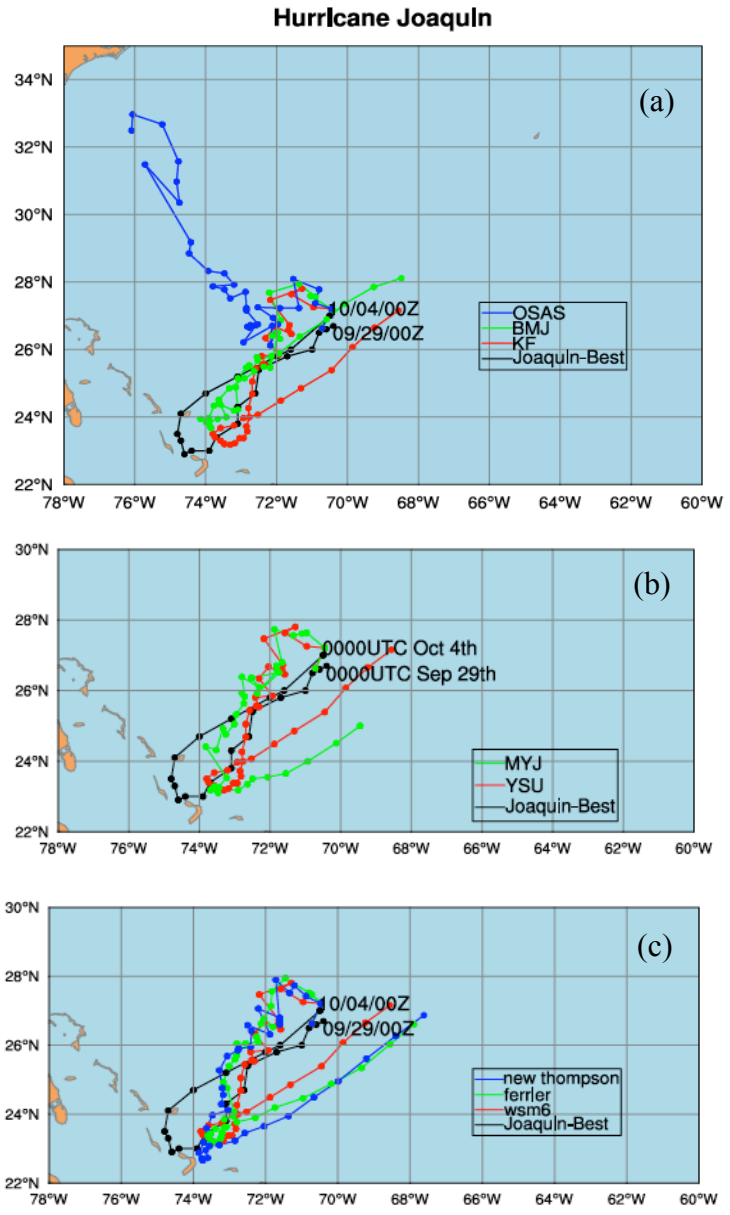

Figure 3.7 Track simulations for a) cumulus schemes, b) boundary layer shemes, and c) microphysics schems (lower) initialized at 0000 UTC 29 Sep 2015.

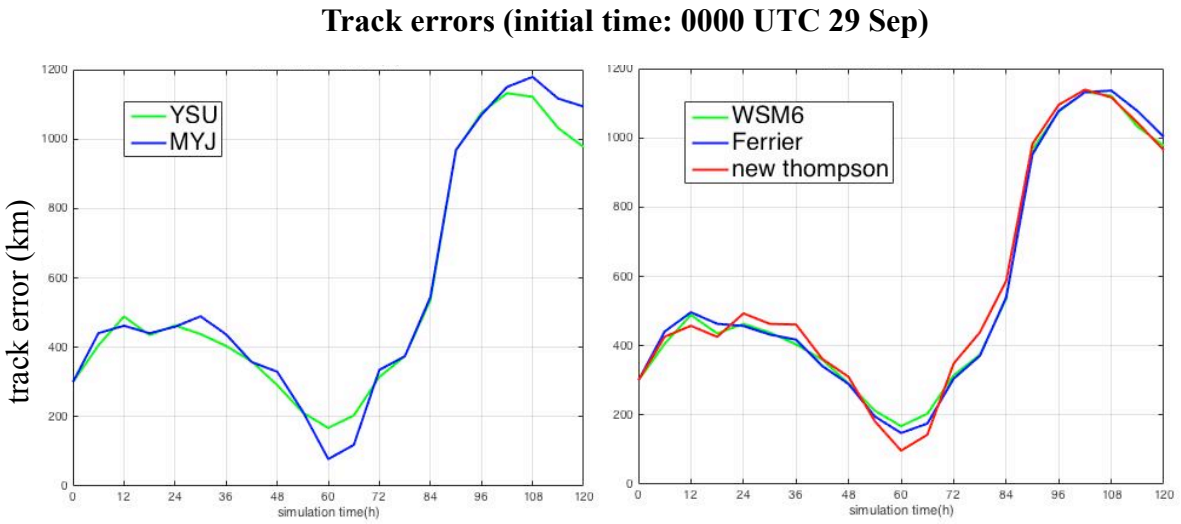

Figure 3.8 Track errors (units: km) for the boundary layer schemes (left) and microphysics schemes (right) during the 120 h simulations (0000 UTC 29 Sep–0000 UTC 4 Oct 2015).

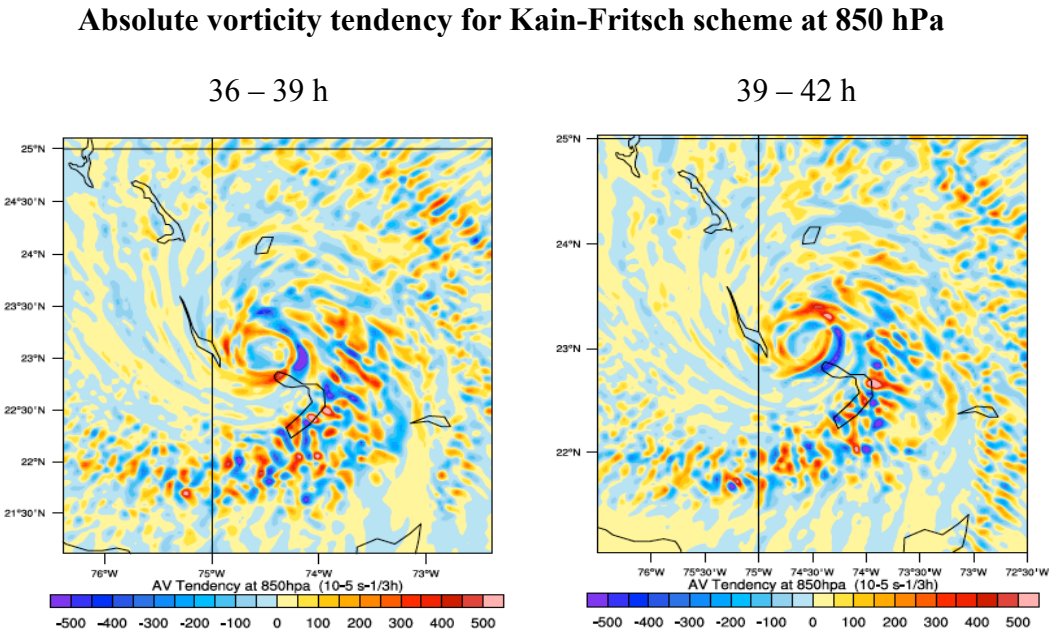

Figure 3.9 Absolute vorticity tendency at 850 hPa for the Kain-Fritsch scheme at 36–39-h forecast (left) and 39–42-h forecast (right).

Absolute vorticity tendency for BMJ scheme at 850 hPa

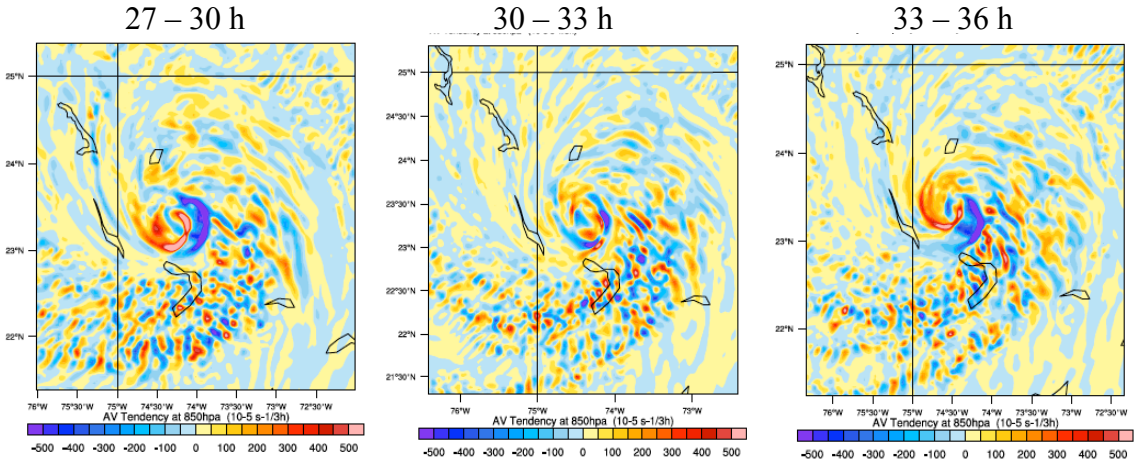

Figure 3.10 Absolute vorticity tendency at 850 hPa for the BMJ scheme at 27–30, 30–33, and 33–36-h integrations, respectively.

Absolute vorticity tendency for OSAS scheme at 850 hPa

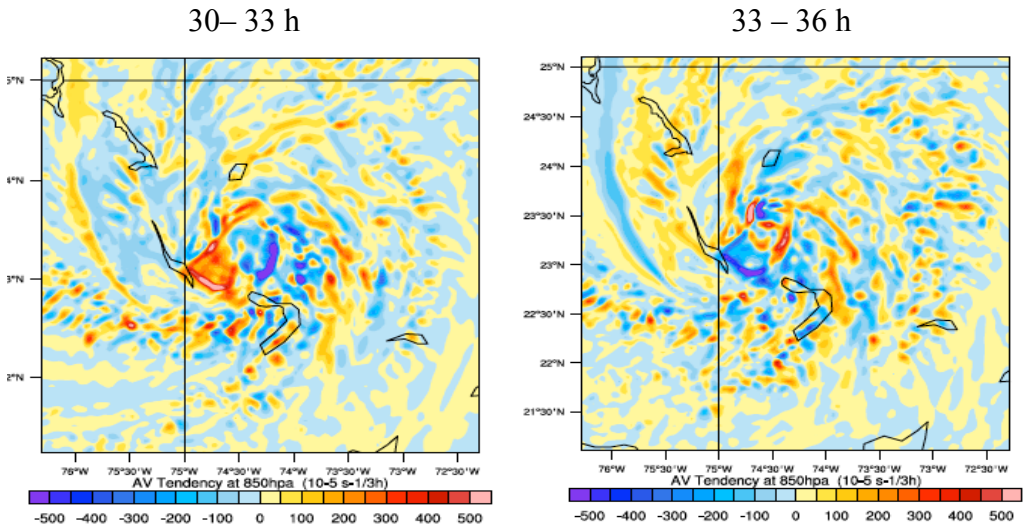

Figure 3.11 Absolute vorticity tendency at 850 hPa for the OSAS scheme at 30–33-h simulation (left) and 33–36-h simulation (right).

Hovmoller plots of wind speed at 850 hPa

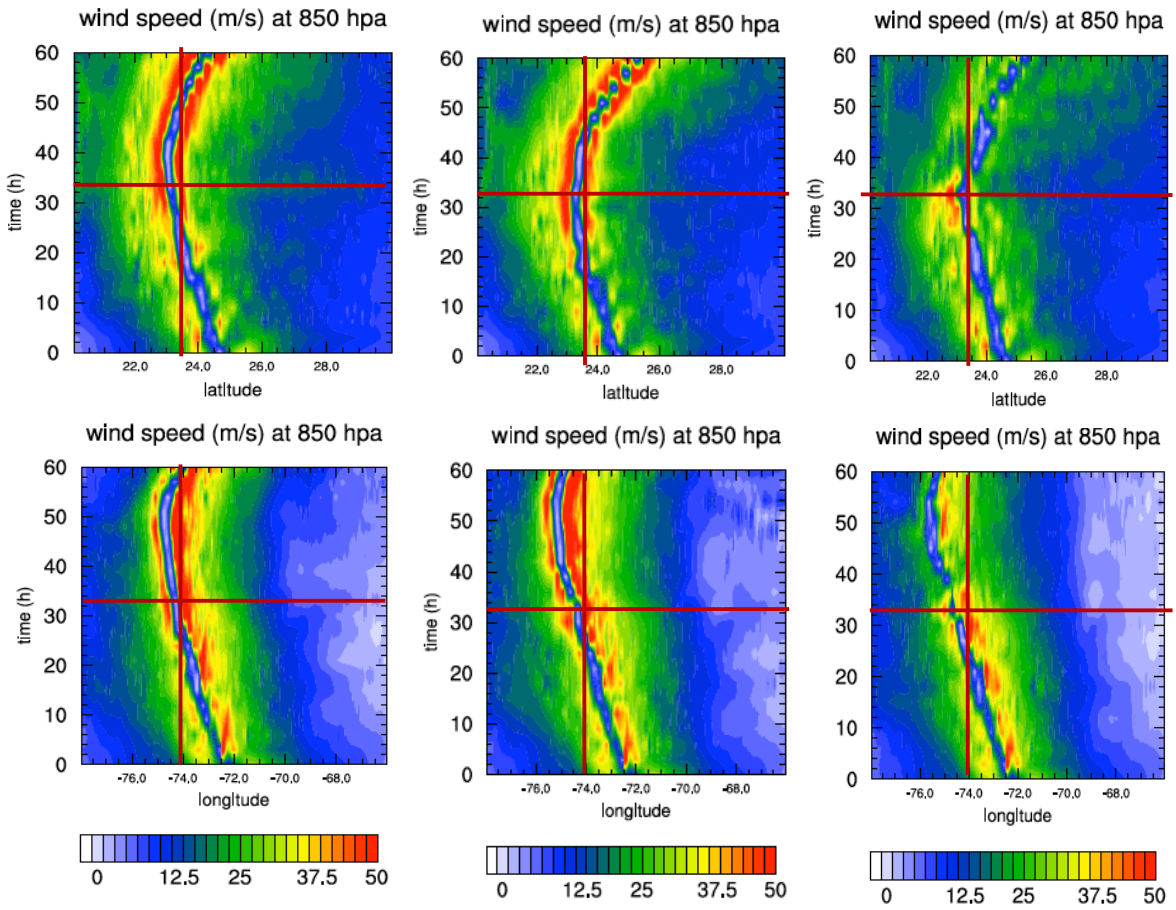

Figure 3.12 The 0–60-h time evolution of 850 hPa wind speed across storm center in S-N (upper) and W-E (lower) directions. Left column: KF scheme; middle column: BMJ scheme; and right column: OSAS scheme. Horizontal red lines indicate forecast hour of 33h.

Steering vectors (initial time: 1200 UTC 30 Sep)

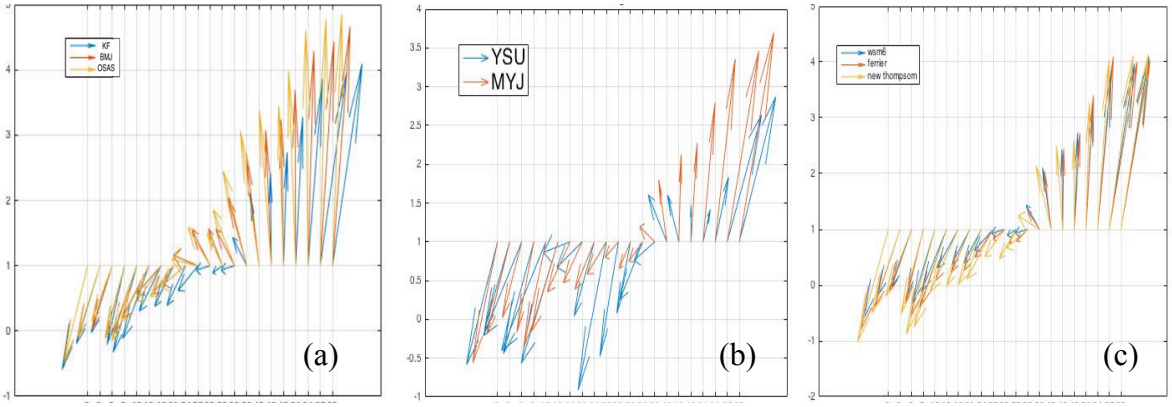

Figure 3.13 Steering vectors (units: m/s) at 1200 UTC 30 Sep 2015 to 0000 UTC 3 Oct 2015 for different a) cumulus schemes, b) microphysics schemes, and c) boundary layer schemes.

Steering vectors for cumulus schemes at different levels

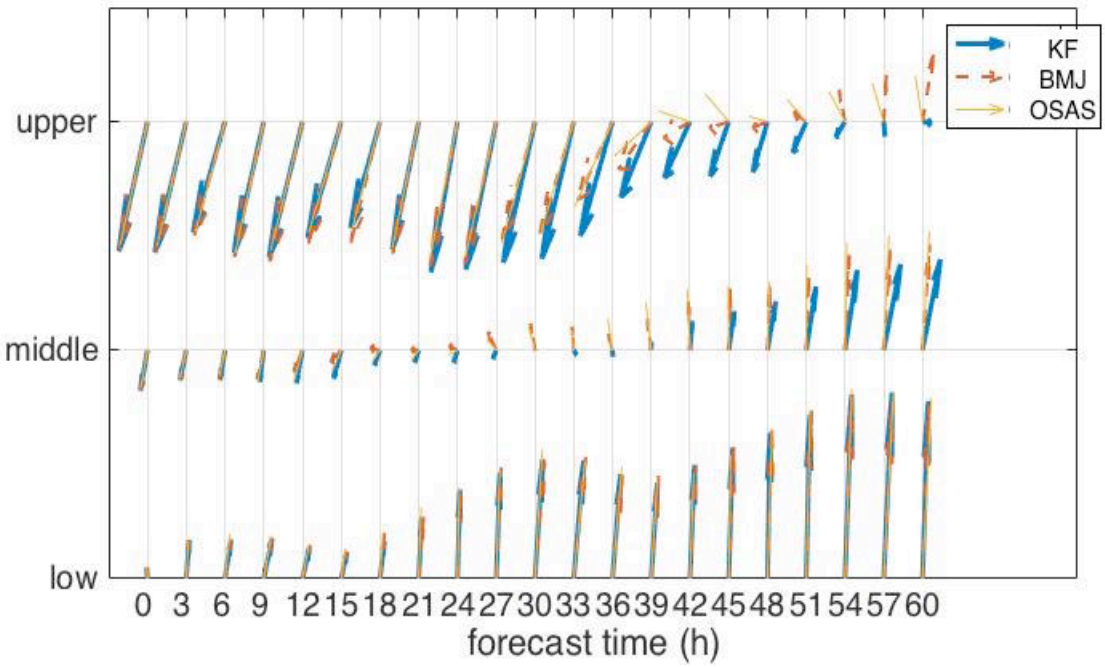

Figure 3.14 Steering at low, middle, and upper levels for the cumulus schemes at 1200 UTC 30 Sep 2015 to 0000 UTC 3 Oct 2015.

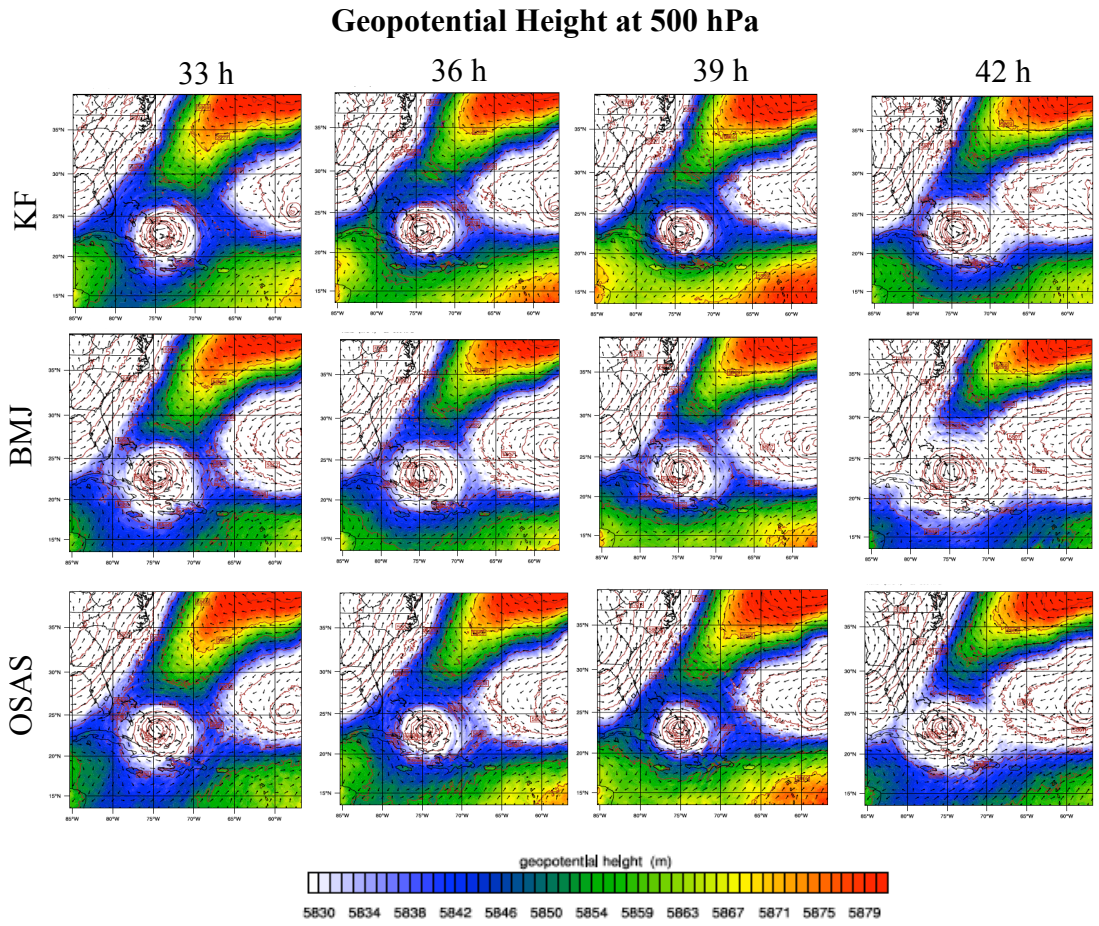

Figure 3.15 Geopotential height (units: m) at 500 hPa for the KF scheme (upper), BMJ scheme (middle), and the OSAS scheme (low) at 33, 36, 39, and 42-h simulaitons.

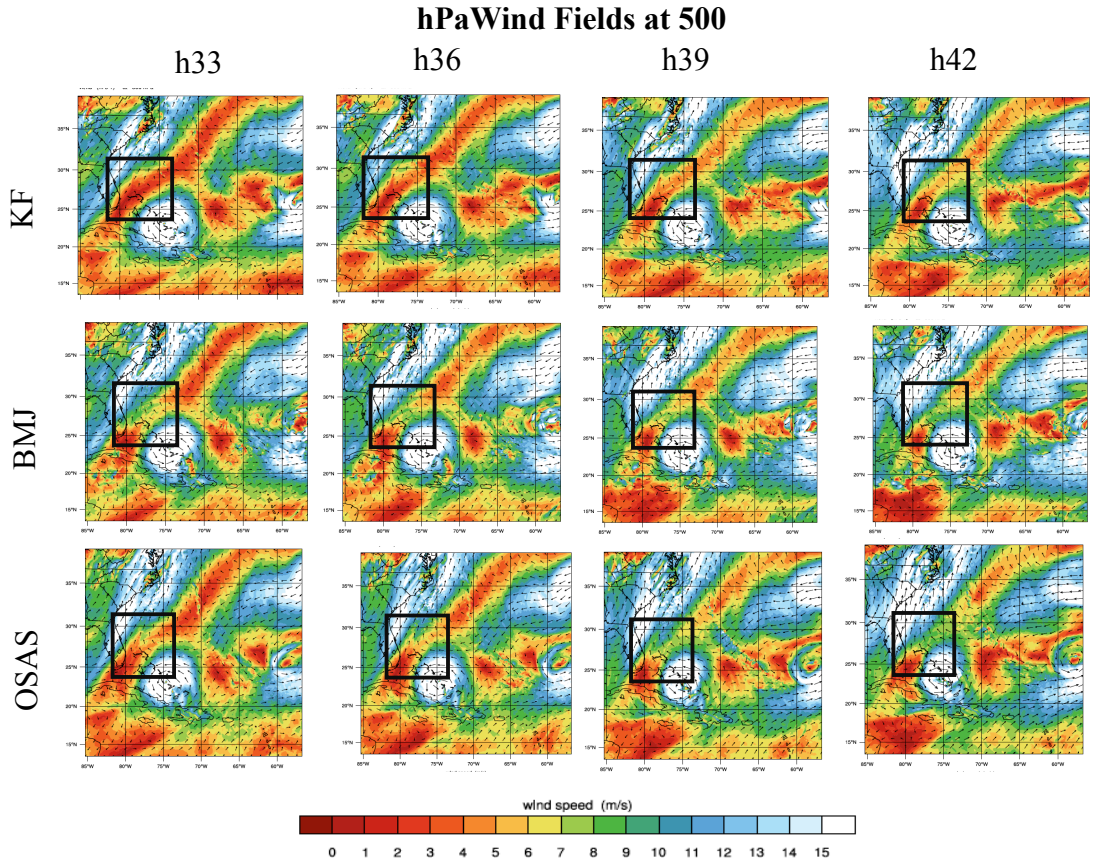

Figure 3.16 Domain 2 wind speed (units: m/s) at 500 hPa for the KF scheme (upper), the BMJ scheme (middle), and the OSAS scheme (lower) at 33, 36, 39 and, 42-h simulaitons.

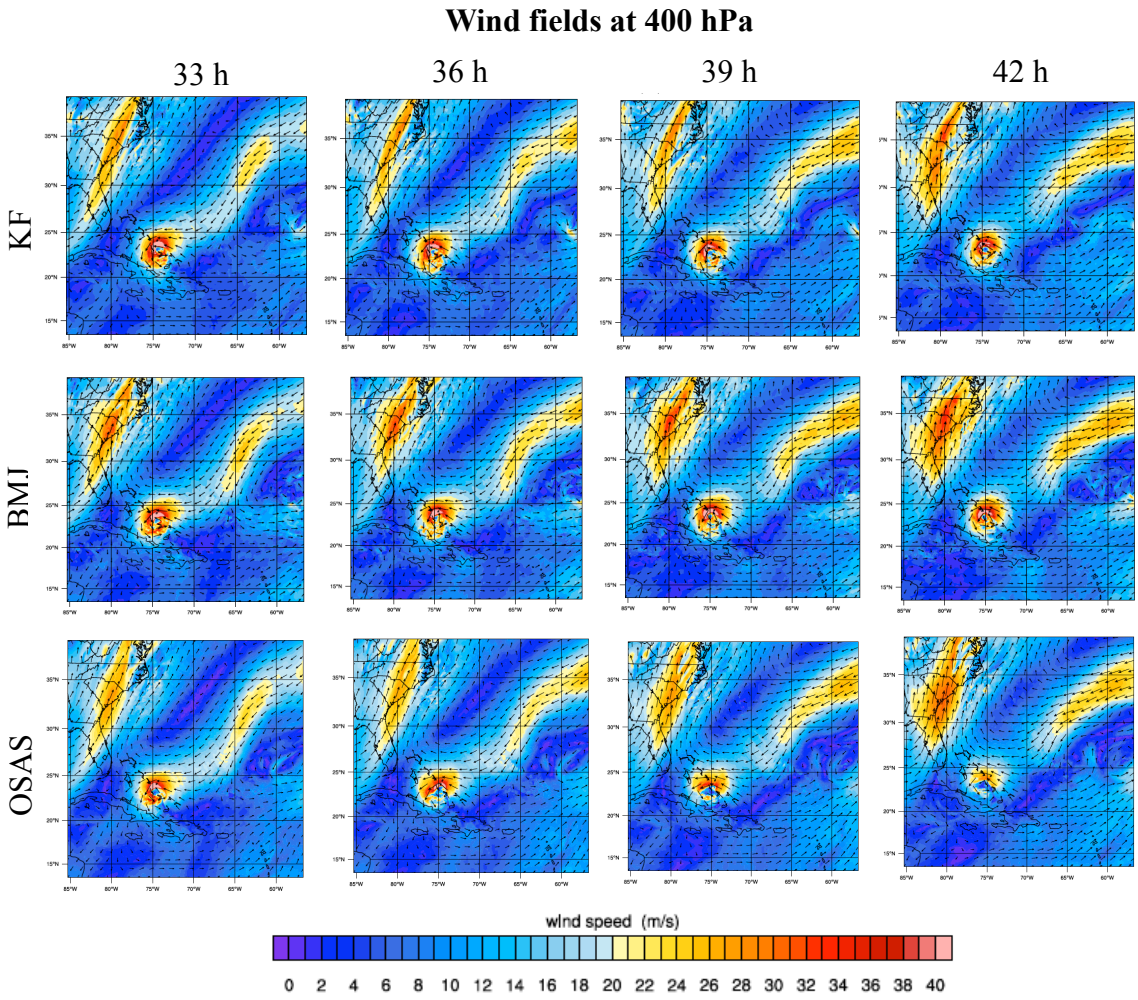

Figure 3.17 Wind speeds (units: m/s) at 400 hPa for the KF scheme (upper), the BMJ scheme (middle) and the OSAS scheme (lower) at 33, 36, 39, and 42 h simulations.

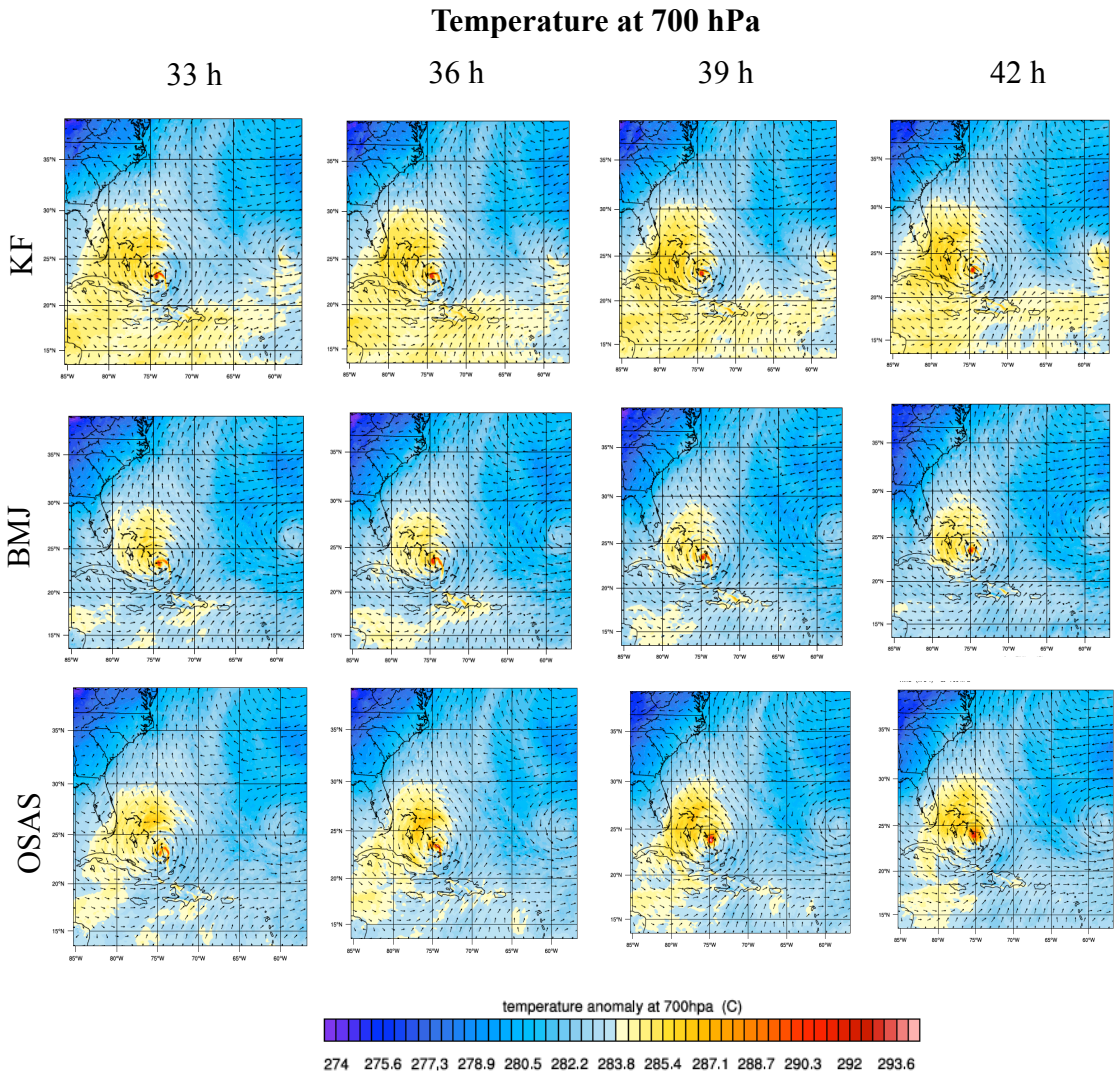

Figure 3.18 Temperature (units: K) at 700 hPa for the KF scheme (upper), the BMJ scheme (middle) and the OSAS scheme (lower) at 33, 36, 39, and 42 h simulations.

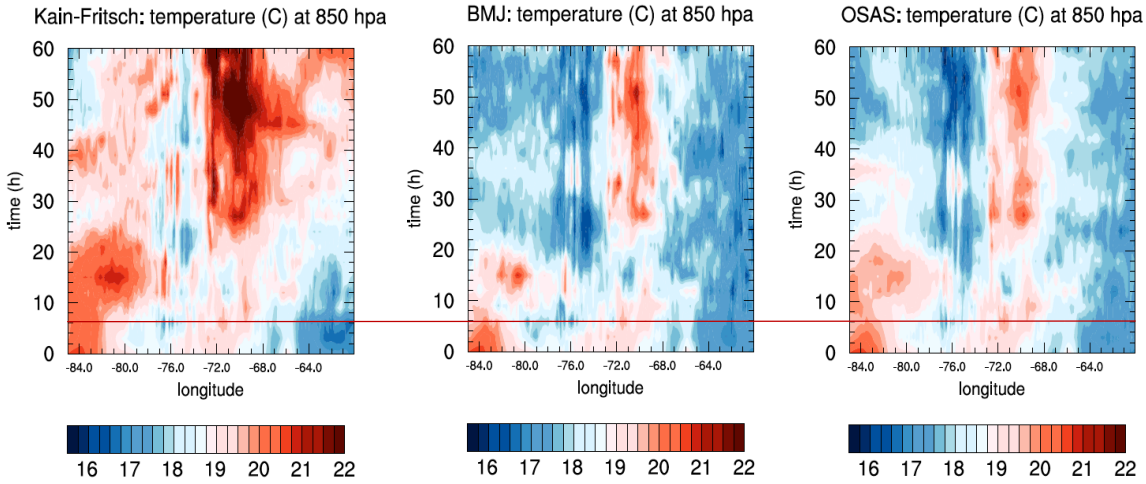

Figure 3.19 Time variations of E-W temperature (units: C) at 20 N at 850 hPa for the KF scheme (left), the BMJ scheme (middle), and the OSAS scheme (left) for the 0–60-h simulations.

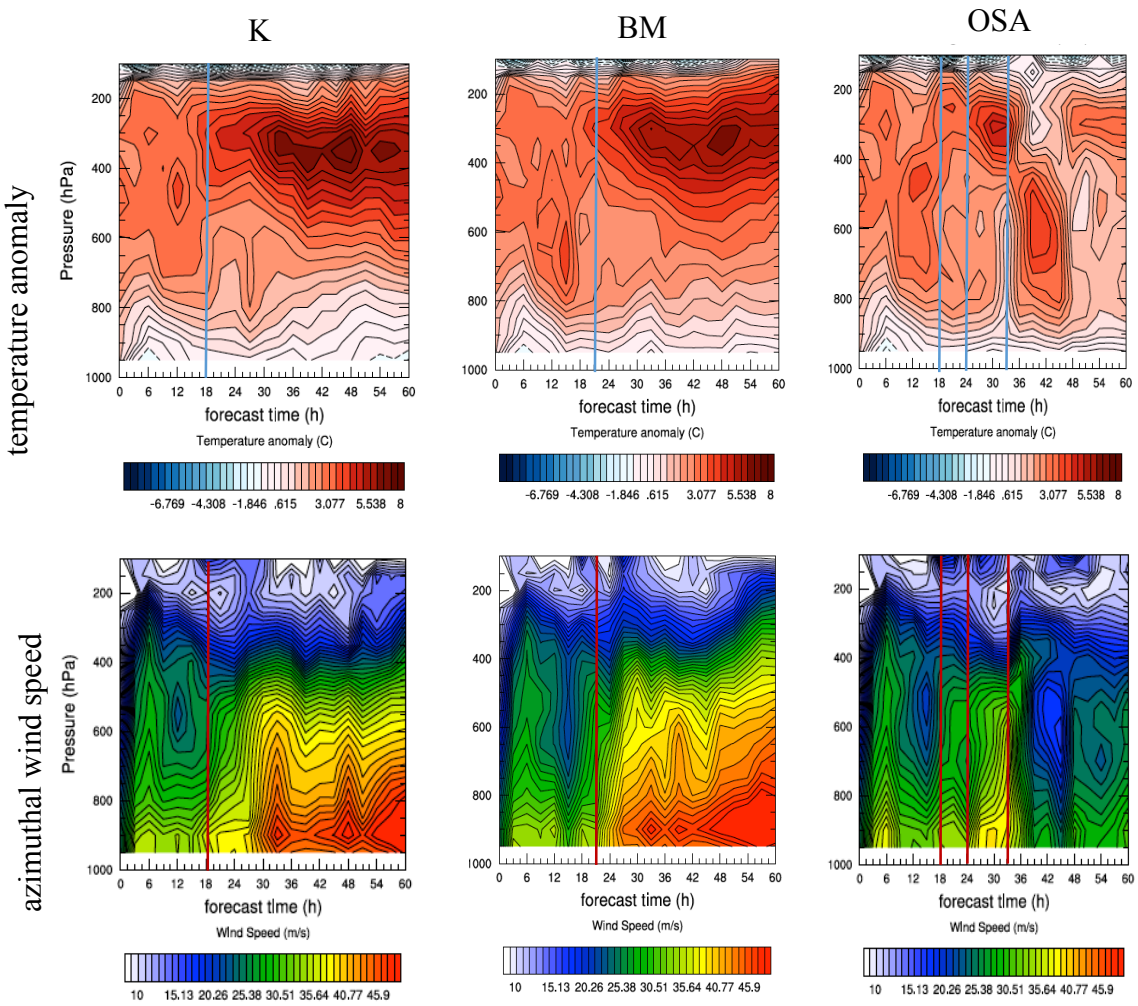

Figure 3.20 Time series of 0–60-h simulations of temperature anomaly (units: C, top) at storm center and azimuthal wind speed (units: m/s, bottom) at around radius of maximum wind for the KF scheme, the BMJ, and the OSAS scheme, respectively.

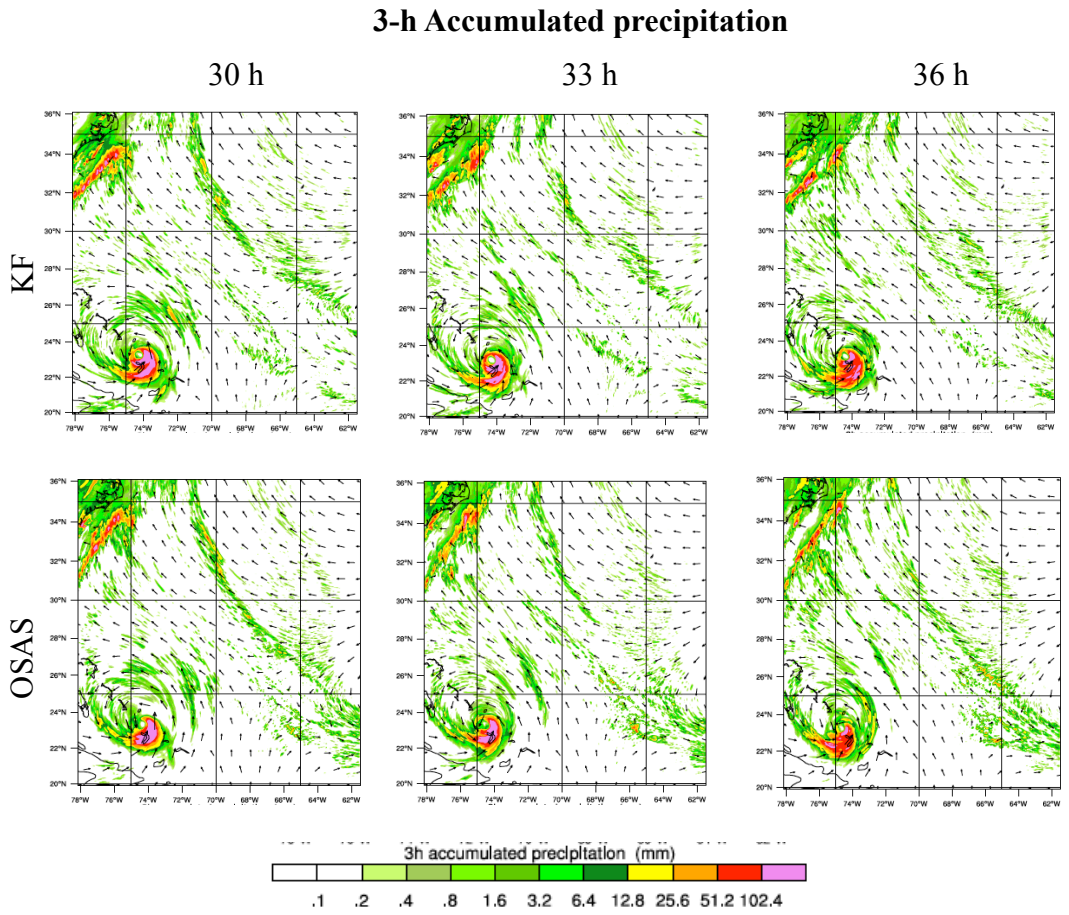

Figure 3.21 3-h accumulated precipitation (units: mm) at Domain 3 for the KF scheme (upper row) and the OSAS scheme (lower row) at 30-, 33-, and 36-h simulations.

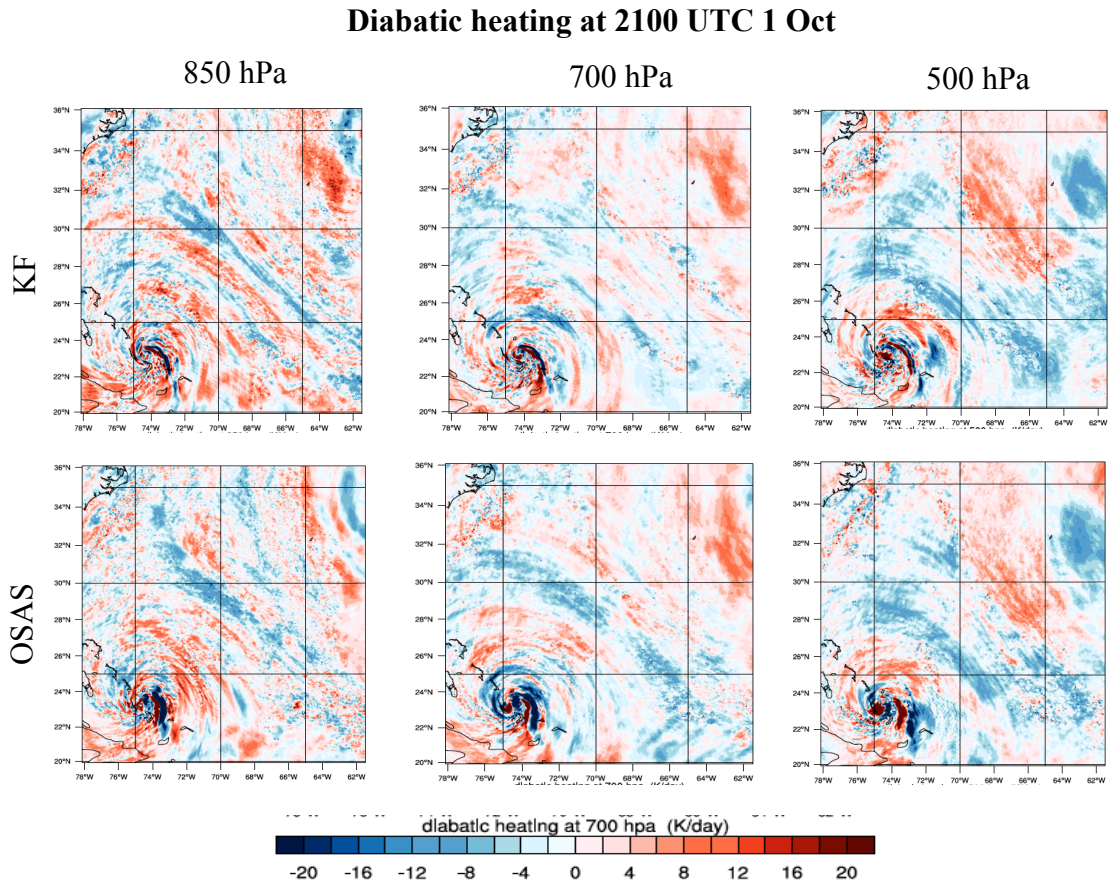

Figure 3.22 Diabatic heating (units: K/day) at Domain 3 for the KF scheme (upper row) and the OSAS scheme (lower row) at 850 hPa (left), 700 hPa (middle), and 500 hPa (left) at 2100 UTC 1 Oct 2015.

Diabatic heating at 0000 UTC 2 Oct

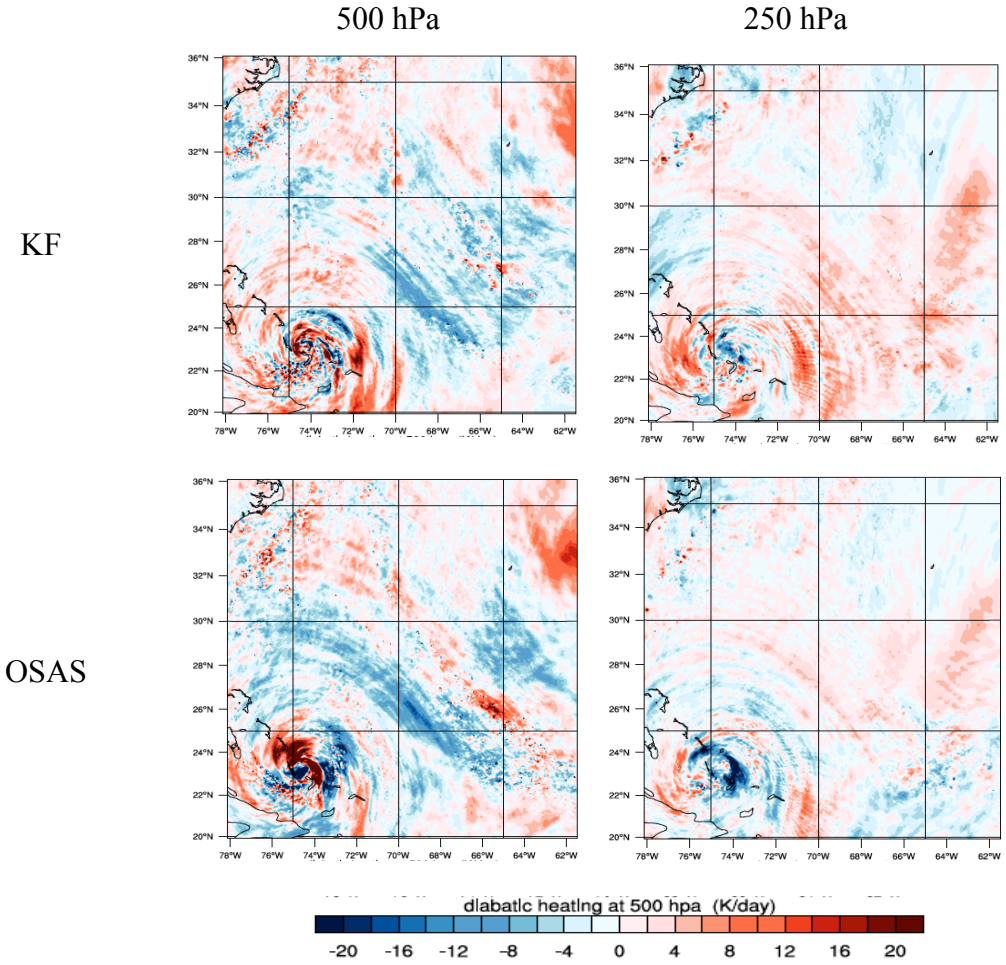

Figure 3.23 Diabatic heating (units: K/day) at Domain 3 for the KF scheme (upper) and the OSAS scheme (lower) at 500 hPa (left) and 250 hPa (right) at 0000 UTC 2 Oct 2015.

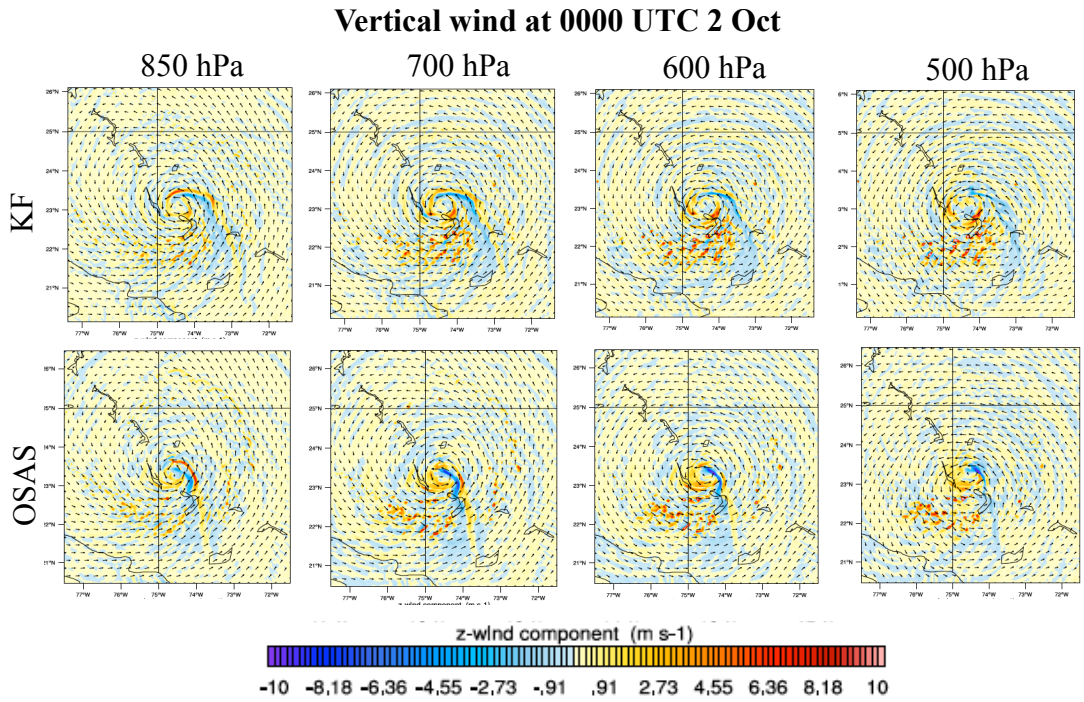

Figure 3.24 Vertical wind speed (units: m/s) for the KF scheme (upper) and the OSAS scheme (lower) at 0000 UTC 2 Oct 2015 at 850, 700, 600, and 500 hPa, respectively.

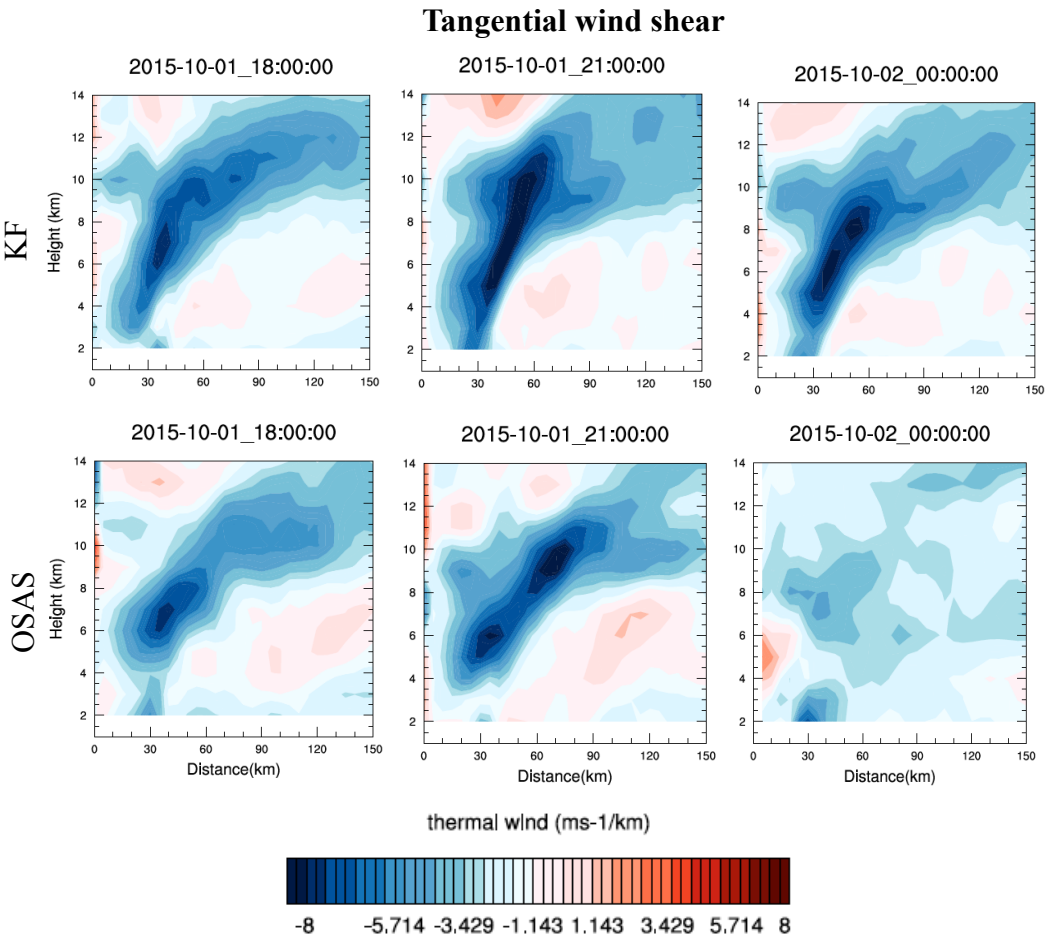

Figure 3.25 Azimuthally averaged tangential wind shear (units: ms/km) for the KF scheme (upper) and the OSAS scheme (lower) at 30-, 33-, and 36-h simulations at 0–150 km radius.

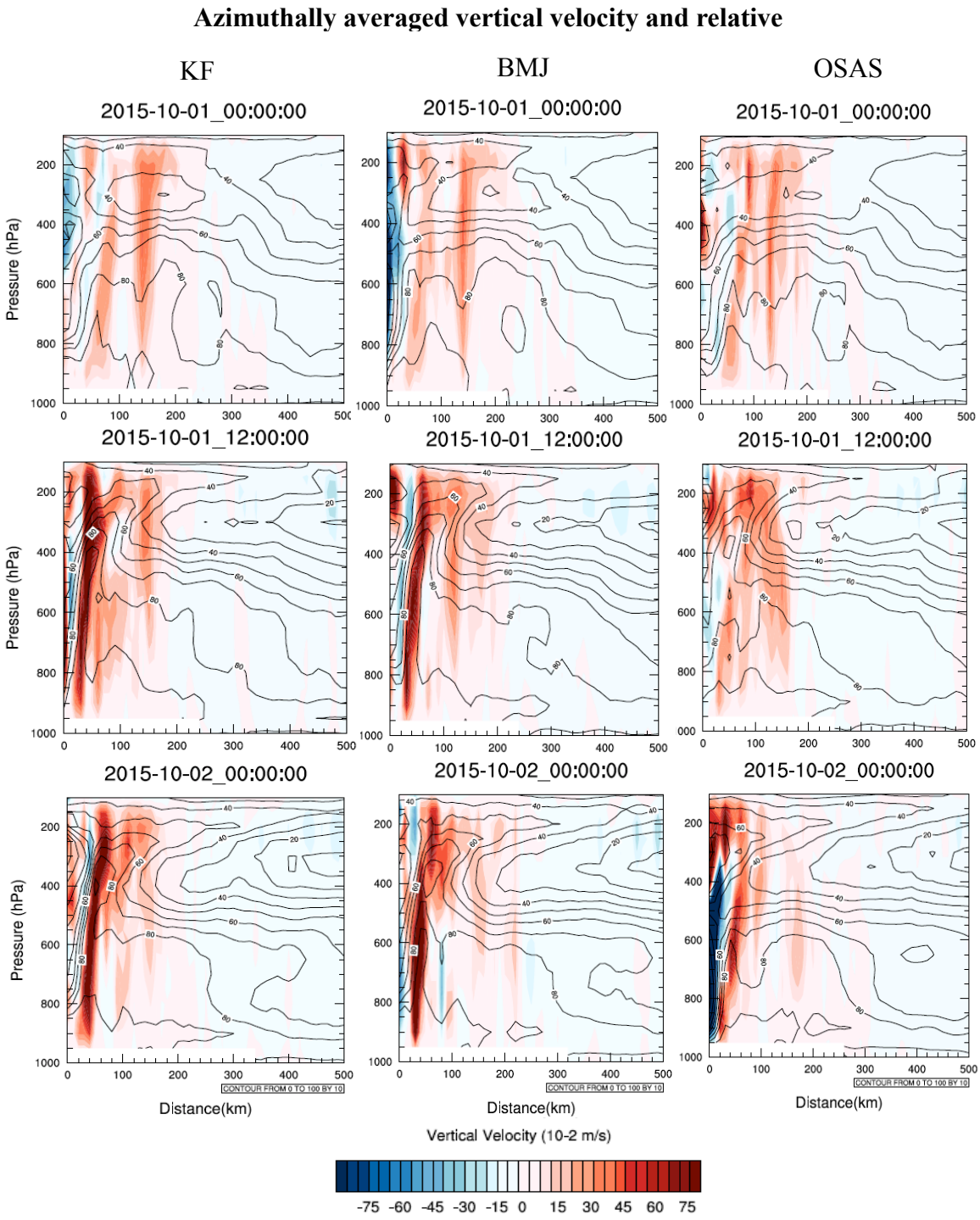

Figure 3.26 Azimuthally averaged vertical velocity (units: 10^{-2} m/s) and relative humidity (units: %) at 0-500 km from storm center for the KF scheme (left), the BMJ scheme (middle) and the OSAS scheme (right) at 0000 UTC 1 Oct, 1200 UTC 1 Oct, and 0000 UTC 2 Oct 2015.

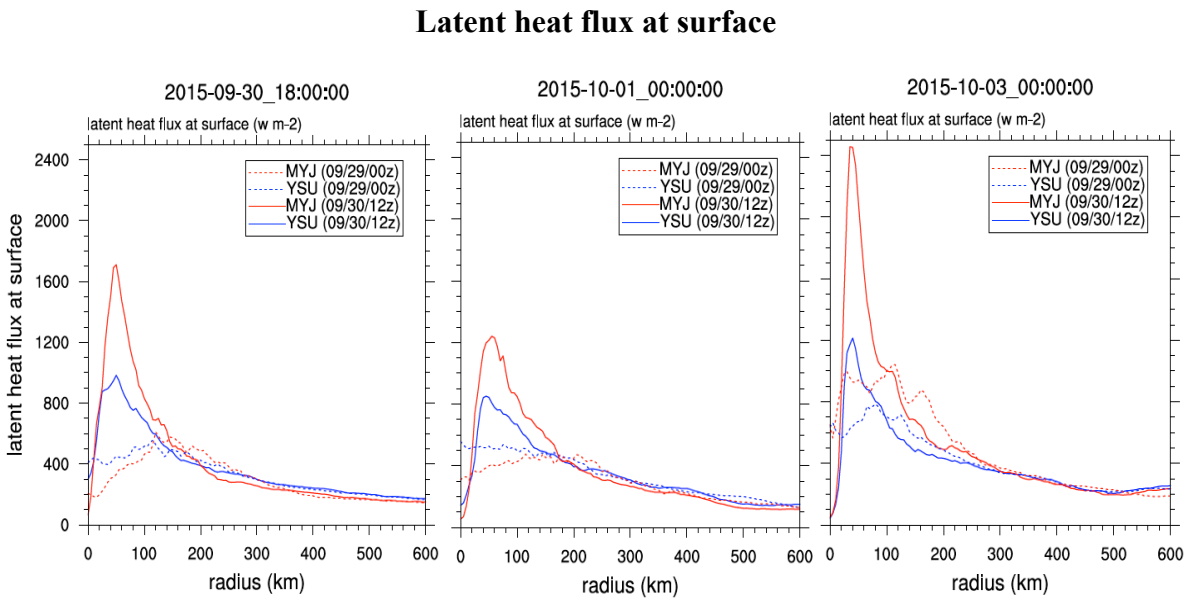

Figure 3.27 Comparison of latent heat flux at surface (units: w m^{-2}) between MYJ and YSU schemes that initialized at 0000 UTC 29 Sep 2015 (dashed line) and 0012 UTC 30 Sep 2015 (solid line) at 1800 UTC 30 Sep 2015, 0000 UTC 1 Oct 2015, and 0300 UTC 1 Oct 2015.

Rain water mixing ratio at different initial times

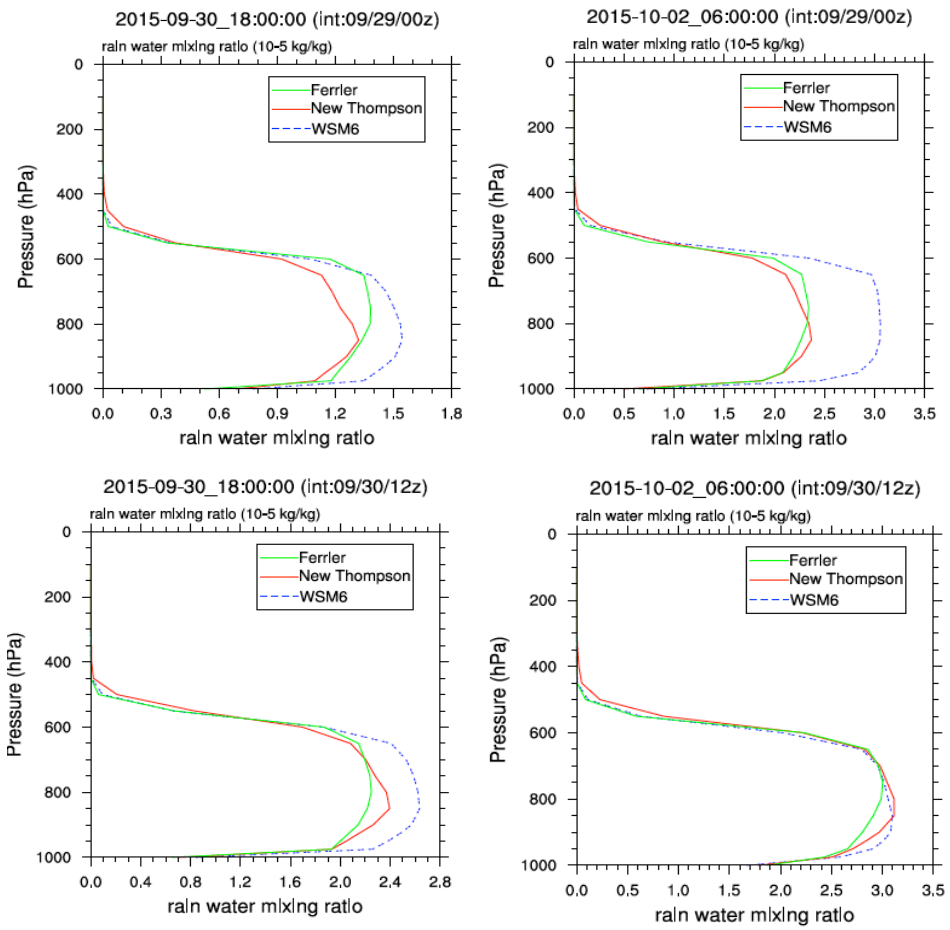

Figure 3.28 Rain water mixing ratio for three microphysics schemes that initialized at 0000 UTC 29 Sep 2015 (upper) and 0012 UTC 30 Sep 2015 (lower) at 1800 UTC 30 Sep and 0600 UTC 2 Oct 2015.

Snow mixing ratio at different initial times

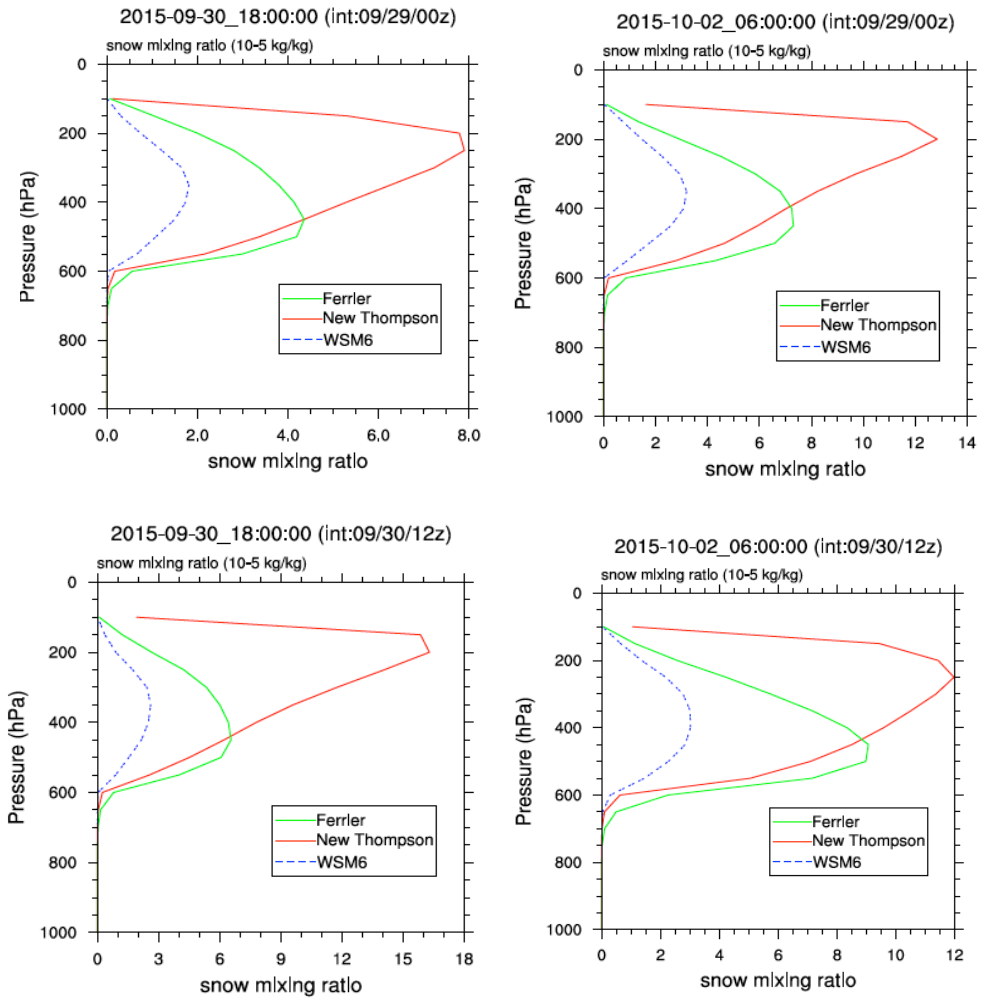

Figure 3.29 Comparison of snow mixing ratio for three microphysics schemes that initialized at 0000 UTC 29 Sep 2015 (upper) and 0012 UTC 30 Sep 2015 (lower) at 1800 UTC 30 Sep 2015 and 0600 UTC 2 Oct 2015.

CHAPTER 4

COMPARISON BETWEEN NAVGEM FORECASTS AND WRF HIGH-RESOLUTION SIMULATION

4.1 Introduction

In the previous chapter we found that different steering flows in the complex large-scale environment is the main factor that leads to different track forecasts. In this chapter, NAVGEM forecast is compared with the WRF high-resolution simulation that gives the best-track forecasts as described in the previous chapter. Specifically, with insights obtained from the previous chapter, we would like to evaluate the NAVGEM forecast focusing on its representation of the large-scale environment and flow patterns. Despite the relatively coarse resolution of the global model, averaged inner-core features that contributed to the intensity trend forecast are also compared with the WRF simulation.

4.2 Data description

The NAVGEM model is cycled four times a day at 00 UTC, 06 UTC, 12 UTC, and 18 UTC. Satellite radiance observations typically account for more than 65% of the total assimilated observations in NAVGEM. These observations are brought into the NAVGEM by NRL Atmospheric Variational Data Assimilation System (Hogan et al., 2014). The forecast fields at each cycle time are retrieved from the data archive for the periods of interest.

The wind fields of NAVGEM are going to be compared with satellite-derived atmospheric motion vectors (AMVs), which are derived using automated procedures that provide estimates of wind at multiple levels using ordered sequences of multispectral satellite images. The algorithm derives wind observations from the VIS, IR window, and WV absorption bands. The extraction of AMV from the WV band provides wind data in the regions devoid of cloud in the middle–upper troposphere (Velden et al., 1997). AMV data are typically distributed over the entire troposphere, but exhibit a concentration of vectors in the lower levels (at around 900–800 hPa) and a second maximum in the upper levels (at around 200–300 hPa).

4.3 Comparison of track and intensity

The NAVGEM forecast is compared with the best WRF simulation results initialized at 1200 UTC 30 September 2015. Specifically, it is compared with the WRF experiments that use the WSM6 microphysics scheme, the Kain-Fritsch cumulus scheme, the YSU planetary boundary layer scheme and GFS analysis data as initial and boundary conditions.

The track and intensity plots from 1200 UTC 30 September 2015 to 0000 UTC 4 October 2015 are shown in Figure 4.1. The track simulations are good for both the NAVGEM forecast and the WRF model simulation, with track errors within 80km in the first 60 h and 180 km from 60 to 84 h (Figure 4.2). Specifically, track errors range between 40 and 110 km for the NAVGEM forecast and between 40 and 160 km for the WRF simulation, while the WRF simulation is better than the NAVGEM forecast within the 72-h integration.

For intensity, the NAVGEM forecast successfully captures the intensification process but is much weaker than the best track or WRF intensity in MSLP and MSW. In general, it is 20–30 hPa weaker than the best track and 10–20 hPa weaker than the WRF simulation (Figure 4.3). Neither WRF nor NAVGEM shows good representation of the best-track intensity, although WRF model produces a better simulation of intensity than NAVGEM does.

4.4 Large-scale environment

The large-scale environment is compared between the NAVGEM forecast and WRF simulations at 1800 UTC 1 October 2015, before the hairpin clockwise recurve of Hurricane Joaquin.

For the geopotential fields (Figure 4.4), both models capture the major weather systems at this time: a strong high-pressure region from lower to middle levels to the north-east of Joaquin, a mid- to upper-level high pressure aloft over the north Atlantic Ocean to the south-west of Joaquin, the remnants of Tropical Storm Ida in the Atlantic and the mid- to upper-level trough over the eastern United States to the north-west of Joaquin (Figure 4.4). At 500 hPa, the two 5838-m contours are separated by a high-pressure region in the NAVGEM scheme. This is consistent with the selected WRF simulation and different from the other two WRF simulations with different cumulus schemes that predict the wrong steering. A major difference is found in the representation of Tropical Storm Ida; the central pressure is lower in the WRF simulation than in the NAVGEM forecast. This is partially attributed to the coarse resolution of the NAVGEM forecast.

Distributions of large-scale temperature fields are similar in lower, middle, and upper levels between the two models. Relatively high temperatures are found to the south of Hurricane Joaquin at 850 hPa and 700 hPa (Figure 4.5). A major difference occurs at the storm center of both Joaquin and Ida. The temperature in the NAVGEM forecast is colder than in the WRF simulation at all levels, especially in the region of Tropical Storm Ida.

Environmental relative humidity (RH) is also compared. The two models show a similar distribution of the RH field at the lower and middle levels (Figure 4.6). A great difference occurs in the upper level, where the RH in the NAVGEM forecast is much higher than that in the WRF simulation. However, this difference does not seem to alter the distribution of weather systems and TC track.

For wind fields, since the geopotential fields are quite similar, the wind fields are also similar between the NAVGEM forecast and the WRF simulation at the lower, middle and upper levels (Figure 4.7). A major difference occurs in the region of Tropical Storm Ida, where the cyclonic circulation is much weaker in the NAVGEM forecast than in the WRF simulation, especially at lower levels. This is expected from the coarse resolution of NAVGEM forecasts. For wind speed, the two models are similar except that the wind speed at the storm center is weaker in the NAVGEM forecast than in the WRF simulation.

Comparing the satellite-derived AMVs during the intensification period, the NAVGEM forecast and the AMV wind fields show good consistency. Note that the vectors in the AMV plots are from a time interval of +/-3h centered at 1800 UTC 1 October 2015, where purple windbarbs represent +/-1h data, blue windbarbs represent +/-2h data and light blue windbarbs represent +/-3h data. At low levels, the positions of the cyclonic circulation of Hurricane Joaquin and two anti-cyclonic circulations around the high-pressure system above the North Atlantic basin are the same (Figure 4.8). Data are

relatively sparse for midlevel AMVs. However, even with these sparse data, it seems that the circulation around the midlevel high to the southwest of Joaquin is weaker at 500 hPa in the NAVGEM forecast than at 600–300 hPa in the AMVs. The outflow-level wind fields are comparatively complex. But, the NAVGEM forecast and the AMVs are generally similar.

4.5 Core regions

TC intensity changes are closely correlated with how the model handles convection and the moisture and temperature distribution. None of the WRF simulations can well represent the rapid intensification periods of Hurricane Joaquin. For the first 60 h integration, the selected WRF simulation captures the intensity trend to some extent. As shown in the previous chapter, the intensification is connected with a stronger updraft and an increment of the upper-level temperature anomaly. Due to the coarse resolution of the NAVGEM model, the updraft cannot be clearly resolved. Only some averaged features in the core region are compared to the WRF simulation.

Soundings averaged within 3 degrees of the storm center are compared to investigate the ability of NAVGEM to represent the atmospheric state at the storm center. The temperature profile is quite similar between the two models while the humidity is much lower in the WRF simulation above 500 hPa (Figure 4.9). The convective available potential energy is much larger in the WRF simulation, which means the atmospheric instability is much higher in the WRF simulation compared to the NAVGEM forecast in the storm region.

The evolution of the warm-core structure is also investigated. During the intensification periods, both the NAVGEM forecast and the WRF simulation show

increments in the upper-level temperature anomaly (Figure 4.10). However, in addition to the strength of the temperature anomaly, double-warm cores exist in the NAVGEM forecast instead of one. Additionally, the increment of warm-core height is not significant in the NAVGEM forecast compared to that in the WRF simulation, indicating that the intensification of the convection is also not significant. The low temperature anomaly at 400 hPa may relate to the drier air at this level as shown in the soundings and the latent heat release is smaller in the NAVGEM forecast at this level.

4.6 Summary

The intensity of Joaquin from the NAVGEM forecast at the mature stage is much lower than the best track in both wind and pressure fields, as expected from the relatively coarse resolution of the NAVGEM model. The core region structures are different from the WRF simulation. For large scale environment, the distribution of temperature, moisture, and geopotential height fields are quite similar between the NEVGEM forecast and the WRF simulation, except that the mid- to upper-level regions are much moister in the NAVGEM forecast. The NAVGEM forecast also shows a good representation of wind fields, compared with satellite-derived atmospheric motion vectors (AMVs). Overall, the NAVGEM forecast can reasonably represent TC environmental conditions at its resolution.

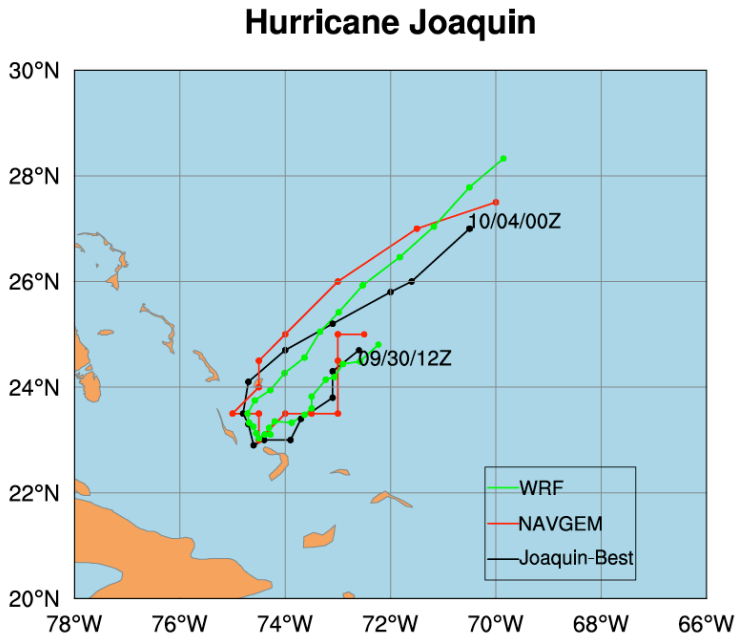

Figure 4.1 Comparison of tracks from WRF simulation and NAVGEM analysis during 1200 UTC 30 Sep 2015 to 0000 UTC 4 Oct 2015.

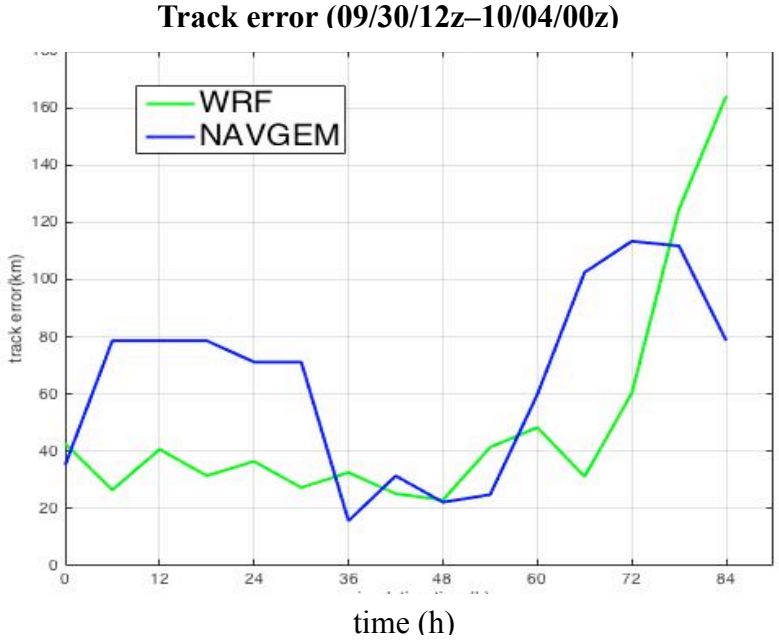

Figure 4.2 Variation of track errors with time (units: km) for WRF simulation and NAVGEM analysis during 1200 UTC 30 Sep 2015 to 0000 UTC 4 Oct 2015.

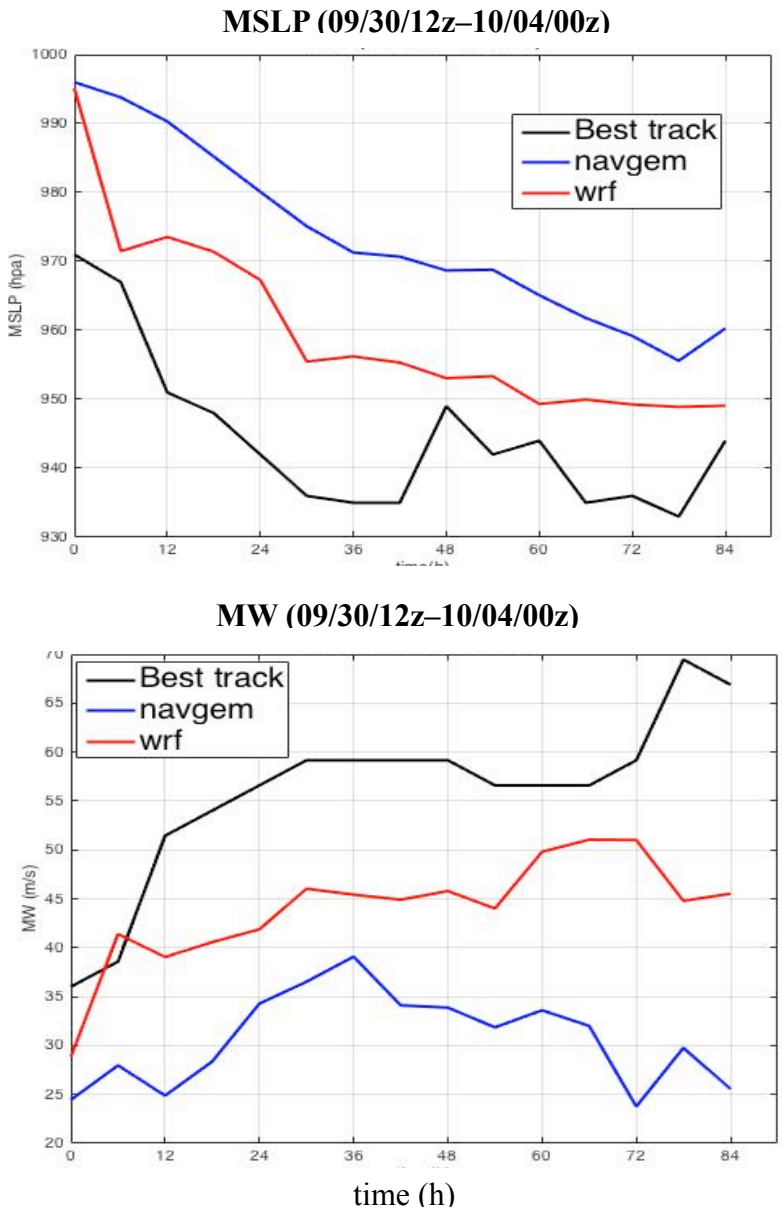

Figure 4.3 Minimum sea level pressure (upper, units: hPa) and maximum surface wind (lower, units:m s^{-1}) for NAVGEM analysis, WRF simulation and best track during 1200 UTC 30 Sep 2015 to 0000 UTC 4 Oct 2015.

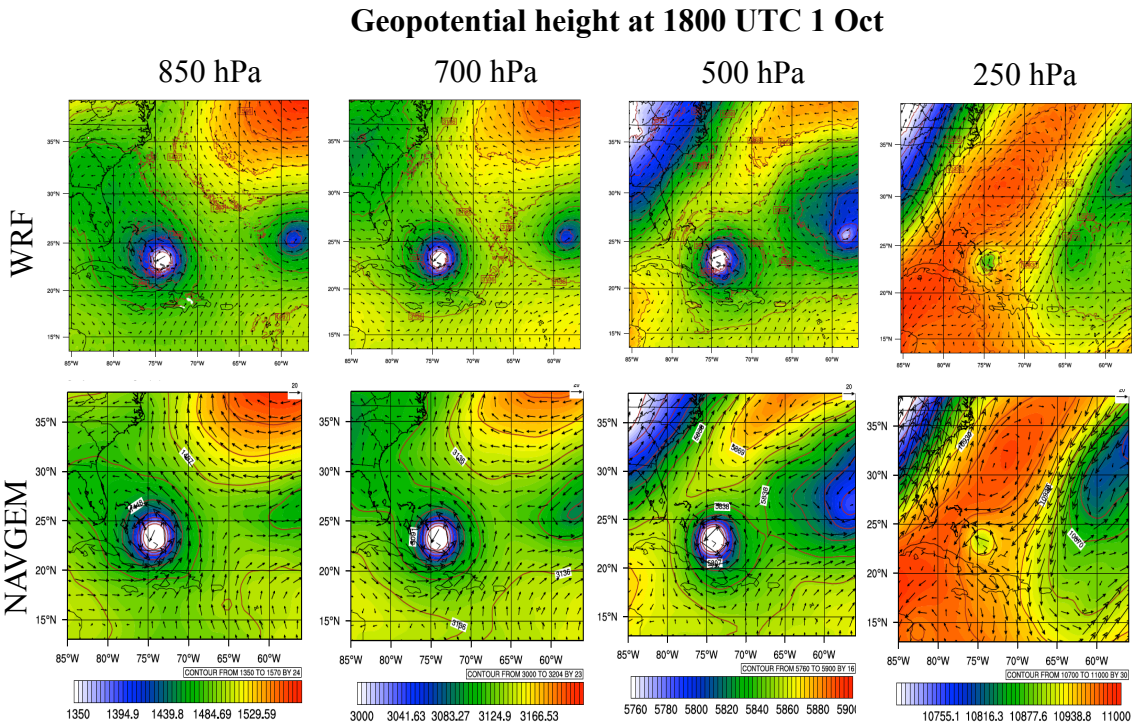

Figure 4.4 The geopotential height (units: m) for the WRF simulation (upper) and the NAVGEM analysis (lower) at 850 hPa, 700 hPa, 500 hPa, and 250 hPa at 1800 UTC 1 Oct 2015.

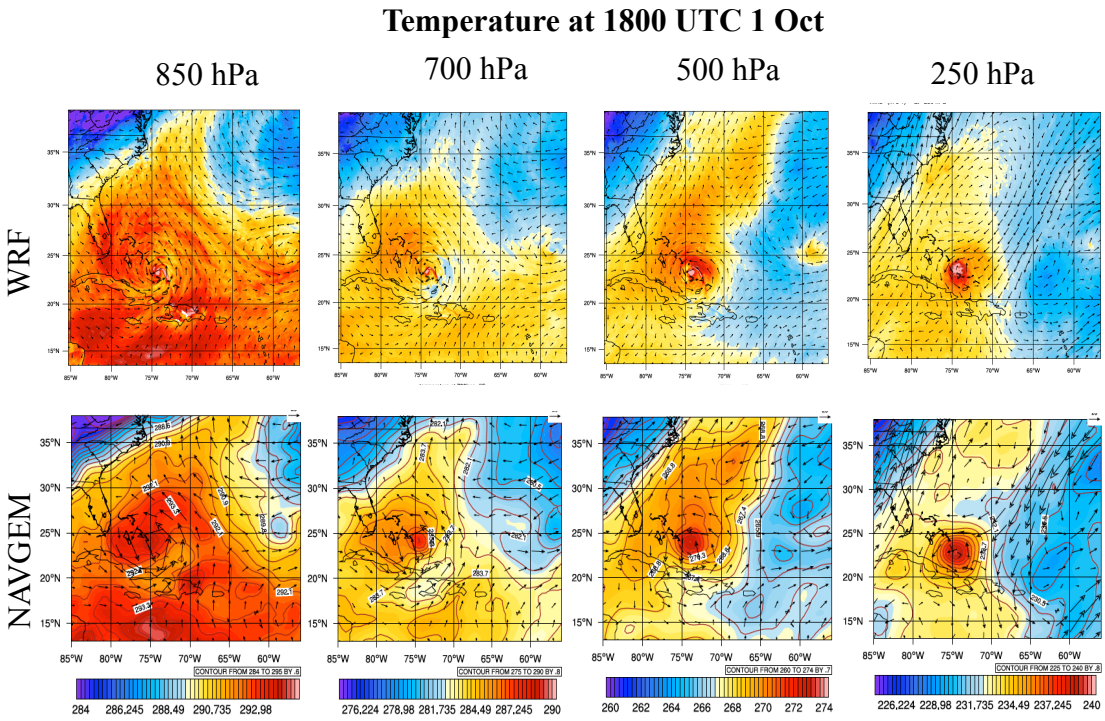

Figure 4.5 The temperature (units: K) for the WRF simulation (upper) and the NAVGEM analysis (lower) at 850 hPa, 700 hPa, 500 hPa, and 250 hPa at 1800 UTC 1 Oct 2015.

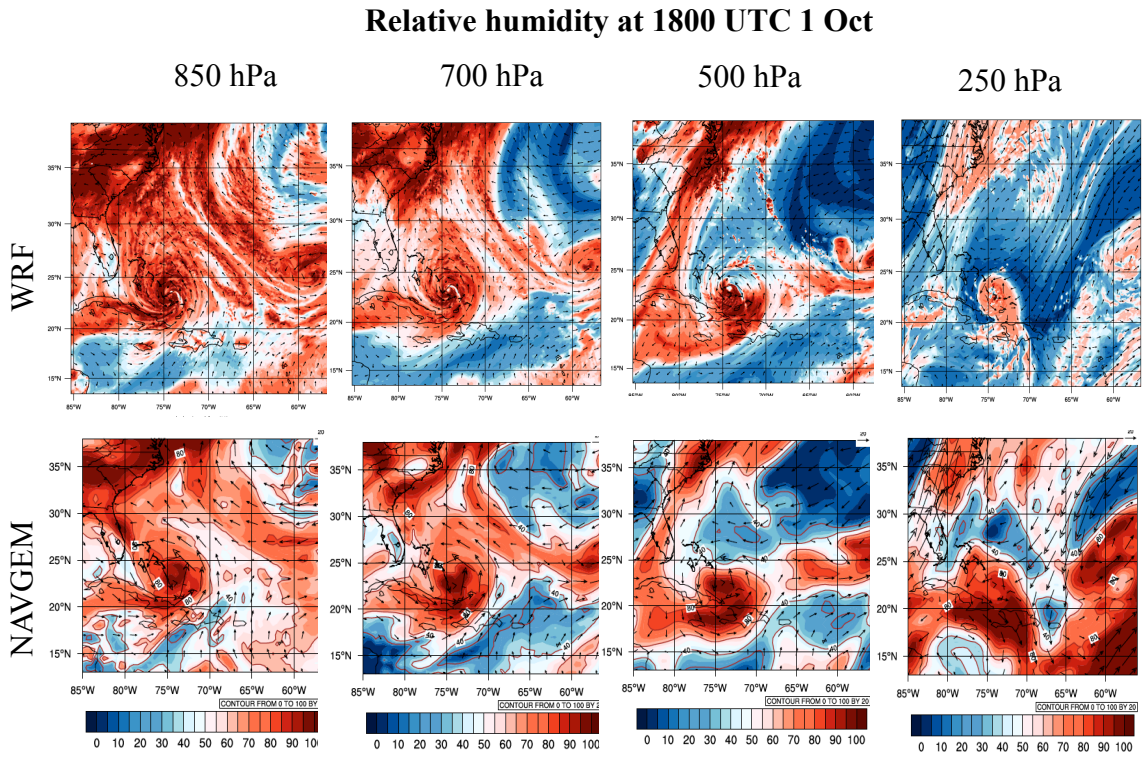

Figure 4.6 The relative humidity (units: %) for the WRF simulation (upper) and the NAVGEM analysis (lower) at 850 hPa, 700 hPa, 500 hPa, and 250 hPa at 1800 UTC 1 Oct 2015.

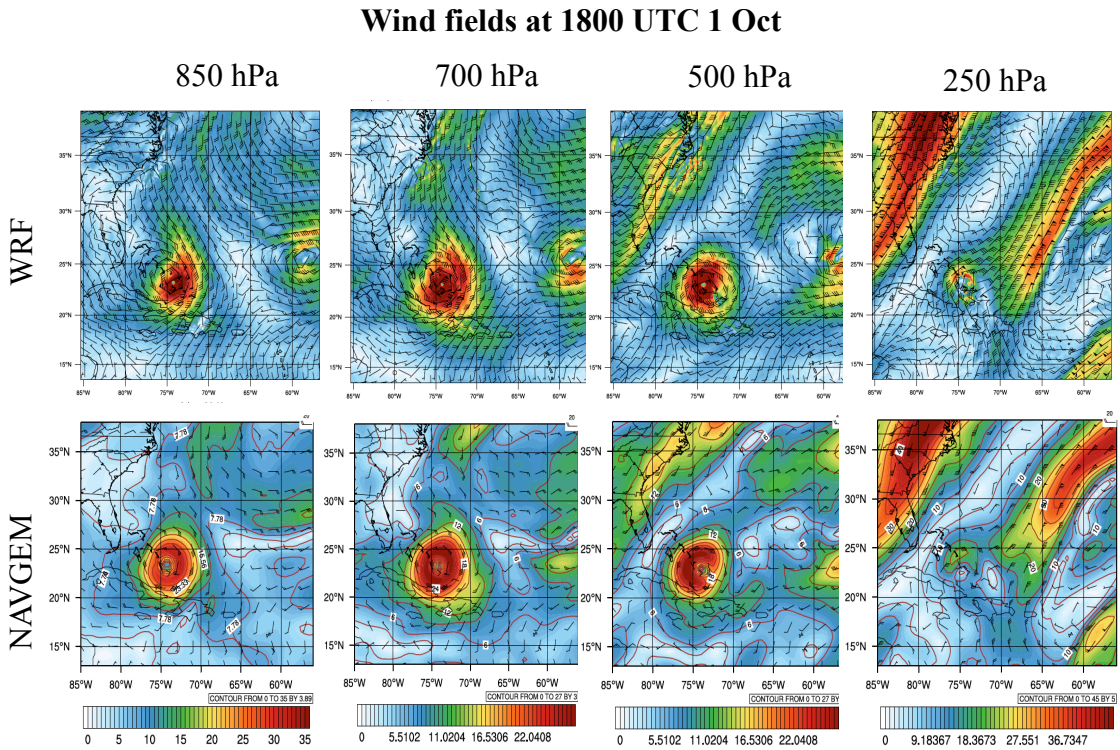

Figure 4.7 The wind fields (units: m s^{-1}) for the WRF simulation (upper) and the NAVGEM analysis (lower) at 850 hPa, 700 hPa, 500 hPa, and 250 hPa at 1800 UTC 1 Oct 2015.

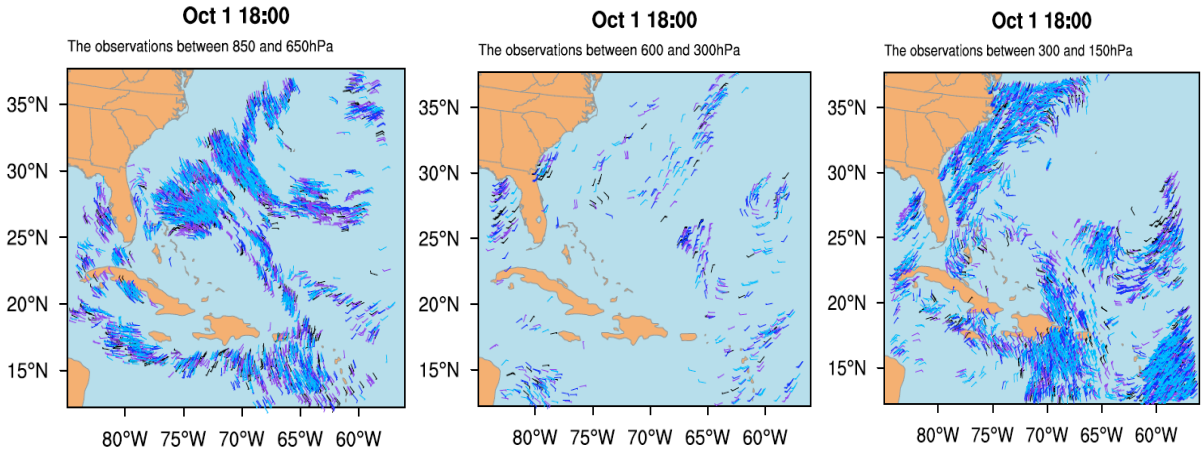

Figure 4.8 The AMVs at low levels (850–650 hPa), middle levels (600–300 hPa) and upper levels (300–150 hPa) at 1800 UTC 1 Oct 2015.

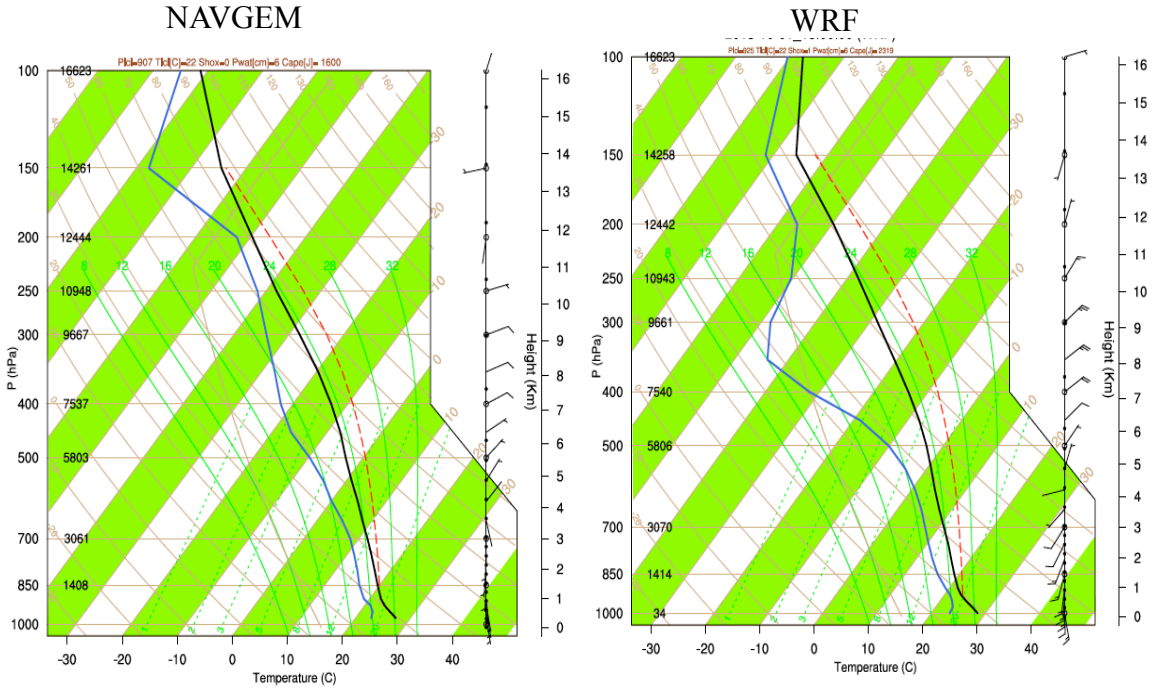

Figure 4.9 Soundings averaged over a radius of 3 degrees centered at the storm center for the NAVGEM analysis (left) and the WRF simulation (right) at 1800 UTC 1 Oct 2015.

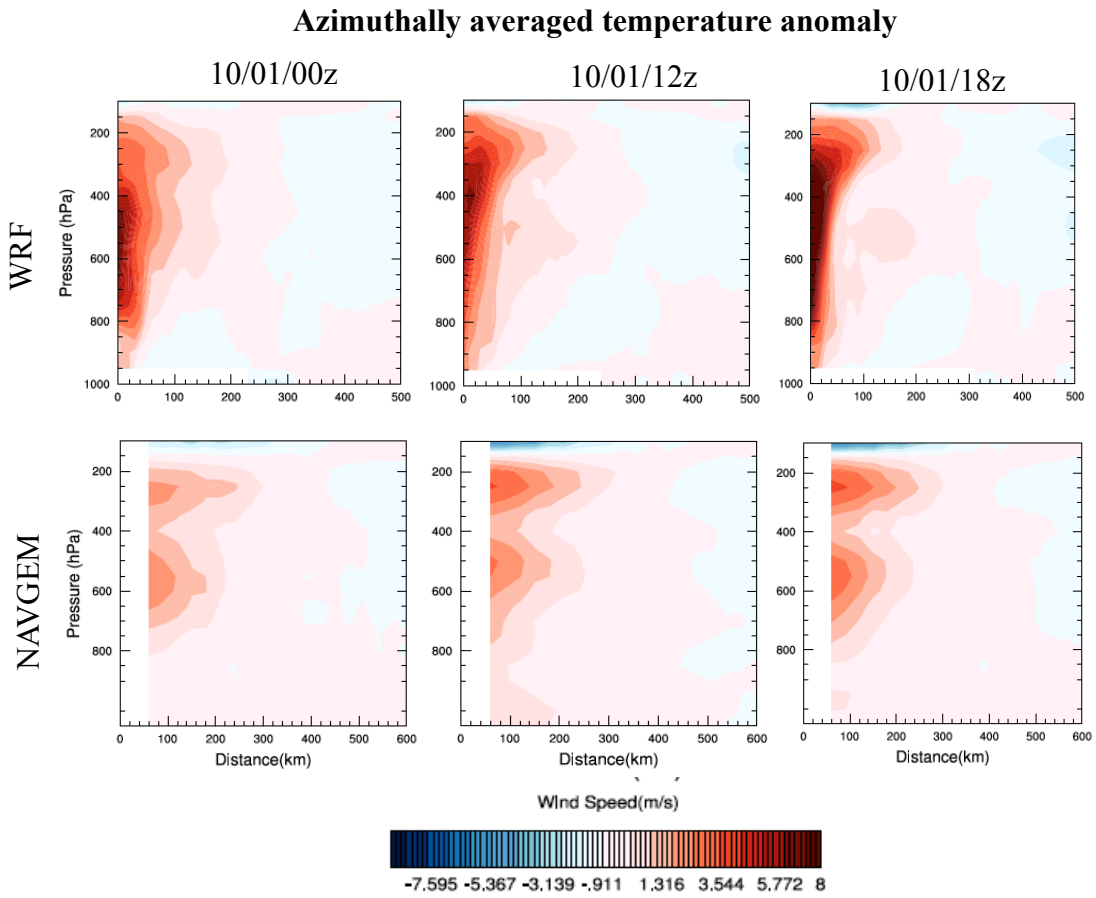

Figure 4.10 The temperature anomaly (units: K) for the WRF simulation (upper) and the NAVGEM analysis (lower) at 0000 UTC 1 Oct, 1200 UTC 1 Oct and 1800 UTC 1 Oct 2015.

CHAPTER 5

CONCLUDING REMARKS

In this study, a statistical evaluation of track and intensity forecasts has been performed for the Navy Global Environmental Model (NAVGEM) during June to November 2014 for the Atlantic, East Pacific, and West Pacific basins. Results show that the averaged track errors of NAVGEM range from about 100km at day 1 to 460 km at day 5. The NAVGEM model has good skill in forecasting the intensity trend, although the predicted intensifications lag the observed intensifications in many cases. The performance of the NAVGEM global dynamical model shows that no significant difference exists in track and intensity prediction among the Atlantic, East Pacific, and West Pacific basins.

Considering the challenge in forecasting the track of Hurricane Joaquin (2015), a series of numerical simulations has been conducted with the mesoscale WRF model. Sensitivity to different cumulus schemes shows that significant differences in the representation of temperature fields can lead to different large-scale environmental flows. By comparing the simulations with successful and unsuccessful track forecasts, it is shown that the environmental steering flow is an important factor that influences the evolution of Joaquin's track. Then, the best WRF simulation among all experiments was compared with the NAVGEM forecasts to obtain additional insight into the representation of the environmental steering in the NAVGEM model.

Although it is impossible for a global model to represent the finer-scale details of the inner-core region that determine the intensity of a TC due to the relatively coarse resolution, NAVGEM makes a fairly good track forecast with reasonable representation of hurricane environmental conditions at its resolution.

Future work should emphasize more case studies and more detailed investigation of the factors that influence hurricane intensity forecasting in both global and regional models.

REFERENCES

Adler, R. F., and E. B. Rodgers, 1977: Satellite-observed latent heat release in a tropical cyclone. *Mon. Wea. Rev.*, **105**, 956–963.

Burton, A., and Coauthors, 2010: Tropical cyclone structure and intensity change: Operational guidance. Seventh Int. Workshop on Tropical Cyclones, La Reunion, France, WMO/CAS/ WWW, 1.5.1–1.5.33.

Biswas, M. K., B. Ligia, and J. Dudhia, 2014: Sensitivity of hurricane forecasts to cumulus parameterizations in the HWRF model. *Geophysical Research Letters*, **41(24)**, 9113-9119.

Chan, J. C. L. and J. D. Kepert, Eds., 2010: Global Perspectives on Tropical Cyclones: From Science to Mitigation. World Scientific, 436 pp.

Chen, G., H. Yu, Q. Cao and Z. Zeng, 2013: The performance of global models in TC track forecasting over the western North Pacific from 2010 to 2012. *Tropical Cyclone Research and Review*, **2(3)**, 149-158.

DeMaria, M., C. R. Sampson, J. A. Knaff, K. D. Musgrave, 2014: Is Tropical Cyclone Intensity Guidance Improving?. *Bull. Amer. Meteor. Soc.*, **95**, 387–398. doi: http://dx.doi.org/10.1175/BAMS-D-12-00240.1

Duan, Y., L. Chen, Y. Xu, and C. Qian, 2012: The status and suggestions of the improvement in the typhoon observation, forecasting and warning systems in China (in Chinese). *Eng. Sci.*, **14 (9)**, 4–9.

Fierro, A. O., R. F. Rogers, F. D. Marks, and D. S. Nolan, 2009: The impact of horizontal grid spacing on the microphysical and kinematic structures of strong tropical cyclones simulated with the WRF-ARW model. *Mon. Wea. Rev.*, **137**, 3717–3743.

Hill, K. A., and G. M. Lackmann, 2009: Analysis of idealized tropical cyclone simulations using the Weather Research and Forecasting Model: Sensitivity to turbulence parameterization and grid spacing. *Mon. Wea. Rev.*, **137**, 745–765.

Hong, S., and J. J. Lim, 2006: The WRF single-moment 6-class microphysics scheme (WSM6). *J. Kor. Meteor. Soc.*, **42**, 129– 151.

Hong, S.-Y., and J. Dudhia, 2003: Testing of a new nonlocal boundary layer vertical diffusion scheme in numerical weather prediction applications. Preprints, 20th Conf. on Weather Analysis and Forecasting/16th Conf. on Numerical Weather Prediction, Seattle, WA, *Amer. Meteor. Soc.*, 17.3. [Available online at http://ams.confex.com/ams/pdfpapers/72744.pdf.]

Pan, H.-L., and W.-S. Wu, 1995: Implementing a mass flux convection parameterization package for the NMC mediumrange forecast model. NMC Office Note 409, 43 pp. [Available from NCEP, 5200 Auth Road, Washington, DC 20233.]

Hogan, T.F., M. Liu, J.A. Ridout, M.S. Peng, T.R. Whitcomb, B.C. Ruston, C.A. Reynolds, S.D. Eckermann, J.R. Moskaitis, N.L. Baker, J.P. McCormack, K.C. Viner, J.G. McLay, M.K. Flatau, L. Xu, C. Chen, and S.W. Chang, 2014: The Navy Global Environmental Model. *Oceanography* **27(3)**, 116-125.

Janjić, Z. I., 1994: The step-mountain Eta coordinate model: Further developments of the convection, viscous sublayer, and turbulence closure schemes. *Mon. Wea. Rev.*, **122**, 927–945.

Kain, J., 2004: The Kain–Fritsch convective parameterization: An update. *J. Appl. Meteor.*, **43**, 170–181.

Kain, J. S., and J. M. Fritsch, 1993: Convective parameterization for mesoscale models: The Kain–Fritsch scheme. The Representation of Cumulus Convection in Numerical Models, *Meteor. Monogr.*, No. **24**, Amer. Meteor. Soc., 165–170.

Kanase, R. D., and P. S. Salvekar, 2015: Effect of physical parameterization schemes on track and intensity of cyclone LAILA using WRF model. *Asia-Pac. J. Atmos. Sci.,* **51(3)**, 205-227.

Kuo, H.-L., 1974: Further studies of the parameterization of the in- fluence of cumulus convection on the large scale flow. *J. Atmos. Sci.*, **31**, 1232–1240.

Lim, K.-S. S., and S.-Y. Hong, 2010: Development of an effective double-moment cloud microphysics scheme with prognostic cloud condensation nuclei (CCN) for weather and climate models. *Mon. Wea. Rev.*, **138**, 1587–1612.

Marchok, T., 2014: Operational Hurricane Track and Intensity Forecasting. Accessed 10 June 2016. [Available online at http://www.gfdl.noaa.gov/operational-hurricane-forecasting]

Mellor, G. L., and T. Yamada, 1982: Development of a turbulence closure model for geophysical fluid problem. Rev. Geophys. *Space Phys.*, **20**, 851–875.

Mandal, M., U. C. Mohanty, and S. Raman, 2004: A study of the impact of parameterization of physical processes on prediction of tropical cyclone over the Bay of Bengal with NCAR/ PSU mesoscale model (MM5). *Nat. Hazards*, **31**, 391–414.

Morrison, H.,and J. Milbrandt, 2011: Comparison of two-moment bulk microphysics schemes in idealized supercell thunderstorm simulations. *Mon. Wea. Rev.,* **139**, 1103–1130.

Nicholas, C. W., 2003: Sensitivity of Tropical Cyclone Track, Intensity, and Orographic Precipitation to Cumulus and Microphysical Parameterizations. *10th Conference on Mesoscale Processes*.

Nolan, D. S., J. A. Zhang, and D. P. Stern, 2009a: Evaluation of planetary boundary layer parameterizations in tropical cyclones by comparison of in situ data and high-resolution simulations of Hurricane Isabel (2003). Part I: Initialization, maximum winds, and outer-core boundary layer structure. *Mon. Wea. Rev.*, **137**, 3651–3674.

Pauley, R., J. Nachamkin, W. Clune, T. Duffy, and L. Lyjak, 2013: Operational Test Report for Navy Global Environmental Model (NAVGEM) System.

Pattanayak, S., U. C. Mohanty, and K. K. Osuri, 2012: Impact of parameterization of physical processes on simulation of track and intensity of Tropical Cyclone Nargis (2008) with WRFNMM Model. *Sci. World J.*, 2012, 671437, doi:10.1100/ 2012/671437

Pasch, R. and J.S. Clark, 2009: Technical Summary of the National Hurricane Center Track and Intensity Models. Accessed 10 June 2016. [Available online at http://www.nhc.noaa.gov/pdf/model_summary_20090724.pdf]

Anthes, R. A., 1977: A cumulus parameterization scheme utilizing a one-dimensional cloud model. *Mon. Wea. Rev*., **105**, 270–286.

Reynolds, C., 2014: Recent Developments in Navy Numerical Weather Prediction. Accessed 10 June 2016. [Available online at http://polar.ncep.noaa.gov/conferences/WGNE-30/pdfs/day2/09-NRL_report.pdf]

Sampson, C. R., R. A. Jeffries, C. J. Neumann, and J.-H. Chu, 1995: Tropical cyclone forecasters reference guide. NRL Rep. NRL/ PU/7541–95–0012, U.S. Naval Research Laboratory, 48 pp.

Skamarock, W. C., J. B. Klemp, J. Dudhia, D. O. Gill, D. M. Barker, W. Wang, and J. G. Powers, 2007: A description of the Advanced Research WRF Version 2. NCAR Tech. Note NCAR/TN-4681STR, 88 pp.

Tao, W.-K., J. J. Shi, S. S. Chen, S. Lang, P.-L. Lin, S.-Y. Hong, C. PetersLidard, and A. Hou, 2011: The impact of microphysical schemes on hurricane intensity and track. *Asia-Pac. J. Atmos. Sci.*, **47**, 1–16.

Thompson, G., R. M. Rasmussen, and K. Manning, 2004: Explicit forecasts of winter precipitation using an improved bulk microphysics scheme. Part I: Description and sensitivity analysis. *Mon. Wea. Rev.*, **132**, 519–542.

Velden, C. S., C. M. Hayden, S. J. Nieman, W. P. Mensel, S. Wanzong, and J. S. Goerss, 1997: Upper-tropospheric winds derived from geostationary satellite water vapor observations. *Bull. Amer. Meteor. Soc*., **78**, 173–195

Wang, Y., and C. C. Wu, 2003: Current understanding of tropical cyclone structure and intensity changes—A review. *Meteor. Atmos. Phys.*, **87**, 257–278, doi:10.1007/s00703-003-0055-6.

Yanai, M., S. Esbensen, and J. Chu, 1973: Determination of bulk properties of tropical cloud clusters from large-scale heat and moisture budgets. *J. Atmos. Sci*., **30**, 611–627.

Yu, H., P. Chen, Q. Li, and B. Tang, 2013: Current capability of operational numerical models in predicting tropical cyclone intensity in the western North Pacific. Wea. Forecasting, **28**, 353–367, doi:10.1175/WAF-D-11-00100.1.

Zhao, Q. Y., and F. H. Carr, 1997: A prognostic cloud scheme for operational NWP models. *Mon. Wea. Rev.,* **125**, 1931-1953

Zarzycki, C. M., and C. Jablonowski, 2015: Experimental tropical cyclone forecasts using a variable-resolution global model. *Mon. Wea. Rev.*, **143**, 4012–4037, doi:10.1175/MWR-D-15-0159.1.